Lattices of Generalized Skyrmions

SILVA-LOBO, JORGE,IVAN

Lattices of Generalized Skyrmions

Jorge Iván Silva Lobo

Abstract

Generalized Skyrme systems are those which include both the Skyrme and the Skyrme-Faddeev models through an interpolating parameter $\alpha \in [0, 1]$; the former corresponds to $\alpha = 0$ and the latter to $\alpha = 1$. Our numerical and analytical investigations centre around the $\alpha = 0$ Skyrme crystal, its deformations, and its behaviour and symmetries as a function of α, called the generalized Skyrme crystal. We show that a double square lattice emerges when the Skyrme crystal is deformed in a certain limit; we compare its energy with the one corresponding to a double hexagonal lattice and show that it has a lower energy-per-charge than its hexagonal counterpart. On the other hand, vortex-like structures with two 1-vortices (vortices of order 1) and two 1-antivortices, denoted V+AV+V+AV, appear when the Skyrme crystal is deformed in a different limit, as well as when the generalized Skyrme crystal is taken close to the Skyrme-Faddeev limit. This leads us to the study of generalized V+AV and V+AV+V+AV configurations, as a function of α. We show that when these configurations are stacked in the axial direction, they exhibit some winding and linking properties as they are taken close to the Skyrme-Faddeev limit, where the V+AV+V+AV configurations appear to be more stable than their V+AV counterparts. Finally, the study of such configurations led to the discovery of two crystalline solutions whose properties are investigated in some detail: a 2-vortex/2-antivortex pair, denoted 2V+2AV, and a "multi-sheet" solution, both of which have a lower energy-per-charge than the V+AV+V+AV solution, in the Skyrme-Faddeev limit.

Lattices of Generalized Skyrmions

Jorge Iván Silva Lobo

A thesis submitted in partial fulfilment
of the requirements for the degree of
Doctor of Philosophy

Department of Mathematical Sciences
Durham University

October 7, 2011

Contents

List of Tables

List of Figures

Declaration

I confirm that no part of the material offered has previously been submitted by myself for a degree in this or any other University. Where material has been generated through joint work, the work of others has been indicated.

Jorge Iván Silva Lobo
Durham, October 7, 2011

Statement of Originality

I have co-authored two papers [1, 2] with my PhD supervisor, Prof. Richard Ward. These represent joint work related to the material presented in sec. 5.3 and Chapter 4, respectively. I have taken great care in these chapters in presenting my own work and, where possible, citing the aforementioned papers whenever I wish to refer to work carried out by Prof. Ward. For example, in Chapter 4, I focus on my own work dealing with the square and hexagonal 2-wall results as well as the process undertaken in getting these results, referring the reader to [2] when discussing the square N-wall results (where $N > 2$), which was work undertaken by Prof. Ward. Another example can be seen in Fig. 5.18 from sec. 5.3, which shows a plot similar to one presented in [1]. In the latter, one can see that there are additional data points, which represent work carried out by Prof. Ward, and which do not appear in the former, which shows my own data points.

Except chapters 1, 2, and sec. 4.1, which contain background information, with the relevant books and papers cited throughout, the rest of the work presented is my own (except where indicated). Chapter 3 is taken from my own paper [3] (with a few minor changes to the figures) and Chapter 6 includes material which has not been published before. Finally, it is worth mentioning that the material presented in sec. 2.4.2 is based on some (incomplete) notes given to me by Prof. Ward, which deal with calculations leading to some of the results presented in his paper [4]; to the best of our knowledge, this material has not been published before and was deemed interesting enough to be included here.

Jorge Iván Silva Lobo
Durham, October 7, 2011

Statement of Copyright

Acknowledgements

I remember early on in my PhD, while in the process of choosing a PhD supervisor, I had talked with some of Prof. Richard Ward's PhD students as well as some members of academic staff at the Department of Mathematical Sciences, regarding Richard's supervisory style. They all seemed to agree that he is an excellent PhD supervisor. I can now confirm that this is true. He has always been extremely helpful to me and have him to thank for many of the achievements that have taken place throughout my PhD. Not only has he been a great supervisor, but he has also been a great collaborator, having worked together on two papers [1, 2]. He seems to have an instinct for quickly finding the paths that will lead to interesting results and avoiding the not-so-interesting ones. This would not be surprising to those who know about the many important contributions that he has made to the field.

I would like to thank my family for their enduring love and support (all the way from Mexico) and especially my father, Carlos Humberto Silva Platt, who has always pressed me to strive for my dreams, saying that anything is possible. This, together with his very generous and unconditional support, has allowed me to get to where I am in my academic and personal life.

Finally, I would also like to thank my girlfriend, Sylvi Händel, for giving me a lot of constructive German criticism in the process of writing my thesis and for making my PhD one of the most exciting periods of my life. She has a refreshing drive and joy of life, which has provided the impetus for the many experiences we have shared together throughout the course of our PhD's, such as the exploration of new places, cultures, and food – these would not have been nearly as enjoyable without her.

I don't know anything, but I do know that everything is interesting if you go into it deeply enough.

—*Richard P. Feynman*[1]

[1] In a May 1979 Omni magazine interview.

Part I

Introduction

Chapter 1

Background

1.1 Historical background

The study of solitons is generally regarded to have begun in 1834, with an observation made by a Scottish naval engineer named John Scott Russell, who recounts in the 14th Meeting of the British Association for the Advancement of Science [5]:

> *I was observing the motion of a boat which was rapidly drawn along a narrow channel by a pair of horses, when the boat suddenly stopped–not so the mass of water in the channel which it had put in motion; it accumulated round the prow of the vessel in a state of violent agitation, then suddenly leaving it behind, rolled forward with great velocity, assuming the form of a large solitary elevation, a rounded, smooth and well-defined heap of water, which continued its course along the channel apparently without change of form or diminution of speed. I followed it on horseback, and overtook it still rolling on at a rate of some eight or nine miles an hour, preserving its original figure some thirty feet long and a foot to a foot and a half in height. Its height gradu-*

> *ally diminished, and after a chase of one or two miles I lost it in the windings of the channel. Such, in the month of August 1834, was my first chance interview with that singular and beautiful phaenomenon which I have called the Wave of Translation, a name which it now very generally bears; which I have since found to be an important element in almost every case of fluid resistance, and ascertained to be the type of that great moving elevation of the sea, which, with the regularity of a planet, ascends our rivers and rolls along our shores.*

The key words here being "large *solitary* elevation" and "preserving its original figure". The number of subjects under which solitons have been studied has greatly increased over the years from the original Fluid Dynamics, which Russell studied, to subjects as varied as Biology (apparently occurring in proteins [6]), Fiber Optics, Quantum Field Theory, Atomic and Molecular Physics (occurring in Bose-Einstein Condensates), Condensed-Matter Theory, and Classical Field Theory, which is the field that concerns us here. However, the properties of the "Wave of Translation" that Russell originally noticed: being localized, having permanent form, and the fact that two or more of these are unchanged after an interaction (an observation he made later), are still the main features of solitons studied across all fields.

Within Field Theory lies the subject of Topological Solitons. The most prominent examples of solitons studied in this field, in increasing number of dimensions, are: kinks (1D), lumps and vortices (2D), monopoles, skyrmions, and hopfions (3D), and instantons (4D), which also appear in other dimensions. There are two ingredients which essentially give rise to their stability: a set of boundary conditions for the fields, producing a non-trivial homotopy group, preserved by the relevant differential equations, whose solutions fall under homotopy classes generally indexed by an integer, called the topological charge. The other ingredient is an energy whose terms, under spatial

rescalings, scale in opposite ways. This phenomenon, which has a balancing effect on the size of the soliton, can be satisfied provided the theory has terms with the appropriate order in derivatives included. Note that this cancelling effect between the terms is similar to the cancellation of nonlinear and dispersive effects which gives rise to Russell's "Wave of Translation".

Here, we will be dealing with a skyrmion-hopfion "hybrid" – the solution of a model that interpolates between the Skyrme and Skyrme-Faddeev Models. In particular, our goal is to study lattices of such solitons.

1.2 Thesis summary

In Chapter 2, we give a general overview of the topics that form the basis for the numerical and analytical investigations which have been carried out. These are: the Skyrme and Skyrme-Faddeev models, the model of generalized Skyrme systems, which interpolates between the first two, and the Skyrme crystal.

In Part II, we shall focus on the Skyrme model limit of the generalized Skyrme systems. In Chapter 3, we deal with deformations of the Skyrme crystal, where the periods in all three directions are changed from their optimal, minimal-energy, values. We investigate the structures that emerge in different limits by looking at the energy-density isosurfaces, after deforming the periods of the Skyrme crystal and, subsequently, numerically minimizing the energy using a conjugate-gradient method. We see that, in one limit, a pair of square sheets are formed and, in a different limit, a series of four parallel, vortex-like, structures emerge. In Chapter 4, we investigate several properties of the square sheets and compare them with hexagonal sheets (similar to those investigated in [7]). More specifically, we determine the energy of the square and hexagonal 2-wall configurations and we investigate their stability as well as the stability of the hexagonal 4-wall, noticing along the way that

the latter tends to be more unstable than the former pair of configurations.

The parameter $\alpha \in [0, 1]$, from the model of generalized Skyrme systems, interpolates between the Skyrme and Skyrme-Faddeev models, reproducing the former at $\alpha = 0$ and the latter at $\alpha = 1$; in Part III, we take $\alpha \in [0, 1]$. In sec. 5.1, we generalize Manton's geometrical explanation of the Skyrme model, which is introduced in sec. 2.2, by considering the metric of a squashed 3-sphere rather than a 3-sphere. In sec. 5.2, we investigate the symmetries of the generalized Skyrme crystal energy density by analyzing its differences when certain isospin and chiral transformations are applied to the fields; we also study the isometries of the system. Finally, in sec. 5.3, we look at the behaviour of the Skyrme crystal as a function of α by analyzing its energy density isosurfaces. We notice that 4 parallel vortex-like structures appear as $\alpha \to 1$ (akin to one of the limits of the deformed Skyrme crystal at $\alpha = 0$), denoted V+AV+V+AV. We also notice that there exist other configurations (local energy minima) with lower energy-per-charge, such as a vortex-antivortex pair of degree 2 (2V+2AV) as well as a "multi-sheeted" structure, which turns out to have the lowest energy-per-charge of those we investigated. Furthermore, we look at an ansatz, whose fields are very similar to the multi-sheeted structure, and compare its energies and optimal periods with those of the multi-sheet solution.

In Chapter 6, we investigate the stability and energy density isosurfaces of vortex configurations when they are stacked multiple times in the $z-$direction, as a function of α. In sec. 6.1, besides looking at these features for the V+AV case, we provide a description of the inter-vortex force as a function of α (a generalization of the discussion of the inter-vortex force in the Skyrme Model, presented in [8]), and in sec. 6.2 we take a look at the V+AV+V+AV case. We notice that twisted and braided vortex structures appear for both cases at certain α values, although these do not exactly overlap. Finally, in Part IV, we present our concluding remarks.

Chapter 2

The Skyrme and Skyrme-Faddeev models, an interpolating model, and Skyrme crystals

2.1 The Skyrme model

The Skyrme model was originally proposed by Tony Skyrme in 1961 [9]. It is a theory of nuclear matter in which the fundamental building blocks are pion fields. It is a nonlinear, classical field theory in (3+1)-dimensions and its Lagrangian L and associated static energy E are given by [10]:

$$L = \int \left\{ \frac{F_\pi^2}{16} \mathrm{Tr}(\partial_\mu U \partial^\mu U^\dagger) + \frac{1}{32e^2} \mathrm{Tr}([\partial_\mu U U^\dagger, \partial_\nu U U^\dagger][\partial^\mu U U^\dagger, \partial^\nu U U^\dagger]) \right\} d^3x \,, \tag{2.1}$$

$$E = \frac{1}{12\pi^2} \int \left(-\frac{1}{2} \mathrm{Tr}(M_i M_i) - \frac{1}{16} \mathrm{Tr}([M_i, M_j][M_i, M_j]) \right) d^3x \,, \tag{2.2}$$

where F_π and e are parameters which have been scaled away in eq. (2.2) by rewriting the Lagrangian in terms of the following energy and length units: $\frac{F_\pi}{4e}$ and $\frac{2}{eF_\pi}$, the field U is an SU(2)-valued scalar field, "Tr" refers to the trace of

the object inside the brackets, $M_i = U^{-1}\partial U/\partial x^i$, $x^i = (x, y, z)$ are the spatial coordinates, and we make use of the notation $\partial_\mu U \partial^\mu U = (\partial_0 U)^2 - \partial_i U \partial_i U$, where repeated latin indices are summed over $i = \{1, 2, 3\}$. In eq. 2.2 we have also included a "normalization" factor, which simplifies the expression for an inequality, which we shall mention shortly.

The second term in eqs. (2.1, 2.2) is called the Skyrme term. A term of degree four or higher in the derivatives of the field must be included in order to evade Derrick's Theorem [11], which is a *non-existence* theorem for static solutions of the field equation under spatial rescalings $\mathbf{x} \mapsto \mu\mathbf{x}$. Under a spatial rescaling of this sort, the energy becomes

$$e(\mu) = \mu^{-1} E_2 + \mu E_4 \,, \tag{2.3}$$

where E_2 and E_4 are the terms in eq. (2.2) involving two and four derivatives, respectively. One can see that (2.3) has a minimal value for non-zero μ, as each term scales in opposite ways. Derrick's Theorem states that if one has a static soliton, then it must be a stationary point of (2.3).

The solutions to the Euler-Lagrange equation that can be derived from the Lagrangian (2.1) are known as skyrmions. In fact, the Skyrme Model can be regarded as a low-energy approximation to QCD, which becomes more accurate in the large N_c-limit, where N_c is the number of quark colours [12, 13].

The pions in the Skyrme Model can be encapsulated in the field $U(x^i)$ as follows:

$$U = \Phi_4 \cdot \mathbb{1} + i\Phi_i \sigma_i \,, \tag{2.4}$$

where Φ_i is the triplet of pion fields, σ_i is the triplet of Pauli matrices, and Φ_4 is an additional scalar field determined through the constraint: $\frac{1}{2}\mathrm{Tr}(U^\dagger U) = \Phi_\beta \Phi_\beta = 1$. For a skyrmion centred at the origin, we impose the following boundary conditions: $U(x^i) \to -\mathbb{1}$ as $|x^i| \to 0$ (i.e. $\Phi_i(x^i) \to 0$ and $\Phi_4(x^i) \to$

-1, as $|x^i| \to 0$) and $U(x^i) \to \mathbb{1}$ as $|x^i| \to \infty$ (i.e. $\Phi_i(x^i) \to 0$ and $\Phi_4(x^i) \to 1$, as $|x^i| \to \infty$).

The scalar field U is a map from $\mathbb{R}^3$, compactified at infinity[1], to S^3, the group manifold of SU(2). Skyrme identified the degree of this map, a topological invariant, with the baryon number. One can use homotopy groups to see where this number comes from, as follows: The map is given by $U : S^3 \to S^3$, where the domain is $\mathbb{R}^3 \cup \{\infty\}$. Therefore, the homotopy group is given by $\pi_3(S^3)$, which is an integer $\mathbb{Z}$. This means that maps from three-spheres to three-spheres fall into homotopy classes indexed by an integer, which is given by [10]:

$$Q = \int \mathcal{Q}\, dx\, dy\, dz\,, \tag{2.5}$$

where

$$\mathcal{Q} = -\frac{1}{24\pi^2}\varepsilon_{ijk}\mathrm{Tr}(M_i M_j M_k) \tag{2.6}$$

is the topological charge density. It is worth mentioning at this point that the energy from eq. (2.2) satisfies the Faddeev-Bogomolny lower bound [14] $E \geq |Q|$.

There has been a great deal of time and effort spent in the study of the structure and symmetries of low- and high-charge skyrmions (see e.g. [15–22]). To sum up, the charge density isosurfaces of Skyrmions (minimal-energy solutions) of charge $Q = 1, 2, 3, 4$ have Platonic symmetries: spherical, toroidal, tetrahedral, and cubic symmetries, respectively. Skyrmions of higher charge have more complicated structures, with symmetries generally falling within the dihedral group (D_n), the extended dihedral groups (D_{nh} and D_{nd}), or the highly symmetric icosahedral group (I_h). It has been noted [19] that the charge density structure of Skyrmions follows a Geometric Energy Minimization (GEM) rule, with the number of faces F, vertices V, and edges E given by: $F = 2(Q-1)$, $V = 4(Q-2)$, and $E = 6(Q-2)$. For $Q \geq 7$, these conditions can be satisfied with trivalent polyhedrons formed from 12

[1]The reason one must compactify at infinity is to keep energies finite as $|\mathbf{x}| \to \infty$.

pentagons and 2(Q-7) hexagons. With this in mind, the similarities between these structures and fullerenes (from carbon chemistry) was identified, calling such structures "fullerene-like", and a conjecture has been stated that Skyrmions of any charge $Q \geq 7$ will have the same symmetries as a fullerene from the family $C_{4(Q-2)}$ (called the "fullerene hypothesis"). The most striking example is the $Q = 17$ Skyrmion, which has the same structure as the famous, icosahedrally symmetric, C_{60} fullerene, which has recently been detected in space [23].

2.2 The Skyrme model: a geometrical perspective

In [24], Manton gave a description of the Skyrme model from a geometrical perspective. One of the main ideas in the paper is that the energy of Skyrmions depends on the geometrical distortion produced by a map from a domain manifold S to a target manifold Σ. An obvious choice for a map that produces the least possible amount of distortion would be one that is an isometry, which is what we have considered so far (a map from the unit 3-sphere to the unit 3-sphere: $S^3 \mapsto S^3$). However, one can learn a great deal about the stabilities of maps and about the symmetries of the Skyrme model when one considers the domain manifold to be a 3-sphere of radius R, S^3_R, rather than just a unit 3-sphere.

A way of measuring the geometrical distortion produced by a map π is to consider the strain tensor D. To define the strain tensor, we first need to define coordinates on the domain and target spaces. Let π^α and p^i be normal coordinates on the target space Σ and domain space S, respectively. The Σ coordinates can be expressed as functions of the S coordinates $\pi^\alpha(p^1, p^2, p^3)$ and the strain tensor is then given by: $D^b_a = g^{jk}(\frac{\partial \pi^c}{\partial p^j})H_{ac}(\frac{\partial \pi^b}{\partial p^k})$, where g^{jk} and H_{ac} are the metrics on the manifolds S and Σ, respectively.

The energy density $\mathcal{E} = \mathcal{E}_2 + \mathcal{E}_4$ of the map would then be given by: $\mathcal{E}_2 = \kappa_2 \mathrm{Tr}(D) \equiv \kappa_2(\lambda_1^2 + \lambda_2^2 + \lambda_3^2)$ and $\mathcal{E}_4 = \frac{\kappa_4}{2}[(\mathrm{Tr}D)^2 - \mathrm{Tr}(D^2)] \equiv \kappa_4(\lambda_1^2\lambda_2^2 + \lambda_2^2\lambda_3^2 + \lambda_3^2\lambda_1^2)$, where λ_1^2, λ_2^2, and λ_3^2 are the eigenvalues of the strain tensor and κ_2 and κ_4 are constants, which for now[2] we take to be $\kappa_2 = \kappa_4 = 1$. A map that is an isometry, which produces no distortion, would correspond to the eigenvalues of the strain tensor all being unity (i.e. the strain tensor is the unit matrix). Therefore, one can see the amount of distortion produced by the map by looking at how much the eigenvalues differ from unity. In the case of the Skyrme model, the Skyrmion is a minimal energy solution.

The energy of a map π is given by:

$$E = \int_S (\lambda_1^2 + \lambda_2^2 + \lambda_3^2 + \lambda_1^2\lambda_2^2 + \lambda_2^2\lambda_3^2 + \lambda_3^2\lambda_1^2)\, dS\,. \tag{2.7}$$

Eq. (2.7) can be rewritten as follows:

$$E = \int_S [(\lambda_1 - \lambda_2\lambda_3)^2 + (\lambda_2 - \lambda_3\lambda_1)^2 + (\lambda_3 - \lambda_1\lambda_2)^2]\, dS + 6\int_S \lambda_1\lambda_2\lambda_3\, dS\,. \tag{2.8}$$

It is easy to see from eq. (2.8), since the first three terms are ≥ 0, that:

$$E \geq 6\int_S \lambda_1\lambda_2\lambda_3\, dS\,, \tag{2.9}$$

which is a topological invariant. To see this, note that $\det(D) = \lambda_1^2\lambda_2^2\lambda_3^2$. Therefore, $\lambda_1\lambda_2\lambda_3 = (\det(D))^{1/2} \equiv (\det(JJ^T))^{1/2} = \det(J)$, where J_i^α is the Jacobian $J_i^\alpha = \frac{\partial \pi^\alpha}{\partial p^i}$. The determinant of the Jacobian turns the integration measure on S to the integration measure on Σ, so eq. (2.9) becomes:

$$E \geq 6(\deg\, \pi)(\mathrm{Vol}\, \Sigma)\,, \tag{2.10}$$

[2] A formal definition will be given in sec. 2.4.

where deg π is the degree of the map π.

Note that the topological bound, eq. (2.9), is achieved when $\lambda_1 = \lambda_2 = \lambda_3 = 1$. In other words, when there is no distortion (i.e. whenever we have an isometry), the lower bound is attained. However, for the Skyrme model, the map is from flat 3-space topologically compactified at infinity, to the unit 3-sphere (for which there is no isometry), so this topological bound cannot be attained.

There is a stronger bound than eq. (2.10) when one considers a target manifold that is isotropically bigger than the domain manifold. That is, Vol $\Sigma = \sigma^3$Vol S, where $\sigma > 1$. The new bound can be derived by minimizing the energy, eq. (2.7), with the use of a Lagrange multiplier and the constraint: $\int \lambda_1\lambda_2\lambda_3 = \text{Vol } \Sigma$. After taking these into consideration, one finds that λ_1, λ_2, and λ_3 must be equal to the same constant σ, and the new constraint is given by:

$$E \geq 3\left(\frac{1}{\sigma} + \sigma\right) \text{Vol } \Sigma\,, \tag{2.11}$$

which reduces to eq. (2.10), when $\sigma = 1$ and deg $\pi = 1$.

2.3 The Skyrme-Faddeev model

In 1975, L.D. Faddeev proposed a theory of solitons whose Lagrangian L and associated static energy E we take to be [4, 25–28]:

$$L = \frac{1}{32\pi^2}\int \left\{\partial_\mu\vec{\psi}\cdot\partial^\mu\vec{\psi} - \frac{1}{4}(\vec{\psi}\cdot\partial_\mu\vec{\psi}\times\partial_\nu\vec{\psi})(\vec{\psi}\cdot\partial^\mu\vec{\psi}\times\partial^\nu\vec{\psi})\right\} d^3x\,, \tag{2.12}$$

$$E = \frac{1}{32\pi^2}\int \left\{\partial_i\vec{\psi}\cdot\partial_i\vec{\psi} + \frac{1}{4}(\vec{\psi}\cdot\partial_i\vec{\psi}\times\partial_j\vec{\psi})(\vec{\psi}\cdot\partial_i\vec{\psi}\times\partial_j\vec{\psi})\right\} d^3x\,, \tag{2.13}$$

where $\vec{\psi} = \{\psi^1, \psi^2, \psi^3\} \equiv \psi^a$ is a unit vector $[(\psi^a)^2 = 1]$ that has its domain in $\mathbb{R}^3$; note that we have included a "normalization" factor, which

simplifies the expression for an inequality (as in the Skyrme Model), which we shall mention shortly. The unit vector is a map $\vec{\psi} : \mathbb{R}^3 \mapsto S^2$. As with the Skyrme model, we assume a compactification at spatial infinity, where $\vec{\psi}(\infty) = \{0, 0, 1\}$. This means that, topologically, the map is given by $\vec{\psi} : S^3 \mapsto S^2$ (also known as the Hopf map) and these maps fall into homotopy classes indexed by an integer: $\pi_3(S^2) = \mathbb{Z}$, as was the case with the Skyrme model. The crucial difference here is that these integers, called the Hopf Charge, do not have the interpretation of the degree of the map from a 3-sphere to a 2-sphere, since these manifolds do not have the same dimension. Rather, the Hopf charge has the following definition [10]:

$$N = \frac{1}{4\pi^2} \int_{S^3} f \wedge a \,, \tag{2.14}$$

where f is the pull-back under the map $\vec{\psi}$ of the area 2-form $\varepsilon_{abc}\psi^a d\psi^b d\psi^c$ and a is a 1-form, such that $f = da$. Note that the integral (2.14) is independent of the choice of a.

Recall that the Skyrme charge Q is given the interpretation of the baryon number, in a sense counting the number of skyrmions in a system. The Hopf charge is entirely different. Points on the target manifold S^2 correspond to Hopf solitons. The preimages of these can be visualized as circles[3] , which can be linked any number of times - this number being the Hopf charge.

The string-like solutions of the Skyrme-Faddeev Model (called Hopf solitons or hopfions), which are generally linked and knotted for high enough values of N, have been studied extensively (see e.g. [26–28, 30–39]). As with the Skyrme model, there is a lower bound on the energy given in terms of the topological charge. However, it is very different in nature and does not arise

[3]Note that the Hopf map can be visualized as a 3-sphere embedded in $\mathbb{C}^2$. The set of lines that pass through the origin in $\mathbb{C}^2 : Aw + Bz = 0$, where A and B are complex numbers not both equal to zero, produce circles when they intersect the 3-sphere. The ratio of complex numbers $A : B$ corresponds to different points of the base manifold S^2 and the circles we mentioned earlier are the fibers of this so-called Hopf fibration (see e.g. [29]).

from the usual Bogomolny-type argument, as it involves a fractional power of the charge [27, 40, 41]: $E \geq |N|^{3/4}$.

Hopfions can be visualized by depicting the curve in space corresponding to the preimage of the vector $\psi^3 = -1$, which is antipodal to the vacuum value of $\psi^3 = 1$. In practice, one takes a value of ψ^3 close to -1 (a circle of vectors where ψ^3 is close to -1), which has the effect of thickening the position curve of the hopfion. Note that the Skyrme-Faddeev Model has a global O(3) symmetry but, by specifying the point $\psi^3 = 1$ to be the vacuum, this is broken to O(2), whose elements rotate the $\{\psi^1, \psi^2\}$ components of the field. One way the charge of a hopfion can be determined is to take two points: one corresponding to the position of the hopfion and some other point, and looking at the number of times their preimages (the position curve and the linking curve) link with each other – this being equal to the hopf charge.

A catalogue of minimal-energy hopfions, up to $N = 16$, has been compiled in [38]. Some notable examples include the hopfions with charge $N = 1$ (whose position curve looks like a torus), $N = 3$ (a twisted torus), $N = 5$ (the first example of a link with two disconnected components), and $N = 7$ (the first example of a knot), with higher charges featuring a higher number of links and twists. A way to determine the charge of a linked hopfion is to add the number of links to the charge of each individual component, then add this result for all components. For example, the $N = 8$ hopfion consists of two charge 3 components, which link once around each other. The charge is then given by $N = (3 + 1) + (3 + 1) = 8$.

One important consequence of the fact that hopfion energies (as a function of charge) closely follow the bound mentioned above is that it is energetically preferable for them to be tightly bound, rather than being a conglomeration of charge 1 hopfions. Moreover, if one normalizes the energy of the $N = 1$ hopfion, such that it coincides with the energy of the $Q = 1$ skyrmion (see sec. 2.4), then as N and Q approach infinity, the tangled twists and loops of

the hopfion system will be more tightly bound than the skyrme system, which is thought to resemble the Skyrme crystal in this limit (see sec. 2.5). This can be readily seen from their binding energy per charge[4]: $\Delta E/Q = E_1 - (E/Q)$, where E_1 is the energy of the $Q = 1$ or $N = 1$ soliton (see tables in [10, 38]).

2.4 Generalized Skyrme systems

2.4.1 Overview

It has been pointed out in [4] that the Skyrme and Skyrme-Faddeev models summarized earlier are members of a family of generalized Skyrme systems, parametrized by $\alpha \in [0, 1]$. In this section we give a brief overview of the results from [4] and in sec. 2.4.2 we give an outline of the steps involved in getting these results. We shall be using the sign conventions from [4] throughout this section as we shall be following it closely; these differ slightly for the Lagrangian densities from secs. 2.1 and 2.3 (where we used the conventions from [10]). However, the important expressions which we use extensively in all subsequent chapters are the static energy densities. When these are expressed in terms of the fields Φ_β or $\vec{\psi}$, it is always the case that for all models under consideration its terms are positive.

Since the Skyrme and Skyrme-Fadeev models feature fields which are maps: $S^3 \mapsto S^3$ and $S^3 \mapsto S^2$ respectively, it would be useful to have a metric that interpolates between S^3 and S^2. One such metric exists, corresponding to a "squashed" 3-sphere S^3_α, sometimes called the Berger sphere:

$$ds^2 = dZ^\dagger dZ + \alpha(Z^\dagger dZ)(Z^\dagger dZ) \tag{2.15}$$

$$\equiv G - \alpha\omega \otimes \omega\,, \tag{2.16}$$

where $Z = (Z_1, Z_2)^T$ is a complex 2-vector satisfying $Z^\dagger Z = |Z_1|^2 + |Z_2|^2 = 1$.

[4]The energy needed to separate a $Q-$soliton into Q $1-$solitons.

Note that when $\alpha = 0$, one has the regular 3-sphere metric and when $\alpha = 1$, one gets the standard 2-sphere metric, which is harder to see. It is easier to see this if one thinks of a unit vector field ξ^j, which is obtained from the 1-form $\omega = -iZ^\dagger dZ$ through use of the 3-sphere metric G. It turns out [4] that ξ^j is tangent to the fibers of the Hopf fibration and when $\alpha \to 1$, the length of these vectors goes to zero, thus effectively producing a 2-sphere. In other words, when $\alpha = 1$, ξ^j becomes a zero eigenvector of the metric (2.15), which therefore becomes degenerate. Otherwise, when $0 \leq \alpha < 1$, the metric is positive-definite.

The Lagrangian density of the generalized Skyrme system is given by [4]:

$$\begin{aligned} \mathcal{L}_{\text{gen}} &= \mathcal{L}_2 + \mathcal{L}_4 \,, && (2.17) \\ \mathcal{L}_2 &= \kappa_2 g^{\mu\nu}(M^a_\mu M^a_\nu - \alpha M^3_\mu M^3_\nu) \,, && (2.18) \\ \mathcal{L}_4 &= \frac{1}{8}\kappa_4 g^{\mu\nu} g^{\beta\gamma}[(1-\alpha)K^a_{\mu\beta}K^a_{\nu\gamma} + \alpha K^3_{\mu\beta}K^3_{\nu\gamma}] \,, && (2.19) \end{aligned}$$

where, if we need to contract certain terms with the spacetime metric $g^{\mu\nu}$, we take it to be flat with signature $(+---)$, and derivatives with respect to the spacetime coordinates x^μ are used in M_μ and $K_{\mu\nu}$ as follows:

$$\begin{aligned} M_\mu &= iM^a_\mu \sigma_a = U^\dagger \partial_\mu U \,, && (2.20) \\ K_{\mu\nu} &= iK^a_{\mu\nu}\sigma_a = [M_\mu, M_\nu] \,, && (2.21) \end{aligned}$$

where $\sigma_a \equiv \sigma^a$ are the triplet of Pauli matrices. Furthermore, U is a matrix determined by the complex 2-vector Z as follows:

$$U = \begin{pmatrix} Z_1 & -Z_2^* \\ Z_2 & Z_1^* \end{pmatrix} .$$

When the field $Z(x^j)$ is an identity map $S^3 \mapsto S^3_\alpha$, the energy of the gener-

alized Skyrme system is given by[5]:

$$E = 2\pi^2(3-\alpha)\kappa_2 + 2\pi^2(3-2\alpha)\kappa_4\,. \tag{2.22}$$

The factors κ_2 and κ_4 in (2.18, 2.19, 2.22) are coupling constants, which can be scaled as desired. For our purposes, we choose the following "geometrical" choice, for which the identity map has unit energy for $\alpha \in [0,1]$ (i.e. $E_2 = E_4 = \frac{1}{2}$) [4]:

$$\kappa_2 = 1/[4\pi^2(3-\alpha)]\,, \tag{2.23}$$

$$\kappa_4 = 1/[4\pi^2(3-2\alpha)]\,. \tag{2.24}$$

Moreover, with the geometrical choice, the energy of the 1-skyrmion on $\mathbb{R}^3$ is approximately constant as a function of α ($E \approx 1.22$).

When $\alpha = 0$, the generalized Lagrangian reduces to the standard Skyrme Lagrangian (2.1) and, in the $\alpha = 1$ limit, if one replaces Z by the unit 3-vector $\psi^a = Z^\dagger \sigma_a Z$ (which is just another form of the Hopf map) then the generalized Lagrangian becomes [4]:

$$\mathcal{L}_{\mathrm{SF}} = \frac{\kappa_2}{4}(\partial_\mu \psi^a)^2 + \frac{\kappa_4}{32}(\varepsilon_{abc}\psi^a(\partial_\mu\psi^b)(\partial_\nu\psi^c))^2\,, \tag{2.25}$$

which is the Skyrme-Faddeev Lagrangian. Note that the squared terms here (and for the rest of this section) imply repeated indices, which are assumed to be contracted, e.g. through the use of a metric which, as stated earlier, we assume to be flat with signature $(+---)$.

We shall show in the next section how one can get to the following expression for the generalized static energy density [1] from the generalized Lagrangian

[5]See sec. 5.1 for its derivation.

(2.17)-(2.19):

$$\mathcal{E} = \kappa_2[(\partial_j \Phi_\beta)^2 - \alpha(P_j)^2] + \kappa_4[2(1-\alpha)(F^j_{\beta\gamma})^2 + \alpha(Q^j)^2]\,, \tag{2.26}$$

where

$$\begin{aligned} P_j &= \Omega^{\beta\gamma}\Phi_\beta \partial_j \Phi_\gamma\,, \\ F^j_{\beta\gamma} &= \frac{1}{2}\varepsilon^{jkl}(\partial_k \Phi_\beta)(\partial_l \Phi_\gamma)\,, \\ Q^j &= \Omega^{\beta\gamma} F^j_{\beta\gamma}\,, \end{aligned}$$

and where $\Omega_{\beta\gamma}$ is a symplectic form, which has the following non-zero components: $\Omega_{12} = -\Omega_{21} = -\Omega_{34} = \Omega_{43} = 1$.

2.4.2 Calculations

The origins of the generalized Lagrangian from the previous section, eqs. (2.18) and (2.19), might seem mysterious. Therefore, in this section we will provide an outline of their derivation, starting from the Berger sphere metric, eq. (2.15). Moreover, it is not entirely clear how one gets to the form of the generalized energy density (2.26) in terms of the fields Φ_μ, from the generalized Lagrangian. In the second part, we will provide an outline of this. Finally, in the last part, we prove that the generalized Lagrangian in the $\alpha = 1$ limit is equivalent to the Skyrme-Faddeev Lagrangian, eq. (2.25).

Derivation of Generalized Lagrangian

The Berger sphere metric can be expressed as follows:

$$\begin{aligned} ds^2 &= H_{jk}\, dx^j dx^k && (2.27)\\ &= \left(\partial_j Z^\dagger \partial_k Z \delta^{jk} + \alpha(Z^\dagger \partial_j Z)(Z^\dagger \partial_k Z)\right) dx^j dx^k && (2.28)\\ &\equiv (\partial_j Z^\dagger \partial_k Z \delta^{jk} - \alpha \xi_j \xi_k) dx^j dx^k\,, && (2.29) \end{aligned}$$

where we have used the symbol δ^{jk} to emphasize that the first term consists of only diagonal components and we have defined $\xi_j \equiv -iZ^\dagger \partial_j Z$.

Recall from sec. 2.2 that the distortion tensor is given by:

$$D_a^b = G^{jk}\left(\frac{\partial \pi^c}{\partial p^j}\right) H_{ac}\left(\frac{\partial \pi^b}{\partial p^k}\right) \equiv G^{jk} H_{ac} \pi_j^c \pi_k^b \,, \tag{2.30}$$

where now the metrics of the domain and target manifolds are given by the unit 3-sphere metric G^{jk} and the squashed 3-sphere metric H_{ac}, respectively:

$$G_{jk} = \partial_j Z^\dagger \partial_k Z \delta^{jk}, \tag{2.31}$$

$$H_{ac} = G_{ac} - \alpha \xi_a \xi_c \,. \tag{2.32}$$

If we focus on the $\alpha = 0$ case for the moment, one can see where the M_i^a terms come from. Using eq. (2.32) we have $H_{ac} = G_{ac}$ and, given the distortion tensor (2.30) and the fact that the spatial part of $\mathcal{L}_2$ is given by the static energy density $\mathcal{E}_2 = \kappa_2 \mathrm{Tr}(D)$, one can almost immediately see that $\mathcal{E}_2 = \kappa_2 g^{jk} \pi_j^a \pi_k^a$. This is of the form of the $\alpha = 0$ term in eq. (2.18). Since the π_j^a involve the derivatives of the fields π^a, much like the M_j^a involve the spatial derivatives of the fields U, we assume for now that they are equivalent objects: $\pi_j^a \equiv M_j^a$. We shall see that this assumption leads to certain expressions for the energy and Lagrangian densities which are consistent with the Skyrme Model, in the $\alpha = 0$ limit, and with the Skyrme-Faddeev Model, in the $\alpha = 1$ limit.

For $\alpha \neq 0$, we need an expression for ξ_j in terms of the M_i^a's. For such

purposes, we note that:

$$M_j \equiv U^\dagger \partial_j U \tag{2.33}$$

$$= \begin{pmatrix} Z_1^* & Z_2^* \\ -Z_2 & Z_1 \end{pmatrix} \begin{pmatrix} \partial_j Z_1 & -\partial_j Z_2^* \\ \partial_j Z_2 & \partial_j Z_1^* \end{pmatrix} \tag{2.34}$$

$$= \begin{pmatrix} Z_1^* \partial_j Z_1 + Z_2^* \partial_j Z_2 & -Z_1^* \partial_j Z_2^* + Z_2^* \partial_j Z_1^* \\ -Z_2 \partial_j Z_1^* + Z_1 \partial_j Z_2 & Z_2 \partial_j Z_2^* + Z_1 \partial_j Z_1^* \end{pmatrix}, \tag{2.35}$$

which yields the following:

$$\frac{1}{2}\mathrm{Tr}(M_j \sigma_3) = \frac{1}{2}(Z_1^* \partial_j Z_1 + Z_2^* \partial_j Z_2 - Z_1 \partial_j Z_1^* - Z_2 \partial_j Z_2^*) \tag{2.36}$$

$$= Z_1^* \partial_j Z_1 + Z_2^* \partial_j Z_2 \tag{2.37}$$

$$= Z^\dagger \partial_j Z, \tag{2.38}$$

where use of the identity $\partial_j (Z^\dagger Z) = 0$ has been made to simplify the expression. Thus, we have:

$$\begin{aligned} \xi_j &\equiv -iZ^\dagger \partial_j Z = -\frac{i}{2}\mathrm{Tr}(M_j \sigma_3) = \frac{1}{2}\mathrm{Tr}(M_j^a \sigma_a \sigma_3) = \frac{1}{2}\mathrm{Tr}\left(M_j^a (\delta_{a3} + i\varepsilon_{a3c}\sigma_c)\right) \\ &= \frac{1}{2}\mathrm{Tr}(M_j^3) \text{ (since } \mathrm{Tr}(\sigma_c) = 0) \\ &\equiv M_j^{3'} \text{ (since } M_j^3 \equiv M_j^{3'} \times \mathbb{1}) \\ &= M_j^{a'} n_a, \text{ where } n_a \equiv (0,0,1)\,. \end{aligned} \tag{2.39}$$

From now on we write $M_j^{a'}$ as simply M_j^a. Therefore, $\xi_j = M_j^a n_a \equiv M_j^a \xi_a$, where ξ_a are the (vector) components of ξ_j. We can now write the generalized distortion tensor as follows:

$$\begin{aligned} D_a^b &= G^{jk}(G_{ac} - \alpha \xi_a \xi_c) M_j^c M_k^b \\ &= G^{jk}(G_{ac} - \alpha n_a n_c) M_j^c M_k^b\,. \end{aligned} \tag{2.40}$$

The static energy density $\mathcal{E}_2$ is given by the trace of the distortion tensor:

$$\mathcal{E}_2 = \kappa_2 \mathrm{Tr}(D) = \kappa_2 g^{jk}(M_j^a M_k^a - \alpha M_j^3 M_k^3)\,. \tag{2.41}$$

Since $\mathcal{E}_2$ is taken to be the spatial part of $\mathcal{L}_2$, one can write the more general Larangian as follows:

$$\mathcal{L}_2 = \kappa_2 g^{\mu\nu}(M_\mu^a M_\nu^a - \alpha M_\mu^3 M_\nu^3)\,, \tag{2.42}$$

as in eq. (2.18).

We can now derive the rest of the terms in the Lagrangian by using the fact that $\mathcal{E}_4 = \frac{\kappa_4}{2}[(\mathrm{Tr}(D))^2 - \mathrm{Tr}(D^2)]$:

$$\begin{aligned}(\mathrm{Tr}(D))^2 &= g^{jk}g^{lm}(\delta_{ab} - \alpha n_a n_b)(\delta_{cd} - \alpha n_c n_d) M_j^a M_k^b M_l^c M_m^d \\ &= g^{jk}g^{lm}[\delta_{ab}\delta_{cd} - \alpha(\delta_{ab}n_c n_d + \delta_{cd}n_a n_b) + \alpha^2 n_a n_b n_c n_d] M_j^a M_k^b M_l^c M_m^d \\ &= g^{jk}g^{lm}[M_j^a M_k^a M_l^c M_m^c - \alpha(M_j^a M_k^a M_l^3 M_m^3 + M_l^c M_m^c M_j^3 M_k^3) \\ &\qquad + \alpha^2 M_j^3 M_k^3 M_l^3 M_m^3].\end{aligned} \tag{2.43}$$

$$\begin{aligned}\mathrm{Tr}(D^2) &= g^{jk}g^{lm}(\delta_{ac} - \alpha n_a n_c)(\delta_{bf} - \alpha n_b n_f) M_l^f M_m^a M_j^c M_k^b \\ &= g^{jk}g^{lm}[\delta_{ac}\delta_{bf} - \alpha(\delta_{ac}n_b n_f + \delta_{bf}n_a n_c) + \alpha^2 n_a n_c n_b n_f] M_j^c M_k^b M_l^f M_m^a \\ &= g^{jk}g^{lm}[M_j^a M_m^a M_k^b M_l^b - \alpha(M_j^a M_m^a M_k^3 M_l^3 + M_k^b M_l^b M_j^3 M_m^3) \\ &\qquad + \alpha^2 M_j^3 M_m^3 M_k^3 M_l^3].\end{aligned} \tag{2.44}$$

In what follows, we shall make use of the following notation:

$M^a_{[k}M^b_{m]} \equiv \frac{1}{2}(M^a_k M^b_m - M^a_m M^b_k) = M^{[a}_k M^{b]}_m$.

$$
\begin{aligned}
(\mathrm{Tr}(D))^2 - \mathrm{Tr}(D^2) &= g^{jk}g^{lm}[M^a_j M^b_l (2M^a_{[k}M^b_{m]}) \\
&\qquad - \alpha\left(M^a_j M^3_l (2M^a_{[k}M^3_{m]}) + M^b_l M^3_j (2M^b_{[m}M^3_{k]})\right)] \\
&= g^{jk}g^{lm}[M^a_{[j}M^b_{l]}M^a_{[k}M^b_{m]} - \alpha(M^a_{[j}M^3_{l]}M^a_{[k}M^3_{m]} + M^b_{[l}M^3_{j]}M^b_{[m}M^3_{k]})] \\
&= g^{jk}g^{lm}[M^{[a}_j M^{b]}_l M^{[a}_k M^{b]}_m - \alpha(M^{[a}_j M^{3]}_l M^{[a}_k M^{3]}_m + M^{[b}_j M^{3]}_l M^{[b}_k M^{3]}_m)] \\
&= g^{jk}g^{lm}[M^{[1}_j M^{b]}_l M^{[1}_k M^{b]}_m + M^{[2}_j M^{b]}_l M^{[2}_k M^{b]}_m + M^{[3}_j M^{b]}_l M^{[3}_k M^{b]}_m \\
&\qquad - 2\alpha(M^{[1}_j M^{3]}_l M^{[1}_k M^{3]}_m + M^{[2}_j M^{3]}_l M^{[2}_k M^{3]}_m)] \\
&= 2g^{jk}g^{lm}[M^{[1}_j M^{2]}_l M^{[1}_k M^{2]}_m + M^{[1}_j M^{3]}_l M^{[1}_k M^{3]}_m + M^{[2}_j M^{3]}_l M^{[2}_k M^{3]}_m \\
&\qquad - \alpha(M^{[1}_j M^{3]}_l M^{[1}_k M^{3]}_m + M^{[2}_j M^{3]}_l M^{[2}_k M^{3]}_m)] \\
&= 2g^{jk}g^{lm}[(1-\alpha)(M^{[1}_j M^{2]}_l M^{[1}_k M^{2]}_m + M^{[1}_j M^{3]}_l M^{[1}_k M^{3]}_m + M^{[2}_j M^{3]}_l M^{[2}_k M^{3]}_m) \\
&\qquad + \alpha M^{[1}_j M^{2]}_l M^{[1}_k M^{2]}_m] \\
&= \frac{1}{4}g^{jk}g^{lm}[(1-\alpha)[M_j, M_l]^a[M_k, M_m]^a + \alpha[M_j, M_l]^3[M_k, M_m]^3].
\end{aligned}
\tag{2.45}
$$

In the last line, we have defined the following: $[M_j, M_l]^c \equiv -\varepsilon_{abc}M^a_j M^b_l = -2M^{[a}_j M^{b]}_l$, where c is a fixed constant, and therefore, $\{a, b\}$ take only two values.

We now have:

$$\mathcal{E}_4 = \frac{\kappa_4}{8}g^{jk}g^{lm}[(1-\alpha)[M_j, M_l]^a[M_k, M_m]^a + \alpha[M_j, M_l]^3[M_k, M_m]^3] \tag{2.46}$$

$$\mathcal{L}_4 = \frac{\kappa_4}{8}g^{\mu\nu}g^{\beta\gamma}[(1-\alpha)[M_\mu, M_\beta]^a[M_\nu, M_\gamma]^a + \alpha[M_\mu, M_\beta]^3[M_\nu, M_\gamma]^3]. \tag{2.47}$$

Derivation of Generalized Energy Density

We now look at how one can arrive at the expression of the energy density, given in terms of the fields Φ_β (eq. (2.26)), from the generalized Lagrangian, eqs. (2.18, 2.19).

In what follows, Greek indices $(\alpha, \beta, \gamma, ...) \in (1, 2, 3, 4)$ and Latin indices $(a, b, c, ...) \in (1, 2, 3)$ which, when repeated, should be thought of as being contracted (or summed over). Furthermore, we shall make use of the following definitions and identities:

$$\sigma_i = \left\{ \begin{pmatrix} 0 & 1 \\ 1 & 0 \end{pmatrix}, \begin{pmatrix} 0 & -i \\ i & 0 \end{pmatrix}, \begin{pmatrix} 1 & 0 \\ 0 & -1 \end{pmatrix} \right\}; \tag{i}$$

$$[\sigma_i, \sigma_j] = 2i\varepsilon_{ijk}\sigma_k \qquad , \qquad \sigma_i\sigma_j = \delta_{ij} \cdot \mathbb{1} + i\varepsilon_{ijk}\sigma_k \,; \tag{ii,iii}$$

$$U = \Phi_4 + i\Phi_i\sigma_i \qquad , \qquad U^\dagger = \Phi_4 - i\Phi_i\sigma_i \,; \tag{iv,v}$$

$$U = \begin{pmatrix} Z_1 & -Z_2^* \\ Z_2 & Z_1^* \end{pmatrix} = \begin{pmatrix} \Phi_4 + i\Phi_3 & \Phi_2 + i\Phi_1 \\ -\Phi_2 + i\Phi_1 & \Phi_4 - i\Phi_3 \end{pmatrix}; \tag{vi}$$

$$\Phi_\beta\Phi_\beta = 1 \qquad , \qquad \Phi_\beta\partial_i\Phi_\beta = 0 \,; \tag{vii,viii}$$

$$M_i = iM_i^a\sigma_a \,, \qquad M_i^\dagger = -M_i, \qquad (M_i^a)^\dagger = M_i^a \,, \qquad [M_i^a, \sigma_a] = 0 \,, \tag{ix-xii}$$

where identities (x) and (xi) follow from $M_iM_i^\dagger = -M_i^2$ and from the Hermiticity of Pauli matrices $\sigma_a = \sigma_a^\dagger$, respectively.

To calculate $\mathcal{E}_2$ we first need to write down expressions for the M_i^a's in terms

of the fields Φ_β. We begin by writing down M_i as follows:

$$\begin{aligned}
M_i &= U^\dagger \partial_i U = (\Phi_4 - i\Phi_j\sigma_j)(\partial_i\Phi_4 + i(\partial_i\Phi_k)\sigma_k) \\
&= \Phi_4\partial_i\Phi_4 + i(\Phi_4(\partial_i\Phi_k)\sigma_k - \Phi_j(\partial_i\Phi_4)\sigma_j) + \Phi_j(\partial_i\Phi_k)\sigma_j\sigma_k \\
&= -i\cdot i[\Phi_4\partial_i\Phi_4 + i\Phi_4((\partial_i\Phi_1)\sigma_1 + (\partial_i\Phi_2)\sigma_2 + (\partial_i\Phi_3)\sigma_3) \\
&\quad - i\partial_i\Phi_4(\Phi_1\sigma_1 + \Phi_2\sigma_2 + \Phi_3\sigma_3) \\
&\quad + (\Phi_1\sigma_1 + \Phi_2\sigma_2 + \Phi_3\sigma_3)((\partial_i\Phi_1)\sigma_1 + (\partial_i\Phi_2)\sigma_2 + (\partial_i\Phi_3)\sigma_3)]. \qquad (2.48)
\end{aligned}$$

Using identities (iii) and (viii) on eq. (2.48) simplifies it considerably. We can now write it down as follows:

$$\begin{aligned}
M_i = i[&\Phi_4((\partial_i\Phi_1)\sigma_1 + (\partial_i\Phi_2)\sigma_2 + (\partial_i\Phi_3)\sigma_3) - \partial_i\Phi_4(\Phi_1\sigma_1 + \Phi_2\sigma_2 + \Phi_3\sigma_3) \\
&+ (\Phi_1\partial_i\Phi_2)\sigma_3 - (\Phi_1\partial_i\Phi_3)\sigma_2 - (\Phi_2\partial_i\Phi_1)\sigma_3 \\
&+ (\Phi_2\partial_i\Phi_3)\sigma_1 + (\Phi_3\partial_i\Phi_1)\sigma_2 - (\Phi_3\partial_i\Phi_2)\sigma_1]. \qquad (2.49)
\end{aligned}$$

From eq. (2.49), we can read out the individual M_i^a's:

$$\begin{aligned}
M_i^1 &= (\Phi_4\partial_i\Phi_1 - \Phi_1\partial_i\Phi_4 + \Phi_2\partial_i\Phi_3 - \Phi_3\partial_i\Phi_2)\times\mathbb{1} && (2.50)\\
&= \frac{i}{2}(Z_1^*\partial_i Z_2^* - Z_1\partial_i Z_2 + Z_2\partial_i Z_1 - Z_2^*\partial_i Z_1^*)\times\mathbb{1}\,, && (2.51)\\
M_i^2 &= (\Phi_4\partial_i\Phi_2 - \Phi_2\partial_i\Phi_4 + \Phi_3\partial_i\Phi_1 - \Phi_1\partial_i\Phi_3)\times\mathbb{1} && (2.52)\\
&= \frac{1}{2}(Z_2^*\partial_i Z_1^* + Z_2\partial_i Z_1 - Z_1\partial_i Z_2 - Z_1^*\partial_i Z_2^*)\times\mathbb{1}\,, && (2.53)\\
M_i^3 &= (\Phi_4\partial_i\Phi_3 - \Phi_3\partial_i\Phi_4 + \Phi_1\partial_i\Phi_2 - \Phi_2\partial_i\Phi_1)\times\mathbb{1} && (2.54)\\
&= i(Z_1\partial_i Z_1^* + Z_2\partial_i Z_2^*)\times\mathbb{1}\,. && (2.55)
\end{aligned}$$

Note that eq. (2.55) does not seem to be real, but in fact it is. To see this, one can use identity (vi) to expand it in terms of the fields Φ_β and use identity

(viii) to simplify it.

We can now calculate the $\alpha = 0$ term of $\mathcal{L}_2$, eq. (2.18):

$$\begin{aligned}\frac{1}{2}\mathrm{Tr}(M_i^a)^2 &= ({\Phi_2}^2 + {\Phi_3}^2 + {\Phi_4}^2)(\partial_i\Phi_1)^2 + ({\Phi_1}^2 + {\Phi_3}^2 + {\Phi_4}^2)(\partial_i\Phi_2)^2 \\ &\quad + ({\Phi_1}^2 + {\Phi_2}^2 + {\Phi_4}^2)(\partial_i\Phi_3)^2 + ({\Phi_1}^2 + {\Phi_2}^2 + {\Phi_3}^2)(\partial_i\Phi_4)^2 \\ &\quad - 2\Phi_1\Phi_4\partial_i\Phi_1\partial_i\Phi_4 - 2\Phi_2\Phi_3\partial_i\Phi_2\partial_i\Phi_3 - 2\Phi_2\Phi_4\partial_i\Phi_2\partial_i\Phi_4 \\ &\quad - 2\Phi_1\Phi_3\partial_i\Phi_1\partial_i\Phi_3 - 2\Phi_3\Phi_4\partial_i\Phi_3\partial_i\Phi_4 - 2\Phi_1\Phi_2\partial_i\Phi_1\partial_i\Phi_2 \quad (2.56) \\ &= (\partial_i\Phi_1)^2 + (\partial_i\Phi_2)^2 + (\partial_i\Phi_3)^2 + (\partial_i\Phi_4)^2 \\ &\quad - (\underbrace{\Phi_1\partial_i\Phi_1 + \Phi_2\partial_i\Phi_2 + \Phi_3\partial_i\Phi_3 + \Phi_4\partial_i\Phi_4}_{0 \text{ (from identity (viii))}})^2 . \quad (2.57)\end{aligned}$$

Therefore[6],

$$\frac{1}{2}\mathrm{Tr}(M_i^a)^2 = (\partial_i\Phi_\beta)^2 , \quad (2.58)$$

$$\frac{1}{2}\mathrm{Tr}(M_i^3)^2 = (\Phi_4\partial_i\Phi_3 - \Phi_3\partial_i\Phi_4 + \Phi_1\partial_i\Phi_2 - \Phi_2\partial_i\Phi_1)^2 \equiv P_i^2 . \quad (2.59)$$

We are now ready to write down the energy density[7] $\mathcal{E}_2$:

$$\mathcal{L}_2 = -\kappa_2((\partial_i\Phi_\beta)^2 - \alpha P_i^2) = -\mathcal{E}_2 . \quad (2.60)$$

To write down the terms in $\mathcal{L}_4$, eq. (2.19), in terms of the fields Φ_β, we develop some special notation which emphasizes the vectorial nature of the terms involved: $\Phi_i \equiv \vec{\phi}$, $\Phi_4 \equiv \phi^0$, $M_\mu^a \equiv \vec{m}_\mu$ (i.e. $M_\mu = i\vec{m}_\mu \cdot \vec{\sigma}$), and their derivatives are given as subscripts (i.e. $\partial_\mu U \equiv U_\mu$, etc.). Using this notation, we now write down some useful expressions:

[6]Note that, because the M_i^a's are proportional to $\mathbb{1}$, whenever we take the trace of terms involving them, we must multiply by a factor of $\frac{1}{2}$ – otherwise we end up double counting the terms.

[7]Note that one can relate the energy density and the Lagrangian, through the energy-momentum tensor T_μ^ν, as follows: $T_\mu^\nu = \left(\frac{\partial\mathcal{L}}{\partial\Phi_{,\nu}}\right)\cdot\Phi_{,\mu} - \mathcal{L}\,\delta_\mu^\nu$, where $\Phi_{,\mu} \equiv \partial_\mu\Phi$. The energy density is given by the T_0^0 component: $\mathcal{E} \equiv T_0^0 = \left(\frac{\partial\mathcal{L}}{\partial\dot{\Phi}}\right)\cdot\dot{\Phi} - \mathcal{L}$, where $\dot{\Phi} \equiv \partial_t\Phi$. Since we are dealing only with static fields, we have: $\mathcal{L} = -\mathcal{E}$.

$$U = \phi^0 + i\vec{\phi}\cdot\vec{\sigma} \equiv \phi^0 + \Phi \qquad , \qquad U^\dagger = \phi^0 - i\vec{\phi}\cdot\vec{\sigma} \equiv \phi^0 - \Phi\,; \quad \text{(xiii,xiv)}$$

$$\phi^\alpha\phi^\alpha = 1 \qquad , \qquad \phi^\alpha\phi^\alpha_\mu = 0\,; \quad \text{(xv,xvi)}$$

$$M_\mu = U^\dagger U_\mu = \phi^0\Phi_\mu - \phi^0_\mu\Phi + i\varepsilon_{ijk}\phi^i\phi^j_\mu\sigma_k \quad , \quad \vec{m}_\mu = \phi^0\vec{\phi}_\mu - \phi^0_\mu\vec{\phi} + \vec{\phi}\times\vec{\phi}_\mu\,; \quad \text{(xvii, xviii)}$$

$$\vec{m}_\mu\cdot\vec{m}_\mu = (\phi^\alpha_\mu)^2 \qquad , \qquad \vec{m}_\mu\cdot\vec{m}_\nu = \phi^0_\mu\phi^0_\nu + \vec{\phi}_\mu\cdot\vec{\phi}_\nu = \phi^\alpha_\mu\phi^\alpha_\nu\,. \quad \text{(xix,xx)}$$

We now focus on the $(1-\alpha)$ term of eq. (2.19). First, we write down $K_{\mu\nu}$ in terms of the m^a_μ's (see eqs. (2.20,2.21)):

$$\begin{aligned} K_{\mu\nu} &= [M_\mu, M_\nu] = [im^a_\mu\sigma_a, im^b_\nu\sigma_b] \\ &= -m^a_\mu m^b_\nu[\sigma_a,\sigma_b] = -2i\varepsilon_{abc}m^a_\mu m^b_\nu\sigma_c \equiv iK^c_{\mu\nu}\sigma_c\,. \end{aligned} \tag{2.61}$$

Therefore,

$$K^a_{\mu\nu} = -2\varepsilon_{abc}m^b_\mu m^c_\nu \times \mathbb{1} = -2(\vec{m}_\mu\times\vec{m}_\nu)\cdot\mathbb{1}\,, \tag{2.62}$$

$$\begin{aligned} \frac{1}{8}\mathrm{Tr}(K^a_{\mu\nu})^2 &= (\vec{m}_\mu\times\vec{m}_\nu)\cdot(\vec{m}_\mu\times\vec{m}_\nu) \\ &= (\vec{m}_\mu\cdot\vec{m}_\mu)(\vec{m}_\nu\cdot\vec{m}_\nu) - (\vec{m}_\mu\cdot\vec{m}_\nu)(\vec{m}_\mu\cdot\vec{m}_\nu)\,. \end{aligned} \tag{2.63}$$

Making use of the identities (xix,xx), we can also express the $(1-\alpha)$ term

of $\mathcal{L}_4$ in terms of the fields ϕ^α_μ:

$$\frac{1}{8}\mathrm{Tr}(K^a_{\mu\nu})^2 = \sum_\alpha (\phi^\alpha_\mu)^2(\phi^\alpha_\nu)^2 - (\phi^\alpha_\mu\phi^\alpha_\nu)^2 \tag{2.64}$$

$$= \sum_\alpha \Big[\Big((\phi^\alpha_1)^2(\phi^\alpha_2)^2 + (\phi^\alpha_1)^2(\phi^\alpha_3)^2 + (\phi^\alpha_2)^2(\phi^\alpha_3)^2\Big) - \Big((\phi^\alpha_1\phi^\alpha_2)^2 + (\phi^\alpha_1\phi^\alpha_3)^2 + (\phi^\alpha_2\phi^\alpha_3)^2\Big) \Big] , \tag{2.65}$$

where we have restricted ourselves to spatial derivatives in eq. (2.65).

The $(1-\alpha)$ term of $\mathcal{L}_4$ can also be expressed in terms of the $F^j_{\beta\gamma}$ from eq. (2.26), as follows (recall that summation over repeated indices is implied throughout):

$$\begin{aligned}
\frac{1}{8}\mathrm{Tr}(K^a_{\mu\nu})^2 &= (\phi^\alpha_\mu)^2(\phi^\alpha_\nu)^2 - (\phi^\alpha_\mu\phi^\alpha_\nu)^2 \\
&= \phi^\alpha_\mu\phi^\alpha_\mu\phi^\beta_\nu\phi^\beta_\nu - \phi^\alpha_\mu\phi^\beta_\mu\phi^\alpha_\nu\phi^\beta_\nu \\
&= \phi^\sigma_\mu\phi^\gamma_\mu\phi^\lambda_\nu\phi^\kappa_\nu\left(\delta^{\sigma\gamma}\delta^{\lambda\kappa} - \delta^{\sigma\lambda}\delta^{\gamma\kappa}\right) \\
&= 2\phi^\sigma_\mu\phi^\gamma_\mu\phi^\lambda_\nu\phi^\kappa_\nu\delta^{\sigma[\gamma}\delta^{\lambda]\kappa} \\
&= 2\phi^\sigma_\mu\phi^\gamma_{[\mu}\phi^\lambda_{\nu]}\phi^\kappa_\nu\delta^{\sigma[\gamma}\delta^{\lambda]\kappa} \\
&= 2\phi^\gamma_{[\mu}\phi^\lambda_{\nu]}\phi^\sigma_{[\mu}\phi^\kappa_{\nu]}\delta^{\sigma[\gamma}\delta^{\lambda]\kappa} \\
&= \frac{1}{2}\underbrace{(\varepsilon_{ijk}\phi^\gamma_j\phi^\lambda_k)}_{\equiv 2F^i_{\gamma\lambda}}\underbrace{(\varepsilon_{ipq}\phi^\sigma_p\phi^\kappa_q)}_{\equiv 2F^i_{\sigma\kappa}}\delta^{\sigma[\gamma}\delta^{\lambda]\kappa} \qquad (2.66) \\
&= 2F^i_{\gamma\lambda}F^i_{\sigma\kappa}\delta^{\sigma[\gamma}\delta^{\lambda]\kappa} \\
&= F^i_{\gamma\lambda}F^i_{\gamma\lambda} - F^i_{\gamma\lambda}F^i_{\lambda\gamma} \\
&= 2F^i_{\gamma\lambda}F^i_{\gamma\lambda}\,, \text{ as in eq. (2.26).} \qquad (2.67)
\end{aligned}$$

Note that, in getting to eq. (2.66), we have restricted ourselves to spatial indices only. We now move on to the α term in $\mathcal{L}_4$, which is proportional to $(K^3_{\mu\nu})^2$. We write it down as follows (recalling that $K^a_{\mu\nu} \equiv -2\varepsilon_{abc}m^b_\mu m^c_\nu \times \mathbb{1}$):

$$K^3_{\mu\nu} = -2\varepsilon_{3ab} m^a_\mu m^b_\nu \times \mathbb{1}\,, \tag{2.68}$$

$$(K^3_{\mu\nu})^2 = 4\varepsilon_{3ab}\varepsilon_{3cd} m^a_\mu m^b_\nu m^c_\mu m^d_\nu \times \mathbb{1}\,, \tag{2.69}$$

$$\frac{1}{8}\mathrm{Tr}(K^3_{\mu\nu})^2 = m^1_\mu m^1_\mu m^2_\nu m^2_\nu + m^2_\mu m^2_\mu m^1_\nu m^1_\nu - m^2_\mu m^2_\nu m^1_\mu m^1_\nu - m^1_\mu m^1_\nu m^2_\mu m^2_\nu \tag{2.70}$$

$$\begin{aligned} &= (m^1_\mu m^2_\nu - m^1_\nu m^2_\mu)^2 \\ &= [(\phi^0\phi^1_\mu - \phi^0_\mu\phi^1 + \phi^2\phi^3_\mu - \phi^3\phi^2_\mu)(\phi^0\phi^2_\nu - \phi^0_\nu\phi^2 + \phi^3\phi^1_\nu - \phi^1\phi^3_\nu) \\ &\quad - (\mu \leftrightarrow \nu)]^2 \qquad (2.71) \\ &\qquad\qquad \vdots \\ &= [(\phi^1_\mu\phi^2_\nu - \phi^1_\nu\phi^2_\mu) + (\phi^0_\mu\phi^3_\nu - \phi^0_\nu\phi^3_\mu)]^2\,. \qquad (2.72) \end{aligned}$$

To get from (2.71) to (2.72), one should expand the (squared) expression, which simplifies considerably after using identities (xv,xvi).

Finally, to get this term into its final form, we make use of the symplectic form $\Omega_{\beta\gamma}$ corresponding to the almost-complex structure in $\mathbb{R}^4 \simeq \mathbb{C}^2$, with non-zero components: $\Omega_{12} = -\Omega_{21} = -\Omega_{34} = \Omega_{43} = 1$. This allows us to write the term as follows:

$$\frac{1}{8}\mathrm{Tr}(K^3_{\mu\nu})^2 = \left(\Omega_{\beta\gamma}\phi^\beta_\mu\phi^\gamma_\nu\right)^2 = \left(\Omega_{\beta\gamma}F^i_{\beta\gamma}\right)^2 \equiv (Q^i)^2\,, \tag{2.73}$$

where, in introducing $F^i_{\beta\gamma}$ from eq. (2.66), we have restricted ourselves to spatial indices.

Bringing together eqs. (2.67,2.73), we can write $\mathcal{L}_4$ as follows:

$$\mathcal{L}_4 = \frac{\kappa_4}{8}((1-\alpha)\mathrm{Tr}(K^a_{\mu\nu})^2 + \alpha\mathrm{Tr}(K^3_{\mu\nu})^2) = -\kappa_4[2(1-\alpha)F^i_{\gamma\lambda}F^i_{\gamma\lambda} + \alpha(Q^i)^2] = -\mathcal{E}_4\,. \tag{2.74}$$

Combining eqs. (2.60,2.74), we get the following expression for the generalized

energy density:

$$\mathcal{E} = \mathcal{E}_2 + \mathcal{E}_4 = \kappa_2[(\partial_i \Phi_\beta)^2 - \alpha P_i^2] + \kappa_4[2(1-\alpha)F^i_{\gamma\lambda}F^i_{\gamma\lambda} + \alpha(Q^i)^2]\,, \quad (2.75)$$

which reproduces eq. (2.26).

Skyrme-Faddeev Lagrangian from Generalized Lagrangian

For the final part of our calculation, we show that eq. (2.17) reduces to the Skyrme-Faddeev Lagrangian, eq. (2.25), in the $\alpha = 1$ limit. In this section, we will write down the Lagrangian in terms of the field $Z \equiv (Z_1, Z_2)^T$, from identity (vi) in the previous section. We use the following notation for its derivatives: $\partial_\mu Z \equiv (Z_{\mu 1}, Z_{\mu 2})^T$ and $\partial_\mu Z^* \equiv (Z^*_{\mu 1}, Z^*_{\mu 2})^T$. The corresponding notation for the fields $\vec{\psi}$ (as defined in sec. 2.3) is given by: $\partial_\mu \vec{\psi} \equiv \partial_\mu \psi^a = \psi^a_\mu$, where again repeated roman indices run over $\{1, 2, 3\}$.

We start by writing the generalized Lagrangian, eq. (2.17), in the $\alpha = 1$ limit, along with the Skyrme-Faddeev Lagrangian:

$$\begin{aligned}
\mathcal{L}_{\text{gen}(\alpha=1)} &= \mathcal{L}_{\text{gen}(\alpha=1),2} + \mathcal{L}_{\text{gen}(\alpha=1),4} \\
&= \kappa_2 g^{\mu\nu}(M^a_\mu M^a_\nu - M^3_\mu M^3_\nu) + \frac{\kappa_4}{8} g^{\mu\nu} g^{\beta\gamma} K^3_{\mu\beta} K^3_{\nu\gamma}\,, \qquad (2.76) \\
\mathcal{L}_{\text{SF}} &= \mathcal{L}_{\text{SF},2} + \mathcal{L}_{\text{SF},4} = \frac{\kappa_2}{4}(\vec{\psi}_\mu)^2 + \frac{\kappa_4}{32}(G_{\mu\nu})^2\,, \qquad (2.77)
\end{aligned}$$

where now $G_{\mu\nu} \equiv \vec{\psi} \cdot (\vec{\psi}_\mu \times \vec{\psi}_\nu)$. However, since we are dealing with spatial indices only, the important terms that we should keep in mind are: the M^a_i, which were defined in terms of Z in eqs. (2.51, 2.53, 2.55) and $K^3_{ij} = -2\varepsilon_{3ab} M^a_i M^b_j \times \mathbb{1}$, as in eq. (2.68). We now write some useful identities:

$$Z^\dagger Z = 1 \qquad , \qquad Z^\dagger_\mu Z + Z^\dagger Z_\mu = 0\,; \qquad \text{(xxi,xxii)}$$

$$\vec{\psi} = Z^\dagger \vec{\sigma} Z = (\psi^1, \psi^2, \psi^3) \quad , \quad (\psi^a)^2 = 1 \quad , \quad \psi^a \psi^a_\mu = 0 \, ; \quad \text{(xxiii,xxiv,xxv)}$$

$$\psi^1 = Z_1^* Z_2 + Z_2^* Z_1 \quad , \quad \psi^1_\mu = Z^*_{\mu 1} Z_2 + Z^*_{\mu 2} Z_1 + Z_1^* Z_{\mu 2} + Z_2^* Z_{\mu 1} \, ; \ \text{(xxvi,xxvii)}$$

$$\psi^2 = -iZ_1^* Z_2 + iZ_1 Z_2^* \quad , \quad \psi^2_\mu = -i(Z^*_{\mu 1} Z_2 - Z^*_{\mu 2} Z_1 + Z_1^* Z_{\mu 2} - Z_2^* Z_{\mu 1}) \, ; \quad \text{(xxviii,xxix)}$$

$$\psi^3 = Z_1^* Z_1 - Z_2^* Z_2 \quad , \quad \psi^3_\mu = Z^*_{\mu 1} Z_1 - Z^*_{\mu 2} Z_2 + Z_1^* Z_{\mu 1} - Z_2^* Z_{\mu 2} \, ; \ \text{(xxx,xxxi)}$$

$$(\psi^1_\mu \psi^2_\nu - \psi^1_\nu \psi^2_\mu) = 2i[Z_1 Z_2 Z^*_{\mu 1} Z^*_{\nu 2} + |Z_1|^2 Z_{\mu 2} Z^*_{\nu 2} + |Z_2|^2 Z^*_{\mu 1} Z_{\nu 1} + Z_1^* Z_2^* Z_{\mu 2} Z_{\nu 1} - (\mu \leftrightarrow \nu)] \, ; \quad \text{(xxxii)}$$

$$\begin{aligned}(\psi^1_\mu \psi^3_\nu - \psi^1_\nu \psi^3_\mu) = {} & \left((Z_1)^2 + (Z_2)^2\right) Z^*_{\mu 2} Z^*_{\nu 1} + (Z_1^* Z_2 - Z_1 Z_2^*) Z^*_{\mu 1} Z_{\nu 1} \\ & + \left(|Z_1|^2 + |Z_2|^2\right) Z^*_{\mu 2} Z_{\nu 1} + (Z_1^* Z_2 - Z_1 Z_2^*) Z^*_{\mu 2} Z_{\nu 2} \\ & + \left(|Z_1|^2 + |Z_2|^2\right) Z_{\mu 2} Z^*_{\nu 1} + \left((Z_1^*)^2 + (Z_2^*)^2\right) Z_{\mu 2} Z_{\nu 1} \\ & - (\mu \leftrightarrow \nu) \, ; \end{aligned} \quad \text{(xxxiii)}$$

$$
\begin{aligned}
(\psi_\mu^2\psi_\nu^3 - \psi_\nu^2\psi_\mu^3) = i\Big[& \left((Z_1)^2 - (Z_2)^2\right) Z^*_{\mu 2} Z^*_{\nu 1} + (Z_1 Z_2^* + Z_1^* Z_2) Z_{\mu 1} Z^*_{\nu 1} \\
& + (|Z_1|^2 + |Z_2|^2) Z^*_{\mu 1} Z_{\nu 2} + (|Z_1|^2 + |Z_2|^2) Z^*_{\mu 2} Z_{\nu 1} \\
& + (Z_1^* Z_2 + Z_1 Z_2^*) Z_{\mu 2} Z^*_{\nu 2} + \left((Z_1^*)^2 - (Z_2^*)^2\right) Z_{\mu 1} Z_{\nu 2} \\
& - (\mu \leftrightarrow \nu)\Big] . \qquad \text{(xxxiv)}
\end{aligned}
$$

We start by writing $\mathcal{L}_{\text{gen}(\alpha=1),2}$ in terms of the fields Z:

$$
\begin{aligned}
\mathcal{L}_{\text{gen}(\alpha=1),2} &= \frac{\kappa_2}{2}\text{Tr}[(M_\mu^1)^2 + (M_\mu^2)^2] && (2.78) \\
&= -\frac{\kappa_2}{4}[(Z_1^* Z^*_{\mu 2} - Z_1 Z_{\mu 2} + Z_2 Z_{\mu 1} - Z_2^* Z^*_{\mu 1})^2 \\
&\qquad - (Z_2^* Z^*_{\mu 1} + Z_2 Z_{\mu 1} - Z_1 Z_{\mu 2} - Z_1^* Z^*_{\mu 2})^2] && (2.79) \\
&\qquad \vdots \\
&= -\frac{\kappa_2}{4}[-4|Z_1|^2|Z_{\mu 2}|^2 - 4|Z_2|^2|Z_{\mu 1}|^2 \\
&\qquad + 4Z_1^* Z_2 Z_{\mu 1} Z^*_{\mu 2} + 4Z_1 Z_2^* Z^*_{\mu 1} Z_{\mu 2}] && (2.80) \\
&= \kappa_2 (Z_1 Z_{\mu 2} - Z_2 Z_{\mu 1})(Z_1^* Z^*_{\mu 2} - Z_2^* Z^*_{\mu 1}) , && (2.81)
\end{aligned}
$$

where all we have done in going from eq. (2.79) to (2.80) is to expand the squares and cancel terms.

We now use identities (xxvii), (xxix), and (xxxi) to write down the term in $\mathcal{L}_{\text{SF},2}$:

$$
\begin{aligned}
(\vec{\psi}_\mu)^2 &= (\psi_\mu^1)^2 + (\psi_\mu^2)^2 + (\psi_\mu^3)^2 \\
&= (Z^*_{\mu 1} Z_2 + Z^*_{\mu 2} Z_1 + Z_1^* Z_{\mu 2} + Z_2^* Z_{\mu 1})^2 \\
&\qquad - (Z^*_{\mu 1} Z_2 - Z^*_{\mu 2} Z_1 + Z_1^* Z_{\mu 2} - Z_2^* Z_{\mu 1})^2 \\
&\qquad + (Z^*_{\mu 1} Z_1 - Z^*_{\mu 2} Z_2 + Z_1^* Z_{\mu 1} - Z_2^* Z_{\mu 2})^2 && (2.82) \\
&\qquad\qquad \vdots \\
&= 4(Z_1 Z_{\mu 2} - Z_2 Z_{\mu 1})(Z_1^* Z^*_{\mu 2} - Z_2^* Z^*_{\mu 1}) , && (2.83)
\end{aligned}
$$

where use has been made of identity (xxii) in going from eq. (2.82) to (2.83), in order to cancel certain terms. This leads us to the following conclusion:

$$\mathcal{L}_{\mathrm{gen}(\alpha=1),2} = \frac{\kappa_2}{4}(\vec{\psi}_\mu)^2 = \mathcal{L}_{\mathrm{SF},2}\,. \tag{2.84}$$

The last step is to relate $\mathcal{L}_{\mathrm{SF},4}$ to $\mathcal{L}_{\mathrm{gen}(\alpha=1),4}$. We begin by writing $(G_{\mu\nu})^2$ as follows:

$$\begin{aligned}
(G_{\mu\nu})^2 &= \varepsilon_{abc}\varepsilon_{def}\psi^a\psi^d\psi^b_\mu\psi^e_\mu\psi^c_\nu\psi^f_\nu && (2.85)\\
&= \Big(\delta_{ad}(\delta_{be}\delta_{cf}-\delta_{bf}\delta_{ce}) - \underbrace{\delta_{ae}}_{\psi^a\psi^a_\mu=0}(\delta_{bd}\delta_{cf}-\delta_{bf}\delta_{cd})\\
&\qquad + \underbrace{\delta_{af}}_{\psi^a\psi^a_\nu=0}(\delta_{bd}\delta_{ce}-\delta_{be}\delta_{cd})\Big)\times\psi^a\psi^d\psi^b_\mu\psi^e_\mu\psi^c_\nu\psi^f_\nu && (2.86)\\
&= (\vec{\psi}_\mu)^2(\vec{\psi}_\nu)^2 - \Big(\vec{\psi}_\mu\cdot\vec{\psi}_\nu\Big)^2 && (2.87)\\
&= (\psi^1_\mu\psi^2_\nu-\psi^1_\nu\psi^2_\mu)^2+(\psi^1_\mu\psi^3_\nu-\psi^1_\nu\psi^3_\mu)^2+(\psi^2_\mu\psi^3_\nu-\psi^2_\nu\psi^3_\mu)^2 && (2.88)\\
&= -4(Z^\dagger_\mu Z_\nu - Z^\dagger_\nu Z_\mu)^2\,, && (2.89)
\end{aligned}$$

where, in going from eq. (2.88) to (2.89), we have made use of the identities (xxxii), (xxxiii), and (xxxiv) and, unless one has the stamina, a decent symbolic manipulation software can be used to get to eq. (2.89), using identities (xxi) and (xxii) as assumptions.

To make the connection with $\mathcal{L}_{\mathrm{gen}(\alpha=1),4}$, we use (vi) to express the Z fields in terms of the ϕ fields:

$$(Z^\dagger_\mu Z_\nu - Z^\dagger_\nu Z_\mu)^2 = -4[(\phi^1_\mu\phi^2_\nu-\phi^1_\nu\phi^2_\mu)+(\phi^0_\mu\phi^3_\nu-\phi^0_\nu\phi^3_\mu)]^2\,. \tag{2.90}$$

Therefore,

$$\frac{1}{16}(G_{\mu\nu})^2 = [(\phi^1_\mu\phi^2_\nu-\phi^1_\nu\phi^2_\mu)+(\phi^0_\mu\phi^3_\nu-\phi^0_\nu\phi^3_\mu)]^2\,. \tag{2.91}$$

Finally, if we think of $K^3_{\mu\nu}$ as a matrix with entries (μ, ν) then, from eqs. (2.69) and (xviii), we have:

$$(K^3_{\mu\nu})^2 = 4\varepsilon_{3ab}\varepsilon_{3cd}m^a_\mu m^b_\nu m^c_\mu m^d_\nu \tag{2.92}$$

$$\vdots$$

$$= 4[(\phi^1_\mu\phi^2_\nu - \phi^1_\nu\phi^2_\mu) + (\phi^0_\mu\phi^3_\nu - \phi^0_\nu\phi^3_\mu)]^2 \,. \tag{2.93}$$

We can now relate $G_{\mu\nu}$ with $K^3_{\mu\nu}$ as follows:

$$\frac{1}{16}(G_{\mu\nu})^2 = \frac{1}{4}(K^3_{\mu\nu})^2 \,, \tag{2.94}$$

$$\frac{1}{32}(G_{\mu\nu})^2 = \frac{1}{8}(K^3_{\mu\nu})^2 \,, \tag{2.95}$$

which leads us to the following conclusion:

$$\mathcal{L}_{\mathrm{gen}(\alpha=1),4} = \frac{\kappa_4}{8}(K^3_{\mu\nu})^2 = \frac{\kappa_4}{32}(G_{\mu\nu})^2 = \mathcal{L}_{\mathrm{SF},4} \,, \tag{2.96}$$

which brings us to the end of our calculation.

2.5 The Skyrme crystal

It turns out that there is a special way of arranging skyrmions in order to obtain the smallest known value of the energy per baryon number seen so far [10], known as the Skyrme crystal. This is an infinite, triply-periodic, arrangement of half-skyrmions [42–47]. In order to study Skyrme crystals, we impose periodic boundary conditions on the Skyrme field in all three directions, with periods $(L_x, L_y, L_z) \equiv (L_1, L_2, L_3)$ along the $(x, y, z) \equiv (x^1, x^2, x^3) \equiv (x_1, x_2, x_3)$ directions, respectively. The skyrmions are therefore defined on a 3-torus T^3.

Skyrme crystals were originally proposed by Klebanov [42] as a model for dense nuclear matter, such as that found in neutron stars. At the time,

the behaviour of two well-separated skyrmions was already known [9] – an important feature being that these are maximally-attracted when one is rotated with respect to the other by 180° about a line perpendicular to the line connecting them. Klebanov believed that an interesting extension of this idea would be to have an array of skyrmions, where any skyrmion would be attracted by its nearest neighbours. A graceful way of achieving this, Klebanov showed, would be to arrange the skyrmions in a simple-cubic lattice with appropriate rotations applied to all the nearest neighbours of a chosen skyrmion [42]. Moreover, if the skyrme fields are to have the correct periodicity in all three directions, they must have symmetry elements that combine both spatial transformations as well as isospin transformations acting on the individual fields (more on this shortly).

Klebanov also showed that there is a minimum in the energy for a certain value of the period $L \equiv L_x = L_y = L_z$, which in our units was first shown in [46] to be $L = 4.7$. In other words, there is a preferred size of the fundamental cell. Later, Goldhaber and Manton showed [43] that there is a phase transition from a low-density simple-cubic lattice of skyrmions to a high-density body-centred lattice of half-skyrmions. However, it has since been shown by Kugler and Shtrikman [46, 47] and by Castillejo et al. [45] that the lowest energy per baryon configuration is that of a (high-density) half-skyrmion phase corresponding to an initial (low-density) face-centred cubic (fcc) array of skyrmions.

An fcc array is one in which skyrmions with standard orientation are placed on the vertices of a cube and more skyrmions are placed on the face centres, but this time rotated by 180° about an axis perpendicular to the face. Such a configuration produces 12 nearest neighbours (to a particular skyrmion), which are all in the attractive channel. If the origin is fixed at the centre of one of the unrotated skyrmions and the skyrme fields are given by $\Phi_\beta(\mathbf{x}) = (\Phi_1(\mathbf{x}), \Phi_2(\mathbf{x}), \Phi_3(\mathbf{x}), \Phi_4(\mathbf{x}))$, then the fcc configuration would have spatial

and isospin symmetries, as was alluded to above. The generators for these symmetries are listed in Table 2.1 [10]:

Table 2.1: Symmetry generators of an fcc array of skyrmions

Transformation Name	Spatial Transformation	Isospin Transformation
$\mathcal{R}_1$	$(x_1, x_2, x_3) \to (-x_1, x_2, x_3)$	$(\Phi_1, \Phi_2, \Phi_3, \Phi_4) \to (-\Phi_1, \Phi_2, \Phi_3, \Phi_4)$
$\mathcal{R}^3_{1,-}$	$(x_1, x_2, x_3) \to (x_2, x_3, x_1)$	$(\Phi_1, \Phi_2, \Phi_3, \Phi_4) \to (\Phi_2, \Phi_3, \Phi_1, \Phi_4)$
$\mathcal{R}^4_{1,-}$	$(x_1, x_2, x_3) \to (x_1, x_3, -x_2)$	$(\Phi_1, \Phi_2, \Phi_3, \Phi_4) \to (\Phi_1, \Phi_3, -\Phi_2, \Phi_4)$
$\mathcal{T}_{1+,2+}$	$(x_1, x_2, x_3) \to (x_1 + L/2, x_2 + L/2, x_3)$	$(\Phi_1, \Phi_2, \Phi_3, \Phi_4) \to (-\Phi_1, -\Phi_2, \Phi_3, \Phi_4)$

The transformations listed here are $\mathcal{R}_1$: a reflection in the x_1-axis, $\mathcal{R}^3_{1,-}$: a "negative" three-fold rotation about the diagonal that goes from the origin to the opposite corner of the cube (defined as "1"), $\mathcal{R}^4_{1,-}$: a "negative" four-fold rotation about the x_1-axis, and $\mathcal{T}_{1+,2+}$: a positive $L/2-$translation in both the x_1-axis and the x_2-axis. Note that these are a subset of the possible transformations that can be carried out on an fcc lattice. For example, one can also have a "positive" three-fold rotation along the same diagonal, $\mathcal{R}^3_{1,+}$, given by the transformation: $(x_1, x_2, x_3) \to (x_3, x_1, x_2)$, $(\Phi_1, \Phi_2, \Phi_3, \Phi_4) \to (\Phi_3, \Phi_1, \Phi_2, \Phi_4)$. Another possible transformation could also be a "positive" four-fold rotation about the x_3-axis, $\mathcal{R}^4_{3,+}$: $(x_1, x_2, x_3) \to (-x_2, x_1, x_3)$, $(\Phi_1, \Phi_2, \Phi_3, \Phi_4) \to (-\Phi_2, \Phi_1, \Phi_3, \Phi_4)$.

There is an additional symmetry unique to the high-density phase of half-skyrmions. Its generator is given by:

Table 2.2: Additional symmetry generator of the high-density half-skyrmion phase

Transformation Name	Spatial Transformation	Isospin Transformation
$\mathcal{T}_{1+}$	$(x_1, x_2, x_3) \to (x_1 + L/2, x_2, x_3)$	$(\Phi_1, \Phi_2, \Phi_3, \Phi_4) \to (-\Phi_1, \Phi_2, \Phi_3, -\Phi_4)$

Note that this transformation involves a chiral SO(4), rather than just isospin SO(3) rotations displayed in Table 2.1 above and it can replace the $\mathcal{T}_{1+,2+}$ transformation since that can be achieved through successive applications of $\mathcal{T}_{1+}$ and $\mathcal{T}_{2+}$.

An analytic approximation for the fields of the Skyrme crystal was proposed in [45]. It takes into account the SO(4) chiral symmetry as well as the SO(3) isospin symmetries. The fields are expressed as follows:

$$\Phi_4 = c_1 c_2 c_3 \,, \tag{2.97}$$

$$\Phi_1 = -s_1 \left(1 - \frac{s_2^2}{2} - \frac{s_3^2}{2} + \frac{s_2^2 s_3^2}{3}\right)^{\frac{1}{2}} \text{ and cyclic permutations,} \tag{2.98}$$

where $s_i = \sin(2\pi x^i/L)$ and $c_i = \cos(2\pi x^i/L)$. It is a good approximation to the actual minimal-energy solution.

We will see that the field behaves in an interesting way as one changes the period of the crystal in different ways, for different directions. For example, if we start with the Skyrme crystal and then increase the period along all three space dimensions in the same way, one gets the familiar picture of the cubically-symmetric charge $Q = 4$ skyrmion. We also show that the energy density of the Skyrme crystal displays certain similarities previously seen in the context of Skyrme chains, provided we have large $L_{x,y}$ (where $L_x = L_y$) and small L_z values. Skyrme chains are solutions of the Skyrme model, which are periodic in one space dimension. It has been shown [8] that soliton chains generally have constituents in the form of vortex-antivortex pairs. These emerge when the period is small compared to the natural soliton size - a feature that we verify when the period in the $z-$direction is small compared to the other two space directions. When the period increases, the constituents tend to clump together, a feature that is also verified here.

A double Skyrme sheet [2], is also seen to emerge at small $L_{x,y}$ and large L_z values. It takes the form of a square lattice, an object analogous to the hexagonal "Skyrme domain wall" solution [7]. However, our system is periodic in all three directions, which means that the vacuum value on both sides of the Skyrme sheets ($\pm\infty$ in the $z-$direction) is unique.

Finally, we describe what happens as one increases the period simultaneously

in all three directions, starting with the Skyrme crystal, and show that there is a rapid transition between the Skyrme crystal and the $Q = 4$ skyrmion with cubic symmetry. We show evidence which suggests that this is a second-order phase transition with an order parameter given by the period $L_{x,y,z}$ of the configuration (where $L_x = L_y = L_z$).

Part II

Skyrme Lattices

Chapter 3

Skyrme crystal deformations

In sec. 2.5 we mentioned that the Skyrme crystal has been shown to have an energy minimum for the period $L = 4.7$, which we call the "optimal period". Our goal in this chapter is to see what other structures emerge, aside from the cubic lattice of eight approximately spherically-symmetric half-skyrmions, when we move away from this optimal period in all three directions.

In what follows, we take periodic boundary conditions in all three space directions - the periods will be specified in the relevant sections. The lattice spacings in the x, y, and z directions are given by h_x, h_y, h_z and the number of lattice points are given by n_x, n_y, n_z, yielding side-lengths $L_{x,y,z} = h_{x,y,z} * n_{x,y,z}$. We use a first-order finite-difference scheme and implement a full 3-dimensional numerical minimization of the energy using the conjugate gradient method (see e.g. [48]).

Note that there is a numerical error associated with the finite lattice spacing. The way we approximate the errors in the energy, for a given configuration, is by comparing its topological charge (using numerical methods) with the "true" value of its charge ($Q = 4$). We assume the same errors in energy and charge since similar finite-difference methods are employed in calculating each of these values. As one would expect, larger lattice spacing gives larger truncation error.

The initial condition that we start with for minimization is the approximate Skyrme crystal of eight half-skyrmions, namely (2.97) and (2.98). After being minimized, the period in each direction for this initial configuration is then changed in a certain way (described in the relevant section) and then re-minimized.

3.1 From a 4-skyrmion to a square 2-wall

The first case is the one for which the period in all three directions is large for the initial configuration and then the $L_{x,y}$ periods are reduced gradually. The initial period is given by $L_{x,y,z} = 7.05$ (see Fig. 3.1) and then reduce $L_x = L_y$ by 1 each time. As this is the first figure, we take the opportunity to mention that, for all figures featuring energy density isosurfaces, each subfigure shows a zoomed in version of the relevant isosurface and, therefore, the vertical and horizontal scales change; this is done in order to make it easy for the reader's tired eyes to be able to discern all the features described in the text.

We start by increasing the periods $L_x = L_y = L_z$ for the minimized Skyrme crystal from $L_{x,y,z} = 4.7$ to 7.05 by increasing the value of $n_{x,y,z}$, for a certain value of $h_{x,y,z}$, and thus producing Fig. 3.1 (a). Afterwards, $n_{x,y,z}$ is kept constant and $L_{x,y,z}$ is reduced by 1 each time.

One can see that the translation symmetries, $\mathcal{T}_{i+/-}$, (where $i = \{1, 2, 3\}$ and in either direction $+/-$) of the high-density Skyrme crystal are broken in Fig. 3.1 (a), which is the $Q = 4$ skyrmion, whereas all reflection symmetries, $\mathcal{R}_i$, three-fold rotations $\mathcal{R}^3_{1/2,+/-}$, and four-fold rotations $\mathcal{R}^4_{i,+/-}$ remain unbroken – characteristic of cubic symmetry. In Fig. 3.1 (b)-(f), $\mathcal{T}_{1+/-}$ and $\mathcal{T}_{2+/-}$ symmetries are regained (possibly due to the fact that we are "squeezing" the configuration in these directions), whereas $\mathcal{T}_{3+/-}$ remains broken only for Fig. 3.1 (b) and Fig. 3.1 (c), due to the fact that these figures are not extended throughout the whole period in the $z-$direction. The reflec-

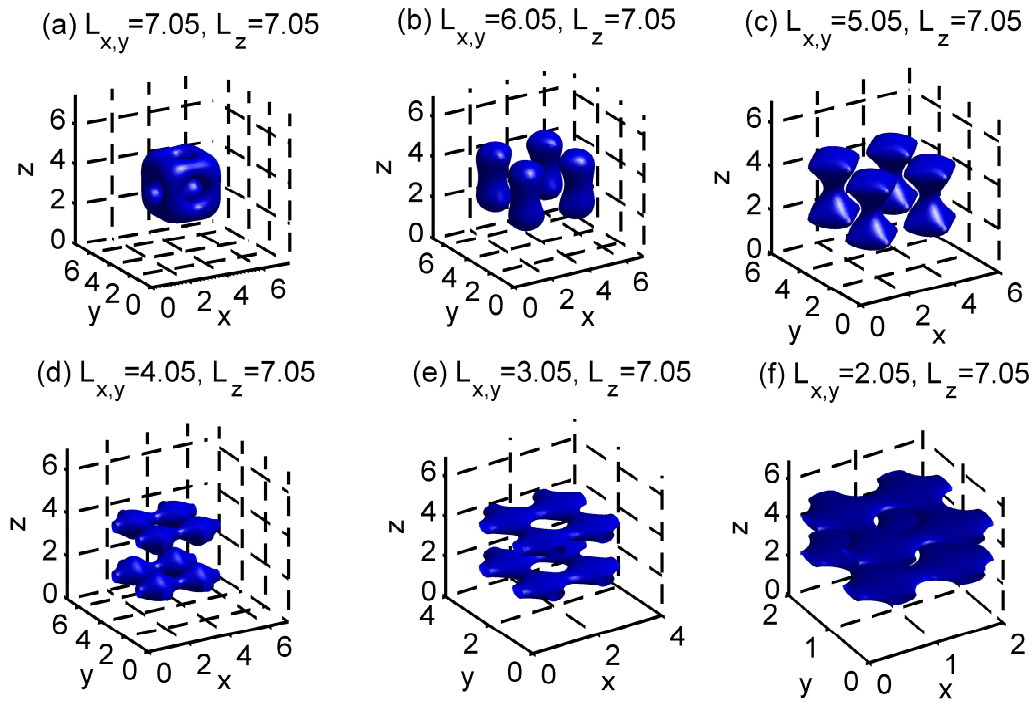

Figure 3.1: Energy density isosurfaces with surface value given by $0.5 * \mathcal{E}_{\max}$, where $\mathcal{E}_{\max}$ is the maximum value of the energy density (all isosurfaces in this chapter have the same surface value). The first isosurface corresponds to the $Q = 4$ skyrmion for the periods $L_{x,y,z} = 7.05$. Each successive picture has $L_{x,y}$ reduced by 1 and L_z is kept constant at 7.05.

tion symmetries $\mathcal{R}_i$ are unbroken and the three-fold rotations $\mathcal{R}^3_{1/2,+/-}$ are broken in Figs. 3.1 (b)-(f). The four-fold rotations $\mathcal{R}^4_{3,+/-}$ remain unbroken throughout, whereas $\mathcal{R}^4_{1/2,+/-}$ are broken in Figs. 3.1 (b)-(f).

Note that a double Skyrme sheet configuration [2] emerges in Fig. 3.1 (d). The separation between the sheets, which is calculated by measuring the distance between the energy density peaks as a function of z, remains constant as $L_{x,y}$ is reduced further and L_z is kept constant at $L_z = 7.05$. However, the energy decreases from a value of $E = 4.36 \pm 0.09$ at $L_{x,y,z} = 7.05$ down to a minimum of $E = 4.20 \pm 0.05$ at $L_{x,y} = 4.05$ and, finally, increases to $E = 5.25 \pm 0.10$ at $L_{x,y} = 2.05$.

The preferred configuration for this Skyrme sheet is to have $L_x = L_y$. For instance, if we fix $L_y = 4.05$ and vary L_x away from this value in either direction, we notice that the energy increases.

3.2 From square 2-walls to vortices

We now start with a large L_z period, which will be reduced, and keep $L_{x,y} = 4$ constant. The starting point is $L_z = 7$, which is then reduced by 1 each time. In this section, $n_x = n_y = n_z$ are kept constant, producing different h_z values each time L_z is changed.

The initial condition (eqs. (2.97) and (2.98)) is first minimized for the periods $L_{x,y} = 4$ and $L_z = 7$, producing the double Skyrme sheet configuration seen in Fig. 3.2 (a). The only broken symmetries associated with this configuration, which are seen to persist in Fig. 3.2 (b) and Fig. 3.2 (c), are $\mathcal{R}^4_{1/2,+/-}$ and $\mathcal{R}^3_{1/2,+/-}$. These are regained in Fig. 3.2 (d), which is a (non-minimal) Skyrme crystal configuration. As the L_z period is decreased further, we notice the appearance of vortex-like structures, which are periodic in the $z-$direction (Fig. 3.2 (e) and Fig. 3.2 (f)). The symmetries associated with these configurations are the same as those in Figs. 3.2 (a)-(c) and, in fact,

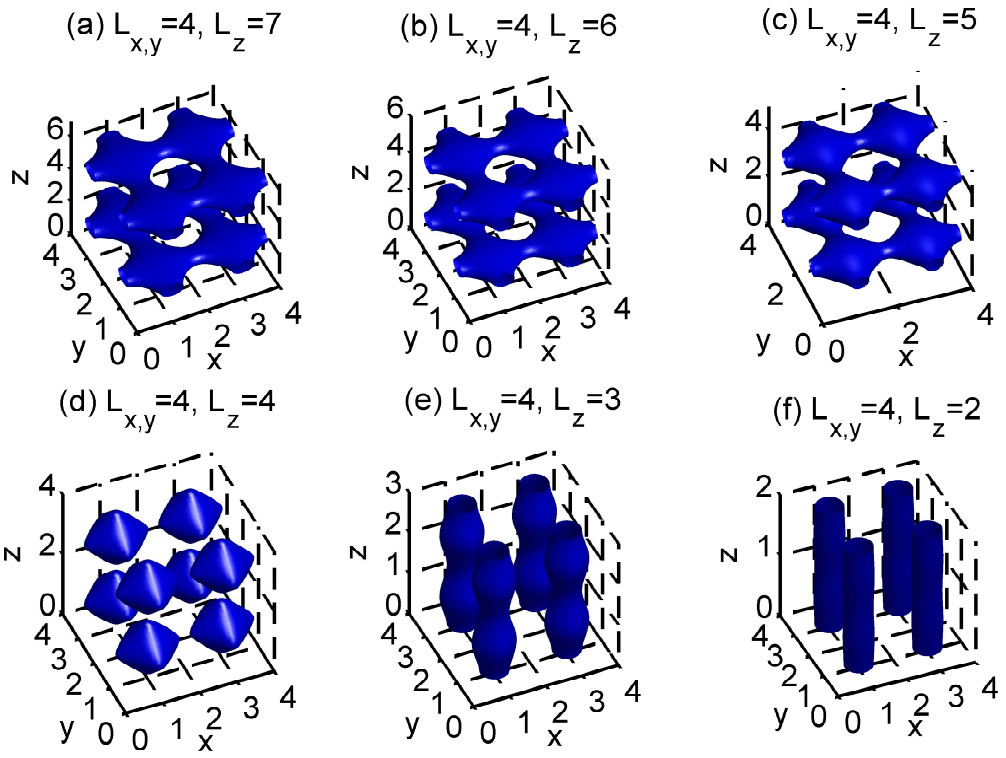

Figure 3.2: Energy density isosurfaces corresponding to the $Q = 4$ double Skyrme sheet configuration, where $L_{x,y} = 4$ remains fixed and where $L_z = 7$ is reduced by 1 in each successive picture, transforming the double skyrme sheet into a (non-minimal) Skyrme crystal and thereafter into a parallel 4-vortex structure.

the translation symmetry in the $z-$direction, $\mathcal{T}_{3+/-}$, becomes continuous for Fig. 3.2 (f), since there is no longer any noticeable $z-$dependence. This ties into the subject of Skyrme chains, which has been explored in [8].

The energy of the isosurfaces decreases from a value of $E = 4.22 \pm 0.05$ at $L_z = 7$, down to a minimum of $E = 4.17 \pm 0.04$ at $L_z = 5$ (where the isosurfaces are still in the form of a double square wall), then back up to $E = 4.89 \pm 0.05$ at $L_z = 2$.

3.3 From square 2-walls to vortices, via crystal

In this section, we show how one can transform a double Skyrme sheet configuration into the 4-vortex configuration discussed in the previous section, by changing both $L_x = L_y$ and L_z (rather than just L_z), and going through an intermediate, minimal, Skyrme crystal state, as can be seen in Fig. 3.3. The initial period is $L_{x,y} = 2.7$ and $L_z = 10.7$. The former is then increased by 1 and the latter decreased by 3, two consecutive times, producing Figs. 3.3 (b)-(c). The changes in the periods are then swapped, increasing $L_{x,y}$ by 3 and decreasing L_z by 1, for two consecutive times, producing Figs. 3.3 (d)-(e). Here, $n_x = n_y = n_z$ are kept constant, producing different $h_x = h_y$ and h_z values, each time the periods are changed.

We start by minimizing the approximate Skyrme crystal (eqs. (2.97) and (2.98)) for the periods $L_{x,y} = 2.7$ and $L_z = 10.7$, producing the double Skyrme sheets discussed in the previous sections (with the same symmetries) in Fig. 3.3 (a). As the periods are changed, as described above, the Skyrme sheets still persist in Fig. 3.3 (b), and change into the (minimal-energy) Skyrme crystal in Fig. 3.3 (c) (with all its associated symmetries as described in the introduction). As $L_{x,y}$ increase and L_z decreases further, the Skyrme crystal changes into a 4-vortex structure, Figs. 3.3 (d)-(e), which have less of a $z-$dependence than the ones in Figs. 3.2 (e)-(f), respectively.

The Skyrme crystal has the minimum energy, with $E = 4.13 \pm 0.04$, followed by the square 2-walls at $L_{x,y} = 3.7$ and $L_z = 7.7$ with $E = 4.26 \pm 0.06$. The final picture, the 4-vortex configuration with the smallest L_z-value, has the highest energy with $E = 4.77 \pm 0.17$, which follows from the fact that (due to the nature of this system) $E \to \infty$ when any combination of the periods $(L_x, L_y, L_z) \to 0$.

Thus far, we have changed the periods in the three space directions in different ways – by decreasing $L_{x,y}$ (or keeping it constant) and keeping L_z

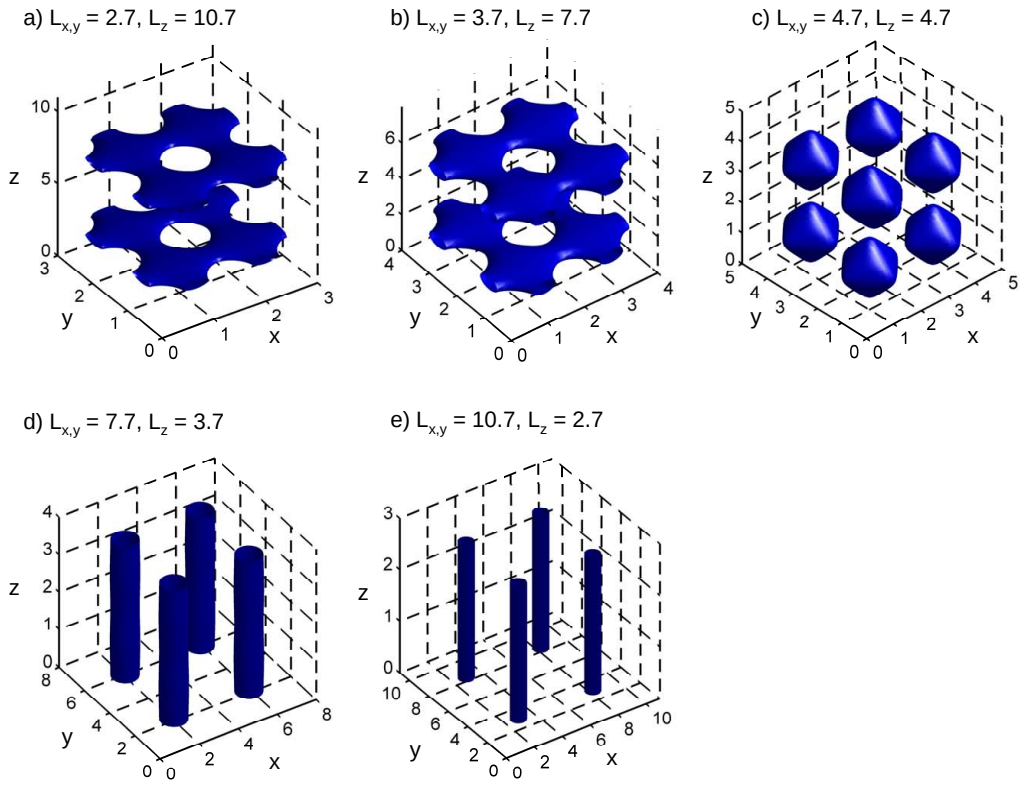

Figure 3.3: Energy density isosurfaces, which show a transition from a pair of Skyrme sheets to a 4-vortex configuration. Subsequent pictures have $L_{x,y}$ and L_z changing in such a way that their values are swapped halfway through the transition.

constant (or decreasing it) or changing all three periods at different rates at the same time. We now turn to the case where we increase (or decrease) all three periods simultaneously at the same rate.

3.4 From the Skyrme crystal to the Q=4 skyrmion

It turns out that an interesting feature of the $Q = 4$ system is uncovered when one starts from the minimal-energy Skyrme crystal configuration at $L_{x,y,z} = 4.7$ and then increases the periods simultaneously until the individual half-skyrmions coalesce.

These half-skyrmions clump in a sudden fashion when one perturbs the system in a certain way. We perturbed it by removing one lattice site through the middle of the configuration in all three directions, thereby "squeezing" the half-skyrmions together in all directions. Therefore, in order to see them coalescing, one needs to increase the periods very gradually. This appears to happen in the range $L_{x,y,z} = 6.07 - 6.09$ as can be seen in Fig. 3.4, where the first picture has periods $L_{x,y,z} = 4.7$ and the following three correspond to the range just mentioned. Compare this with Fig. 3.5, where the periods are increased in larger steps.

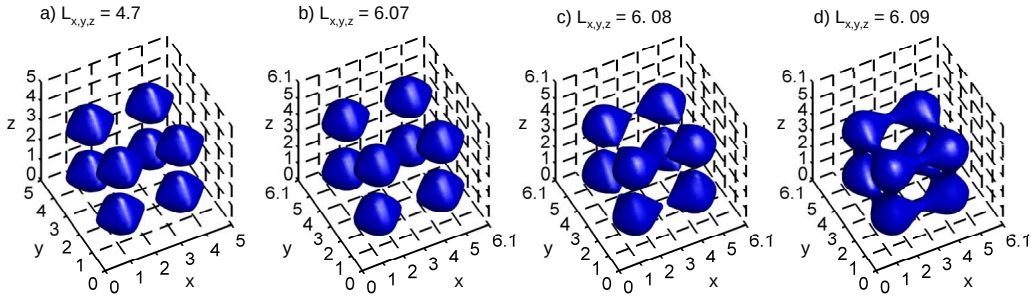

Figure 3.4: The energy density isosurface of the $Q = 4$ Skyrme crystal at $L_{x,y,z} = 4.7$. The periods are then increased gradually from $L_{x,y,z} = 6.07$ to $L_{x,y,z} = 6.09$.

The sudden merging of the half-skyrmions can be visualized in a different fashion by taking the maximum value of the difference in the energy densi-

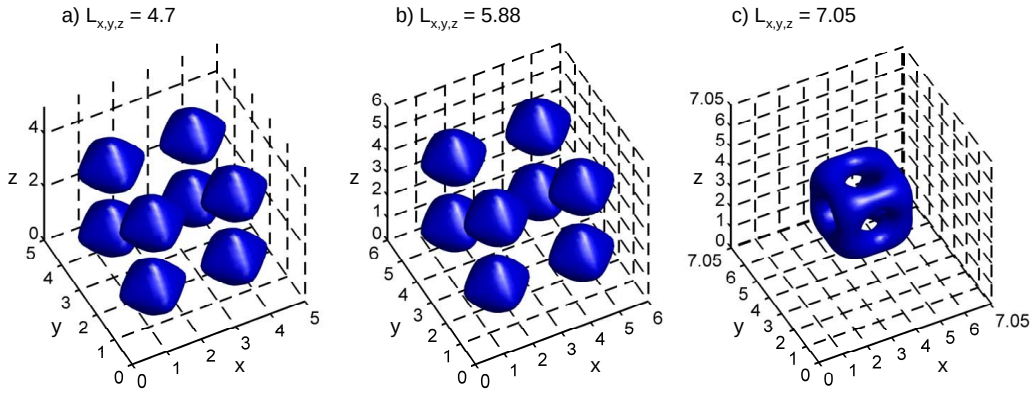

Figure 3.5: Fig. a) corresponds to the energy density isosurface of the Skyrme crystal for the periods $L_{x,y,z} = 4.7$, Fig. b) has $L_{x,y,z} = 5.88$, and Fig. c) has $L_{x,y,z} = 7.05$

ties of the fields $\mathcal{E}[\Phi_\beta(x^j)]$ under a certain symmetry transformation, in this case a translation of $L_x/2$ in the $x-$direction, which is half the size of the fundamental cell, and dividing by the maximum value of the energy density, i.e. $\Delta_1 = (\mathcal{E}[\Phi_\beta(x^j)] - \mathcal{E}[\Phi_\beta(x^{j'})])_{\max}/\mathcal{E}_{\max}$, where $x^{j'} = x^j - L_x/2$. We then plot this as a function of the period $L_{x,y,z}$ - the reason we do this is that, as soon as the half-skyrmions start to coalesce, they will no longer be $L_x/2-$periodic. For the Skyrme crystal, this difference is seen to be essentially zero and it then starts to increase as the half-skyrmions begin to coalesce as can be seen in Fig. 3.6.

This jump in the asymmetries of the crystal is analogous to a phase transition in thermodynamics. There is a sudden transition from a crystalline phase, which has more symmetries, such as chiral SO(4) symmetries for the Skyrme crystal, to a phase with less symmetries, such as SO(3) isospin symmetries for the $Q = 4$ cubic-shaped skyrmion. We expect the transition to become more pronounced as the number of lattice points increases – as can be seen in Fig. 3.6, when $n_{x,y,z}$ is increased from 32 to 36, which starts to resemble a step function. It should be noted that the Δ_1 values are independent of which $L_{x,y,z}$ value one starts with, which hints to a lack of hysteresis in the system. Extending the analogy with phase transitions, this lack of hysteresis

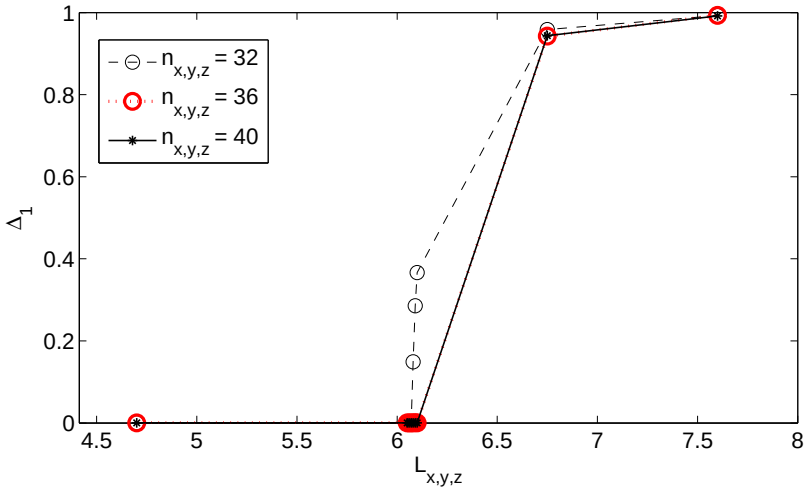

Figure 3.6: Difference in the value of the energy density of the Skyrme fields under an $L_x/2-$translation in the $x-$direction divided by $\mathcal{E}_{\max}$, for different values of the period $L_{x,y,z}$. Note that as the number of lattice points $n_{x,y,z}$ increases, the half-skyrmions coalesce more abruptly.

strongly suggests a second-order phase transition (see e.g. [49]), with no latent heat, and with the period $L_{x,y,z}$ as the order parameter.

To sum up, we have seen that by changing the periods of the Skyrme crystal, one obtains qualitatively different energy density configurations, including what appear to be vortex-like structures with little or no $z-$dependence, when L_z is small compared with $L_{x,y}$, and square lattices when $L_{x,y}$ is small compared with L_z. Finally, by way of making contact with results obtained by others, we should point out that there has recently been a conjecture by Prof. Nick Manton[1], which states that hexagonal lattices akin to graphene (see e.g. [7] and Ch. 4) may emerge if one performs a stretch along a diagonal of the Skyrme crystal, since a hexagonal symmetry is evident, should one look along one of its diagonals.

[1]We have learned this through informal discussions.

Chapter 4

Square and hexagonal lattices

In this chapter, we present some material which is largely self-contained, even though it was inspired by some of the results of Chapter 3. Recall from that chapter that a $Q = 4$ skyrmion and a Skyrme crystal can be transformed into a pair of square sheets by lowering their $L_{x,y}$ periods (see sec. 3.1, Fig. 3.1 and sec. 3.3, Fig. 3.3). We now wish to investigate some properties of these square sheets, such as their energy and stability, and compare them to hexagonal sheets. In sec. 4.1, we present an ansatz we shall be using as an initial condition for such sheets in the Skyrme model. In sec. 4.2, we discuss the techniques used in obtaining their optimal periods. Finally, in sec. 4.3, we investigate the case where the number of sheets $N > 2$ and briefly discuss their stability.

4.1 Ansatz

In this section, we shall be dealing with complex functions $W(z)$. Therefore, to avoid confusion, we denote the three spatial directions (x_1, x_2, x_3) (as in sec. 2.5) and the complex coordinate $z \equiv x_1 + ix_2$. We can express the Skyrme fields Φ_β (where $\beta = \{1, 2, 3, 4\}$) in terms of complex functions $W(z) \equiv W$

through the use of a unit vector $\hat{\mathbf{n}}_W$, given by [7]:

$$\begin{aligned}\hat{\mathbf{n}}_W &\equiv \frac{1}{1+|W|^2}((W+W^*), i(W^*-W), 1-|W|^2) \\ &= \frac{1}{1+|W|^2}(2\mathrm{Re}(W), 2\mathrm{Im}(W), 1-|W|^2)\,. \end{aligned} \tag{4.1}$$

The fields Φ_β can be encapsulated in a 2×2 matrix U, written in terms of the unit vector $\hat{\mathbf{n}}_W$ and Pauli matrices $\boldsymbol{\sigma} \equiv \{\sigma_1, \sigma_2, \sigma_3\}$ (defined in (i), sec. 2.4.2), as follows:

$$U(x_1, x_2, x_3) = \exp(if(x_3)\hat{\mathbf{n}}_W \cdot \boldsymbol{\sigma}) \tag{4.2}$$

$$\begin{aligned} &= \cos(f(x_3)) \cdot \mathbb{1} + i\sin(f(x_3)) \\ &\quad \times \left[\left(\frac{2\mathrm{Re}(W)}{1+|W|^2}\right)\sigma_1 + \left(\frac{2\mathrm{Im}(W)}{1+|W|^2}\right)\sigma_2 + \left(\frac{1-|W|^2}{1+|W|^2}\right)\sigma_3\right], \end{aligned} \tag{4.3}$$

where $f(x_3) \equiv 2N\mathrm{arctan}\{\exp(2[x_3 - L_3/2])\}$ and N is equal to the number of sheets. Note that near the limits $x_3 = (0, L_3)$, the function f is approximately $f(x_3) \approx (0, N\pi)$. Using the definition of U (see (vi), sec. 2.4.2), we can now write the fields as:

$$\Phi_1 = \sin(f(x_3))\left(\frac{2\mathrm{Re}(W)}{1+|W|^2}\right), \tag{4.4}$$

$$\Phi_2 = \sin(f(x_3))\left(\frac{2\mathrm{Im}(W)}{1+|W|^2}\right), \tag{4.5}$$

$$\Phi_3 = \sin(f(x_3))\left(\frac{1-|W|^2}{1+|W|^2}\right), \tag{4.6}$$

$$\Phi_4 = \cos(f(x_3))\,. \tag{4.7}$$

Recall that a skyrmion centred at the origin has the boundary conditions $\Phi_4(x_i) \to 1$ as $|x_i| \to \infty$ and $\Phi_4(x_i) \to -1$ as $|x_i| \to 0$ (see sec. 2.1). A skyrmion can therefore be thought of as a surface which divides space into two regions with different vacuum values: $\Phi_4 = \pm 1$. Since Skyrme sheets

are extended objects, which stretch out over the (periodic) (x_1, x_2)-plane, we choose to define it as the surface which divides space in the x_3-direction into regions where the field Φ_4 takes these different vacuum values. If one looks closely at the expression for Φ_4, eq. (4.7), one can see that it indeed divides the lattice in the x_3-direction, where $x_3 \in [0, L_3]$, into regions where the field Φ_4 takes the values $\{+1, 0, -1\}$; the location of the sheets is defined to be those values of x_3 where $\Phi_4 = 0$. For example, in going from $x_3 = 0$ to $x_3 = L_3$, for $N = 2$, the field would take the values $\Phi_4 = \{+1, 0, -1, 0, +1\}$.

In order to write down the ansatz for the square and hexagonal sheets explicitly, all that is left for us to do is to identify the complex functions $W(z)$. It turns out that the functions which capture the properties of such lattices most gracefully are the Weierstrass p-functions, denoted $\wp(z)$. These are doubly-periodic functions, with complex fundamental periods (ω_1, ω_2), and therefore $\wp(z) = \wp(z + a\omega_1 + b\omega_2)$, where a and b are integers. Due to their periodicity, it suffices to study such functions in a fundamental period parallelogram, which is defined on the complex plane and has vertices: $(0, \omega_1, \omega_2, \omega_1 + \omega_2)$. We shall now define the Weierstrass function and list some identities and results which are relevant to our discussion of square and hexagonal lattices – all of these can be found in [50].

The Weierstrass functions can be expressed as a Laurent series as follows:

$$\wp(z) = z^{-2} + \sum_{k=2}^{\infty} c_k z^{2k-2} \,, \tag{4.8}$$

where

$$c_2 = \frac{g_2}{20} \,, c_3 = \frac{g_3}{28} \,, c_k = \frac{3}{(2k+1)(k-3)} \sum_{m=2}^{k-2} c_m c_{k-m} \,, k \geq 4 \,. \tag{4.9}$$

We shall explain the significance of g_2 and g_3 shortly. The Weierstrass func-

tions satisfy the following differential equation:

$$(\wp'(z))^2 = 4\wp^3(z) - g_2\wp(z) - g_3\,. \tag{4.10}$$

The numbers g_2 and g_3 are called the "invariants" and are related to the geometry of the lattice under consideration. One can also relate the values of $\wp(z)$ at half-periods, denoted by (e_1, e_2, e_3) [i.e. $\wp(\omega_1/2) \equiv e_1, \wp((\omega_1 + \omega_2)/2) \equiv e_2, \wp(\omega_2/2) \equiv e_3$], to the invariants as follows:

$$e_1 + e_2 + e_3 = 0\,, \tag{4.11}$$

$$e_1e_2 + e_2e_3 + e_3e_1 = -\frac{g_2}{4}\,, \tag{4.12}$$

$$e_1e_2e_3 = \frac{g_3}{4}\,. \tag{4.13}$$

It is worth mentioning that the derivative of the Weierstrass function vanishes at the half-period locations, i.e. $\wp'(\omega_1/2) = \wp'((\omega_1 + \omega_2)/2) = \wp'(\omega_2/2) = 0$. With this in mind, and using the Fundamental Theorem of Algebra, one can write down eq. (4.10) as follows:

$$(\wp'(z))^2 = 4(\wp(z) - e_1)(\wp(z) - e_2)(\wp(z) - e_3)\,. \tag{4.14}$$

The identities (4.11)-(4.13) are then obtained by equating like terms in eqs. (4.10) and (4.14).

The invariants can be calculated, among other ways, using Jacobi's theta functions (see e.g. [50–52]). The theta functions, in turn, can be readily calculated in most computer algebra systems and are denoted by $\theta_\beta(z, q)$, where the nome $q = \exp(i\pi\tau)$ and the half-period ratio $\tau \equiv \omega_2'/\omega_1'$ is given in terms of the half-periods $\omega_{1,2}' \equiv \omega_{1,2}/2$. In terms of the theta functions, the

invariants are given by:

$$g_2 = \frac{\pi^4}{12{\omega'_1}^4}(\theta_2(0,q)^8 - \theta_2(0,q)^4\theta_3(0,q)^4 + \theta_3(0,q)^8)\,, \tag{4.15}$$

$$g_3 = \frac{\pi^6}{432{\omega'_1}^6}(2(\theta_2(0,q)^{12} + \theta_3(0,q)^{12}) - 3(\theta_2(0,q)^4\theta_3(0,q)^8 + \theta_2(0,q)^8\theta_3(0,q)^4))\,. \tag{4.16}$$

One can calculate the periods (ω_1, ω_2) through the use of elliptic integrals. The complete elliptic integrals of the 1st kind with parameter m, denoted $K(m)$ and $K'(m) = K(m_1) \equiv K(1-m)$ are defined as follows:

$$K(m) = \int_0^{\pi/2} \frac{d\theta}{\sqrt{1 - m\sin^2(\theta)}}\,. \tag{4.17}$$

These elliptic integrals can, in turn, be expressed in terms of hypergeometric functions $F(a,b;c;z)$, which have the following infinite series representation:

$$F(a,b;c;z) = \frac{\Gamma(c)}{\Gamma(a)\Gamma(b)} \sum_{n=0}^{\infty} \frac{\Gamma(a+n)\Gamma(b+n)}{\Gamma(c+n)} \frac{z^n}{n!}\,. \tag{4.18}$$

We can now write down the elliptic integrals as follows:

$$K(m) = \frac{\pi}{2} F\left(\frac{1}{2}, \frac{1}{2}; 1; m\right)\,, \tag{4.19}$$

$$K'(m) = \frac{\pi}{2} F\left(\frac{1}{2}, \frac{1}{2}; 1; m_1\right)\,. \tag{4.20}$$

To calculate (ω_1, ω_2), the following expression is useful [51]:

$$z = \int_{\wp(z)}^{\infty} \frac{dt}{\sqrt{4t^3 - g_2 t - g_3}}\,. \tag{4.21}$$

For example, if one knows the values of the invariants and half-period values e_i and one wants to calculate ω_1, the following integral would have to be

evaluated:

$$\omega_1' = \int_{e_1}^{\infty} \frac{dt}{\sqrt{4t^3 - g_2 t - g_3}} \,. \tag{4.22}$$

It has been shown [51] that for the case $g_2 = 0$ and $g_3 > 0$, which corresponds to the hexagonal lattice (more on this shortly), integrals of the type (4.22) can be expressed in terms of elliptic integrals $K(m)$:

$$\omega_1' = \int_{e_1}^{\infty} \frac{dt}{\sqrt{4t^3 - g_3}} = \frac{2K(m)}{\sqrt{r+s}} \qquad (g_2 = 0,\, g_3 > 0)\,, \tag{4.23}$$

where $r \equiv (\sqrt{3} - 3/2)(2g_3)^{\frac{1}{3}}$, $s \equiv (\sqrt{3} + 3/2)(2g_3)^{\frac{1}{3}}$, and parameter m given by:

$$m = \sqrt{\frac{r}{r+s}} \qquad (g_2 = 0,\, g_3 > 0)\,. \tag{4.24}$$

Therefore, through eqs. (4.19, 4.23), one can express the period ω_1 in terms of hypergeometric functions F, for the case $g_2 = 0$ and $g_3 > 0$. Armed with this information, one can look in a book which lists hypergeometric functions with the appropriate values of the parameters $(a, b; c; m)$ (e.g. [50]); these are usually given in terms of gamma functions. We now discuss two different cases, with particular values of the invariants g_2 and g_3.

The case where $g_2 = 0$ and $g_3 = 4$ (as in [7]) corresponds to the hexagonal lattice, whereas the case where $g_2 = 1$ and $g_3 = 0$ corresponds to the square lattice [50]. More generally, these lattices fall within the "equianharmonic" and "lemniscatic" cases, respectively, which are defined in terms of the value of the modular discriminant $\Delta \equiv g_2^3 - 27 g_3^2$. The case where $\Delta < 0$ corresponds to the equianharmonic (hexagonal) case, whereas $\Delta > 0$ corresponds to the lemniscatic (square) case.

With these values for the invariants, one can determine the half-period values e_i of the Weierstrass function using eqs. (4.11, 4.12, 4.13). We get the

following values:

$$e_1 = \frac{1}{2}\,, \qquad e_2 = 0\,, \qquad e_3 = -\frac{1}{2} \qquad \text{(Square)} \tag{4.25}$$

$$e_1 = 1\,, \qquad e_2 = -\frac{1}{2}(1+\sqrt{3}i)\,, \qquad e_3 = -\frac{1}{2}(1-\sqrt{3}i) \text{ (Hexagonal)} \tag{4.26}$$

Having determined the e_i values, we can now obtain the value of the half-period ω_1' and parameter m for the square lattice (and, more generally, for $\Delta > 0$):

$$\omega_1' = \frac{K(m)}{\sqrt{e_1 - e_3}}\,, \tag{4.27}$$

$$m = \frac{e_2 - e_3}{e_1 - e_3}\,. \tag{4.28}$$

Note that the periods ω_2' for the hexagonal and square lattices are given in terms of ω_1', as follows:

$$\omega_2' = i\omega_1' \qquad \text{(Square)} \tag{4.29}$$

$$\omega_2' = \omega_1' e^{\frac{i\pi}{3}} \qquad \text{(Hexagonal)} \tag{4.30}$$

Eqs. (4.24, 4.28) give the following values for the parameters m and m_1:

$$m = \frac{1}{2}\,, \qquad m_1 = \frac{1}{2} \qquad \text{(Square)} \tag{4.31}$$

$$m = \frac{1}{2} - \frac{\sqrt{3}}{4}\,, \quad m_1 = \frac{1}{2} + \frac{\sqrt{3}}{4} \quad \text{(Hexagonal)} \tag{4.32}$$

We can now calculate the periods (ω_1, ω_2). Using eqs. (4.23, 4.27) for the half-periods, with the aforementioned values of the invariants, half-period values of the Weierstrass function (4.25, 4.26), and parameter values (4.31, 4.32), together with eq. (4.19) for the elliptic integrals K in terms of hypergeometric

functions, the periods are given by:

$$\omega_1 = \frac{\Gamma^2\left(\frac{1}{4}\right)}{2\sqrt{\pi}} \qquad \text{(Square)} \tag{4.33}$$

$$\omega_1 = \frac{\Gamma\left(\frac{1}{3}\right)\Gamma\left(\frac{1}{6}\right)}{2\sqrt{3\pi}} \quad \text{(Hexagonal)}\,. \tag{4.34}$$

Note that one might need to use certain properties of the gamma function in order to get the periods in the form of (4.33, 4.34) – see e.g. [50].

We are almost ready to write down the complex functions $W(z)$, used in the expressions for the fields Φ_β. There is just one more ingredient we need to define: the Jacobian elliptic functions. These can be defined in terms of the following integral:

$$z = \int_0^\phi \frac{d\theta}{\sqrt{1 - m\sin^2(\theta)}}\,, \tag{4.35}$$

where the angle ϕ is called the "amplitude". We shall be interested in the following functions, given in terms of the amplitude:

$$\mathrm{sn}(z|m) = \sin(\phi)\,, \quad \mathrm{cn}(z|m) = \cos(\phi)\,, \quad \mathrm{dn}(z|m) = \sqrt{1 - m\sin^2(\phi)}\,. \tag{4.36}$$

The functions $\mathrm{sn}(z|m)$ and $\mathrm{cn}(z|m)$ can be expressed in terms of (x_1, x_2), with $z \equiv x_1 + ix_2$, as follows [50]:

$$\mathrm{sn}(x_1 + ix_2|m) = \frac{\mathrm{sn}(x_1|m)\mathrm{dn}(x_2|m_1) + i\,\mathrm{cn}(x_1|m)\mathrm{dn}(x_1|m)\mathrm{sn}(x_2|m_1)\mathrm{cn}(x_2|m_1)}{\mathrm{cn}^2(x_2|m_1) + m\,\mathrm{sn}^2(x_1|m)\mathrm{sn}^2(x_2|m_1)}\,, \tag{4.37}$$

$$\mathrm{cn}(x_1 + ix_2|m) = \frac{\mathrm{cn}(x_1|m)\mathrm{cn}(x_2|m_1) - i\,\mathrm{sn}(x_1|m)\mathrm{dn}(x_1|m)\mathrm{sn}(x_2|m_1)\mathrm{dn}(x_2|m_1)}{\mathrm{cn}^2(x_2|m_1) + m\,\mathrm{sn}^2(x_1|m)\mathrm{sn}^2(x_2|m_1)}\,. \tag{4.38}$$

Note that the Jacobian elliptic functions $(\mathrm{sn}, \mathrm{cn}, \mathrm{dn})$ are quite common and are usually built into numerical computing programs. With this in mind, we now write down the Weierstrass functions for the square ($\Delta > 0$) and

hexagonal ($\Delta < 0$) lattices, in terms of these functions:

$$\wp(z) = e_3 + \frac{e_1 - e_3}{\mathrm{sn}^2(z|m)} \qquad (\Delta > 0) \tag{4.39}$$

$$\wp(z) = e_1 + H\left(\frac{1 + \mathrm{cn}(z'|m)}{1 - \mathrm{cn}(z'|m)}\right) \ (\Delta < 0)\,, \tag{4.40}$$

where $H^2 \equiv 2e_1^2 + e_2 e_3$ and $z' = 2\sqrt{H}z$.

It is worth noting that, due to the homogeneity properties of the Weierstrass function, one can rescale both the function and its argument: $W(z) = \lambda\wp(\varepsilon z)$, where λ and ε are real constants.

Using the aforementioned values of e_i for each lattice, we can now write down the expressions for $W(z)$ in the final form used for the ansatz (4.4)-(4.7):

$$W(z) = \lambda\left(-\frac{1}{2} + \frac{1}{\mathrm{sn}^2(\varepsilon z|m)}\right) \ \text{(Square)} \tag{4.41}$$

$$W(z) = \lambda\left(1 + \sqrt{3}\left(\frac{1 + \mathrm{cn}(\varepsilon z'|m)}{1 - \mathrm{cn}(\varepsilon z'|m)}\right)\right) \ \text{(Hexagonal)}\,. \tag{4.42}$$

In order to express the fields Φ_β as functions of the spatial coordinates (x_1, x_2, x_3), we use eqs. (4.37, 4.38) to express the functions $W(z)$ (4.41, 4.42) in terms of (x_1, x_2). We shall be using a value of $(\lambda, \varepsilon) = (1, 4K(m)/L_1)$ for the hexagonal lattice and $(\lambda, \varepsilon) = (2, 2K(m)/L_1)$ for the square lattice, with the respective values of m for each lattice (4.31, 4.32). These values of ε yield the fundamental domains: $(x_1, x_2) \in [0, \omega_1/\varepsilon] \times [0, \omega_1/\varepsilon] = [0, L_1] \times [0, L_1]$ for the square lattice and $(x_1, x_2) \in [0, \omega_1/\varepsilon] \times [0, \sqrt{3}\omega_1/\varepsilon] = [0, L_1] \times [0, \sqrt{3}L_1]$ for the hexagonal lattice. Note that, in order to make it easier for the purposes of carrying out numerical calculations, we have chosen to work with two fundamental parallelograms in the case of the hexagonal lattice (as in [7]), which yields a rectangular fundamental domain. This means that, since there is a double pole in each fundamental parallelogram, its charge (i.e. the degree of the map) is $Q = 4$, and for N hexagonal sheets $Q = 4N$. Since there is no need to do this for the square lattice, we use one fundamental

parallelogram, and thus, $Q = 2N$ for N square sheets.

4.2 Optimal periods

Now that we have an ansatz for both the square and hexagonal sheets, i.e. the fields Φ_β, eqs. (4.4-4.7), together with the corresponding functions $W(z)$, eqs. (4.41, 4.42), we can begin to look for the optimal periods (L_1, L_2) in the $(x_1, x_2)-$directions, respectively, with the period in the x_3-direction remaining at a large constant value of $L_3 = 14$. In particular, we shall focus on the 2-wall ($N = 2$), for both the square and hexagonal lattices. This exercise could easily be generalized to $N > 2$, provided one is careful with the boundary conditions in the energy-minimizing code for the fields in the x_3-direction; these being periodic for even N and antiperiodic for odd N (see [2]).

To find the optimal periods, we perform a full three-dimensional numerical minimization of the fields using the conjugate-gradient method on a triply-periodic lattice, with lattice spacing $h_1 = h_2 = h_3 \equiv h$, number of lattice points (n_1, n_2, n_3), and periods $(L_1, L_2, L_3) = h \cdot (n_1, n_2, n_3)$ in the $(x_1, x_2, x_3)-$directions, respectively. The energy E (a discretized version of the energy density (2.26), averaged along all three lattice directions) and charge Q (eq. (2.5), discretized similarly) are calculated by using a second-order finite difference method, with associated errors in the energy given by the difference between the calculated value of Q and the "true" value, given by $Q = 4N$ for N hexagonal sheets and $Q = 2N$ for N square sheets. We define the normalized energy E_N as the energy divided by the "true" value of the charge for each type of lattice: $E_N \equiv E/Q$.

We start by minimizing either the square or hexagonal lattice ansatz, with a certain value of the periods (L_1, L_2), while at the same time being careful about our chosen values of (n_1, n_2), such that the dimensions of the hexag-

onal lattice obey (or approximately obey) $L_2 = \sqrt{3}L_1$. The periods are subsequently increased by using the minimized ansatz as an initial condition, keeping h constant, and increasing (n_1, n_2), carried out by adding an appropriate number of copies of the lattice sites at the (x_1, x_2) edges of the configuration (with $x_3 \in [0, L_3]$) along the appropriate direction, minimizing again, and recording the new values of the energy E and charge Q. This procedure is then repeated, again using the minimized fields with the previous periods as an initial condition for minimization for the new periods, increased using the procedure outlined above, until an energy minimum is clearly seen. Since the behaviour of the energy as a function of the periods is approximately parabolic, we proceed by fitting a second-order polynomial to the three smallest $E-$values and obtaining its minimal value, along with the associated, optimal, value of the period.

To obtain an accurate value of E and Q for the square and hexagonal 2-walls, we scan through different values of L_1 using the aforementioned method, for three different values of the lattice spacing $h = (0.1, 0.15, 0.2)$, each time obtaining the minimal energy and associated values of the optimal periods and charge. We plot the resulting minimal values of E, Q, and L as functions of h^2 and, since there is a linear dependence in each case, we fit a line and read off their values at $h = 0$, i.e. we extrapolate $h \to 0$, yielding $E_N = 1.053 \pm 0.001$ and $E_N = 1.055 \pm 0.001$ for the square and hexagonal cases, respectively. These extrapolation plots can be seen in Fig. 4.1 for the square lattice and in Fig. 4.2 for the hexagonal lattice. It is worth noting that even though we quote the same errors for the energy and optimal periods, the latter are trickier to define as they generally correspond to shallow energy minima. However, comparing these with results from other sources typically shows that their difference is within about 1%. For example, in [2] the optimal period for the square 2-wall is given by $L_{1,2} = 4.47$, which can be compared with our own value of $L_{1,2} = 4.42$.

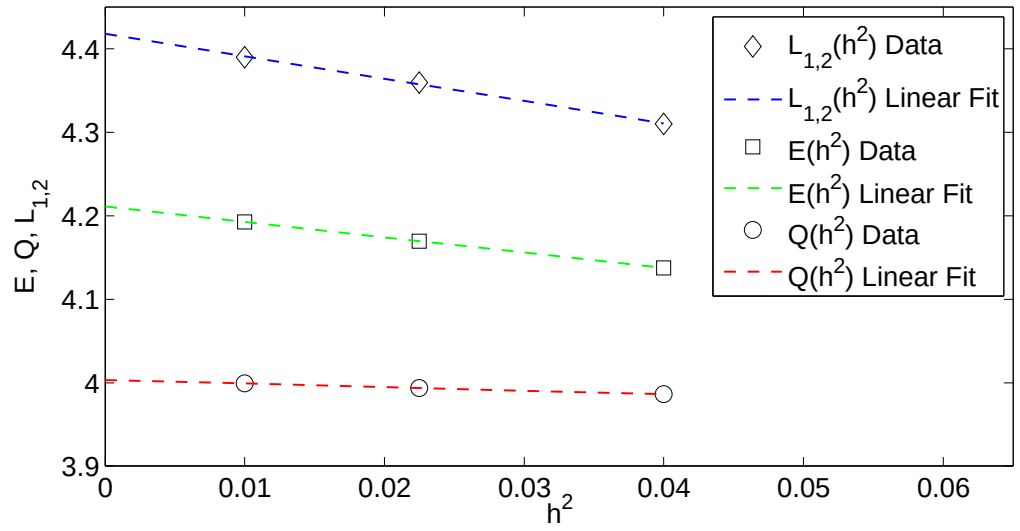

Figure 4.1: Minimal energies E, associated charges Q, and optimal periods $L_{1,2}$ of the square 2-wall for lattice spacings $h = (0.1, 0.15, 0.2)$, with linear fits. The extrapolated values are: $E(0) = 4.211 \pm 0.003$, $E_N(0) = 1.053 \pm 0.001$, $Q(0) = 4.003$, and $L_{1,2}(0) = 4.42 \pm 0.003$.

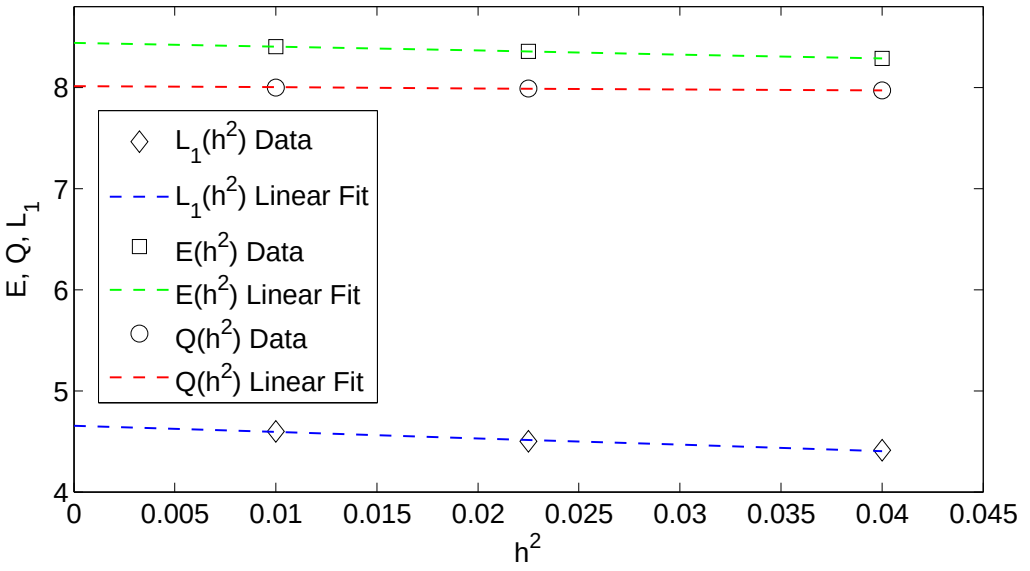

Figure 4.2: Minimal energies E, associated charges Q, and optimal periods $L_{1,2}$ of the hexagonal 2-wall for lattice spacings $h = (0.1, 0.15, 0.2)$, with linear fits. The extrapolated values are: $E(0) = 8.44 \pm 0.01$, $E_N(0) = 1.055 \pm 0.001$, $Q(0) = 8.01$, and $L_1(0) = 4.65 \pm 0.01$.

Before we move on to the topic of ($N > 2$) multi-walls, there are some important aspects of square and hexagonal 2-wall lattices, which we wish to emphasize. In the course of experimenting with relative sign changes of the walls' fields Φ_i (more on this shortly), we noticed while looking at the associated energy density isosurfaces of the hexagonal walls that they were shifted with respect to each other (in a case which turned out to have no relative sign change); this was possibly due to an applied random perturbation, which we use regularly before minimizing the energy each time, so as to prevent the configuration from becoming "stuck" in the course of trying to reach its energy minimum. We went on to investigate this in more detail by shifting one of the parallel, unshifted, walls by various amounts and then minimizing its energy, to see what is the threshold beyond which the configuration prefers to be shifted. It turns out that, even if one shifts one of the walls by 1 lattice spacing, the hexagonal configuration becomes shifted and its energy is reduced by about 0.3%. This means that the hexagonal 2-wall is unstable with respect to relative translations of its walls. For the square 2-wall, it is a different story. Shifting one of the walls and then minimizing its energy sees the configuration return to its original (unshifted) state, regardless of how much one shifts one of the walls.

Another feature we investigated is related to the relative signs between the fields of each wall. Recall that two well-separated $Q = 1$ Skyrmions attract each other when one is rotated by π with respect to the other about a line perpendicular to the line joining them. This is equivalent to changing the sign of two of the fields Φ_i of one of the Skyrmions, where $i = \{1, 2, 3\}$. It has been proposed (see e.g. [10]) that a similar effect occurs for two configurations of higher charge Q, but it is not always the case that both configurations can be made attractive through a suitable isospin transformation on one of them, and if they can become attractive, there is no prescription for which transformations to apply.

For the square and hexagonal 2-walls, we experimented with this idea by trying different configurations of sign changes for the fields Φ_i of one of the walls. We found that changing the sign of any two of these fields has the effect of further reducing the energy of the hexagonal walls by about 0.4%, besides the reduction in its energy due to the relative shift between the walls. For the square case, the combination of introducing a relative shift (even though the walls end up minimizing to a parallel configuration), besides having a similar sign change, reduces its energy by about 1%. Note that these techniques of shifting the walls and changing the signs of two of the fields were employed in the process of finding the minimal energies and optimal periods for the square and hexagonal 2-walls, outlined above.

The attractive effect of the sign change on the hexagonal 2-wall can be seen in the relative separation S between the walls, measured by calculating the distance between the highest peaks in the energy density of the 2-wall configuration at the origin, as a function of x_3. If one does not introduce any shifts and one has the signs unchanged, the parallel hexagonal walls have $S = 6.8$, and with the sign change, the separation is $S = 2.7$. Interestingly, with no shifts, the sign change has the opposite effect on the square 2-walls, with $S = 2.1$ and $S = 7.2$ for unchanged and changed signs, respectively.

A perturbation, in the form of a relative shift between the walls, has the effect of reducing the separation between the walls. With the signs changed, if one introduces a shift before minimizing, their separation after minimizing goes down to $S = 2.1$ (square case) and $S = 2.4$ (hexagonal case). This attractive effect, along with the relative shift between the hexagonal walls, can be seen in Figs. 4.3(a)-(d) and 4.4(a)-(d). These show the energy density isosurfaces $\mathcal{E}$ for the square and hexagonal 2-walls, respectively, with the signs of the fields (Φ_1, Φ_2) for one of the walls changed; the surfaces are at half of the energy density maximum $\mathcal{E} = 0.5 * \mathcal{E}_{\max}$. Figs. 4.3(a), (b) and 4.4(a), (b) depict the unshifted 2-walls, while Figs. 4.3(c), (d) and 4.4(c), (d) show the

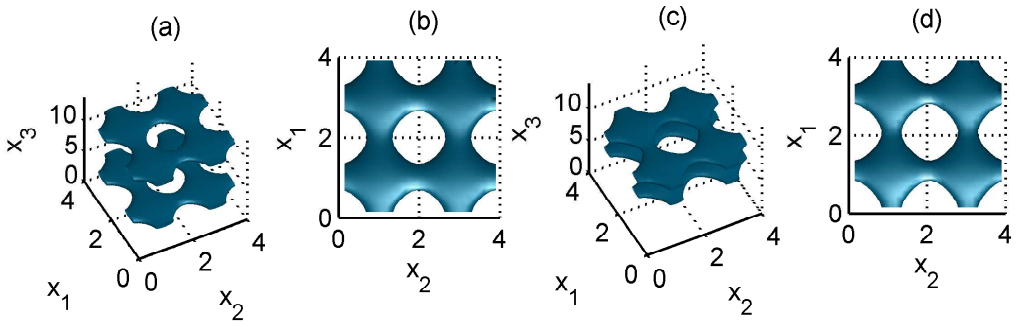

Figure 4.3: Energy density isosurfaces of the square 2-wall, with $\mathcal{E} = 0.5 * \mathcal{E}_{\max}$, and with the signs of the fields (Φ_1, Φ_2) changed. Figs. (a), (b) show the unshifted walls, while Figs. (c), (d) show the effect on the 2-wall by introducing a shift between the walls, which subsequently minimize to the same parallel configuration, but with smaller separation.

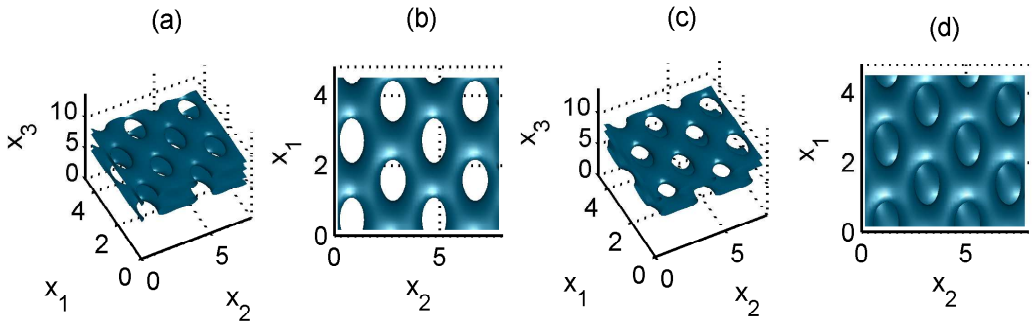

Figure 4.4: Energy density isosurfaces of the hexagonal 2-wall, with $\mathcal{E} = 0.5 * \mathcal{E}_{\max}$, and with the signs of the fields (Φ_1, Φ_2) changed. Figs. (a), (b), show the unshifted walls, while Figs. (c), (d), show the shifted walls with a slightly smaller separation, produced by introducing a shift between the walls before minimizing the configuration.

same configurations, but after introducing a shift.

4.3 Multi-wall solutions and stability

In the final section for this chapter, we wish to give a brief description of our experience in dealing with $(N > 2)$ multi-wall configurations. In particular, we shall focus on the $N = 4$ hexagonal lattice configuration in order to complement the findings of Prof. Richard Ward, which consist of unstable $N = 3$ hexagonal lattice configurations and stable $N > 2$ square configurations (see

[2]).

With the dual goal of analyzing the stability of the hexagonal 4-wall as well as finding out its optimal periods, we make use of two different methods, both of which involve calculating the first-order energy E of the configuration for different values of the periods (L_1, L_2), while keeping L_3 fixed at a large and constant value of $L_3 = 20$. The first method is similar to the one used in sec. 4.2, which involves scanning through different L_1 values (with $L_2 = \sqrt{3}L_1$), while the second method involves scanning through different values of (L_1, L_2) independently of each other (i.e. where the relationship $L_2 = \sqrt{3}L_1$ does not necessarily hold). The variation in the periods is carried out by keeping the lattice spacing h fixed and changing the numbers of lattice sites (n_1, n_2) along the edges of the configuration. This is done for three different values of lattice spacing $h = (0.1, 0.15, 0.2)$, in the hopes of performing an extrapolation $h \to 0$ in the energy E and the period L_1.

Our initial condition consists of stacking two copies, in the x_3-direction, of previously minimized hexagonal 2-walls. The constituent walls for each of these copies have been shifted with respect to each other and have opposite signs for the fields (Φ_1, Φ_2), so that they are in the attractive channel (see sec. 4.2). This configuration is then minimized and its periods are subsequently increased in the manner outlined above.

In the process of carrying out the calculations using the first method, we learned that the $h = 0.2$ case (for an unbeknownst reason) is rather unstable, in the sense that the energy density isosurfaces no longer exhibit hexagonal symmetry for certain L_1 values. The periods that we scanned through are given by: $(L_1, L_2) = (4.4, 7.6), (4.6, 8.0), (4.8, 8.4), (5.0, 8.6)$, and $(5.2, 9.0)$. Note that since the number of lattice sites (n_1, n_2) are, by definition, integers one cannot always satisfy the relation $L_2 = \sqrt{3}L_1$. Therefore, we have chosen numbers of lattice sites, such that the corresponding values of the periods approximately follow the aforementioned relation. Fig. 4.5 (a)-(e) shows the

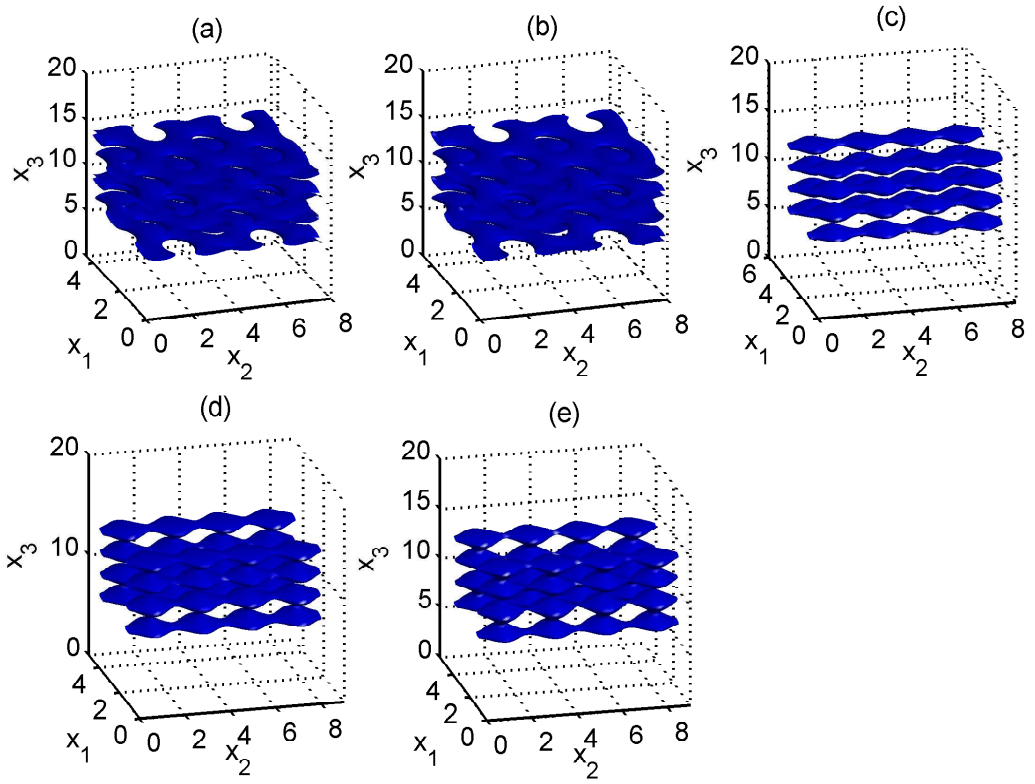

Figure 4.5: Energy density isosurfaces for a hexagonal 4-wall initial condition ($h = 0.2$), with $\mathcal{E} = 0.5 * \mathcal{E}_{\max}$. Figs. (a)-(e) have the periods $(L_1, L_2) = (4.4, 7.6), (4.6, 8.0), (4.8, 8.4), (5.0, 8.6), (5.2, 9.0)$ and normalized energies $E_N = 1.037, 1.034, 1.033, 1.030, 1.035$, respectively.

energy density isosurfaces $\mathcal{E} = 0.5 * \mathcal{E}_{\max}$ for the hexagonal 4-wall ($h = 0.2$) initial condition mentioned earlier, with the quoted values of the periods (L_1, L_2), in that order. Figs. 4.5 (a), (b) show the hexagonal 4-wall, while Fig. 4.5 (c) shows a non-hexagonal configuration that has separated in the x_1-direction, but is still merged in the x_2-direction, and in Figs. 4.5 (d), (e), such a configuration has also merged in the x_3-direction. As we minimize the configuration for this set of periods we notice the energy has an approximately parabolic behaviour, as was the case with the optimal period analysis of sec. 4.2, with a minimum normalized energy of $E_N = 1.030$ corresponding to Fig. 4.5 (d).

We should emphasize that a similar exercise has shown that a hexagonal 4-wall initial condition is stable for the lattice spacings $h = (0.1, 0.15)$, keeping

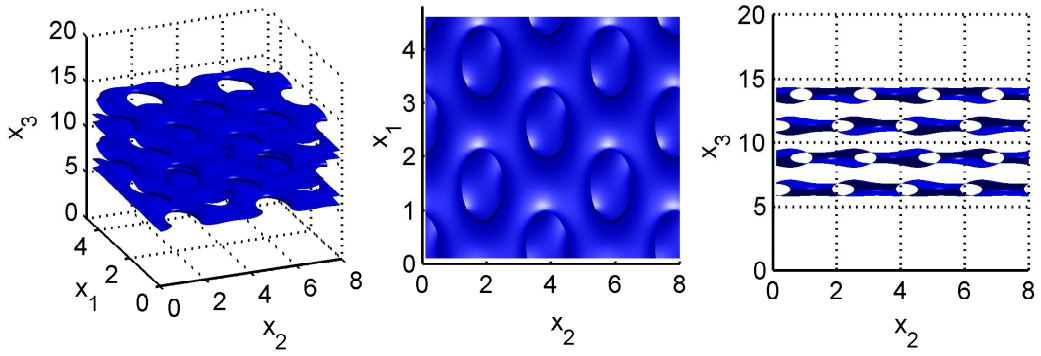

Figure 4.6: Different views of the energy density isosurface ($\mathcal{E} = 0.5 * \mathcal{E}_{\max}$) of a hexagonal 4-wall with $h = 0.1$, $E_N = 1.047$, and $(L_1, L_2) = (4.6, 8.0)$.

its hexagonal symmetry throughout a similar range of periods. A representative example can be seen in Fig. 4.6, which shows three different views of the energy density isosurface corresponding to the minimal-energy $h = 0.1$ configuration, with $E_N = 1.047$ and $(L_1, L_2) = (4.6, 8.0)$; the minimal-energy configuration for the $h = 0.15$ case has $E_N = 1.041$ and $(L_1, L_2) = (4.65, 8.1)$. Note that since we have no corresponding minimal-energy configuration with hexagonal symmetry for $h = 0.2$ we cannot proceed with a reliable and accurate linear extrapolation in h^2 for E and L_1, since we need at least three points to make sure we have a linear dependence.

Even though we could have looked for a value of $h \neq (0.1, 0.15, 0.2)$, with a minimal-energy hexagonal 4-wall configuration, we decided this is not worth pursuing since an application of the aforementioned second method shows that the relation $L_2 = \sqrt{3}L_1$ is not the optimal one. Our second method of stability analysis consists of finding the optimal values (L_1, L_2) by picking a range of values for each of these periods and scanning through them independently of each other. This is done by fixing a value of L_1, scanning through the whole range of values of L_2 and making a plot of the energy values E vs L_2 (which is usually approximately parabolic), then we change the fixed value of L_1 and repeat the process, until we have gone through our chosen range of values of L_1. This exercise was performed for the lattice spacings $h = (0.15, 0.2)$ and, since our original guess for the optimal periods

was wrong, we ended up scanning through two different sets of values for the periods, for both lattice spacings. Our results consistently show a tendency for the lowest energy to correspond to the highest chosen values of L_1 and the lowest of L_2; these being $(L_1, L_2) = (4.8, 7.0)$ with $E_N = 1.032$ for the $h = 0.2$ case and $(L_1, L_2) = (4.95, 7.5)$ with $E_N = 1.041$ for the $h = 0.15$ case. Furthermore, since these periods are at the ends of our chosen range of values, the optimal periods (L_1, L_2) are likely to be even closer together. While the energy density isosurfaces corresponding to the lowest-energy values that we found still have hexagonal symmetry, it is likely that this will no longer be the case for the optimal periods, should these end up being closer together in value. The reason for this being that such a set of periods would no longer conform to the relation satisfied by a lattice featuring hexagonal symmetry.

There are two issues that we now wish to raise, as a way of concluding this chapter. One is that more work needs to be done to find the optimal periods for the hexagonal ($N > 2$) multi-walls and to analyze the corresponding energy density isosurfaces. The other is related to one of the motivations behind the paper by Battye and Sutcliffe [7]; the idea being that one can think of an $N = 1$ hexagonal lattice as the infinite limit of a shell-like skyrmion, which contains hexagons and pentagons, provided one inserts an appropriate number of pentagon defects. To be precise, the lattice would correspond to the bottom portion of a shell-like skyrmion in this limit, since the vacuum values on either side coincide with such a configuration – i.e. the region below(above) the lattice corresponds to the outside(inside) of the shell with $\Phi_4 = +1(-1)$. If we stick with this idea, then our multi-walls ($N > 1$) would correspond to skyrmions composed of nested shells, provided one has the correct vacuum values on either side of the multi-wall configuration, which would correspond to an odd number of walls. Our results, coupled with the $N > 2$ square multi-wall and $N = 3$ hexagonal multi-wall results from Prof. Ward [2], would therefore suggest that the square multi-wall config-

uration would be the better "material" out of which one can build nested shell-like skyrmions, since they have slightly lower normalized energy (for $N = 2$) and are seemingly more stable (for $N > 2$).

Part III

Generalized Skyrme Lattices

Chapter 5

The generalized Skyrme crystal

Up to now, we have been considering certain types of lattices in the Skyrme model – Skyrme crystals, square, and hexagonal Skyrme "sheets". It is now time to discuss lattices in the context of generalized skyrme systems, moving away from the $\alpha = 0$ limit and letting $\alpha \in [0, 1)$. In this chapter, we present triply-periodic ("crystalline") solutions and, in Chapter 6, we shall be dealing with multi-vortex configurations.

5.1 Geometrical considerations

We start this chapter by generalizing the discussion of sec. 2.2, which reviews some of the results of Manton's geometrical take on the Skyrme model [24], by putting it in the context of Ward's generalized skyrme systems [4]. In other words, we want to incorporate the parameter α into the results. This can be done by letting the domain and target manifolds, S and Σ, be squashed 3-spheres with parameters α and α', respectively, rather than dealing with standard 3-spheres.

The first task is to calculate the distortion tensor D, introduced in sec. 2.2, for the case of the domain and target spaces having metrics H^{ab} and H'_{jl} with

parameters α and α', respectively; note that $H^{ab}H_{ac} = \delta^b_c$.

Recall from sec. 2.4.2 that the distortion tensor is given by contracting the indices of the domain and target metrics with the derivatives of the coordinate maps $\pi : S \to \Sigma$ as follows:

$$D^k_j = H^{ab}H'_{jl}\pi^l_a\pi^k_b\,, \tag{5.1}$$

where $\pi^l_a \equiv \frac{\partial \pi^l}{\partial p^a}$ and π^l, p^a are normal coordinates on Σ and S, respectively.

We start by expressing the Z fields in terms of the 3-sphere coordinates (μ, ϕ_1, ϕ_2) as follows:

$$Z_1 \equiv \sin(\mu)e^{i\phi_1} \qquad , \qquad Z_2 \equiv \cos(\mu)e^{i\phi_2}\,, \tag{5.2}$$

where $\mu \in [0, \pi/2]$ and $\phi_1, \phi_2 \in [0, 2\pi]$. Using eq. (2.32) for the Berger sphere metric, together with Z_1, Z_2 from (5.2), we get the following Berger sphere components:

$$H^{ab} = \begin{pmatrix} 1 & 0 & 0 \\ 0 & \frac{1}{s^2} + \frac{\alpha}{1-\alpha} & \frac{\alpha}{1-\alpha} \\ 0 & \frac{\alpha}{1-\alpha} & \frac{1}{c^2} + \frac{\alpha}{1-\alpha} \end{pmatrix} \qquad , \qquad H'_{jl} = \begin{pmatrix} 1 & 0 & 0 \\ 0 & s^2 - \alpha' s^4 & -\alpha' s^2 c^2 \\ 0 & -\alpha' s^2 c^2 & c^2 - \alpha' c^4 \end{pmatrix}, \tag{5.3}$$

where $c \equiv \cos(\mu)$ and $s \equiv \sin(\mu)$.

If we now consider π^l_a and π^k_b as identity maps δ^l_a and δ^k_b, respectively, we can now calculate the distortion tensor using the metric components from eq. (5.3), as follows:

$$D^k_j = H^{ab}H'_{jl}\pi^l_a\pi^k_b = H^{ab}H'_{jl}\delta^l_a\delta^k_b = H^{lk}H'_{jl} \tag{5.4}$$

$$= \begin{pmatrix} 1 & 0 & 0 \\ 0 & \frac{1-\alpha c^2 - \alpha' s^2}{1-\alpha} & \frac{s^2(\alpha - \alpha')}{1-\alpha} \\ 0 & \frac{c^2(\alpha - \alpha')}{1-\alpha} & \frac{1-\alpha s^2 - \alpha' c^2}{1-\alpha} \end{pmatrix}. \tag{5.5}$$

The eigenvalues of this matrix are: $\lambda_1^2 = 1$, $\lambda_2^2 = 1$, and $\lambda_3^2 = \frac{\alpha'-1}{\alpha-1}$.

With this information, we can now calculate the energy of the generalized Skyrme system:

$$\begin{aligned} \mathcal{E}_2 &= \kappa_2 \mathrm{Tr}(D) = \kappa_2(\lambda_1^2 + \lambda_2^2 + \lambda_3^2) = \kappa_2 \left(2 + \frac{\alpha' - 1}{\alpha - 1}\right), \qquad (5.6) \\ \mathcal{E}_4 &= \frac{\kappa_4}{2}\left[(\mathrm{Tr}(D))^2 - \mathrm{Tr}(D^2)\right] = \kappa_4\left(\lambda_1^2\lambda_2^2 + \lambda_2^2\lambda_3^2 + \lambda_3^2\lambda_1^2\right) \\ &= \kappa_4\left[1 + 2\left(\frac{\alpha' - 1}{\alpha - 1}\right)\right]. \qquad (5.7) \end{aligned}$$

In order to calculate the energies E_2 and E_4 we first determine the volume of the domain space (Vol S). This can be carried out through the use of the domain space metric, with components H_{jl} from eq. (5.3), as follows:

$$\text{Vol } S = \int \sqrt{|H|}\, d\phi_1\, d\phi_2\, d\mu = 2\pi^2\sqrt{1-\alpha}\,, \qquad (5.8)$$

where $|H| \equiv |\det\, H_{jl}|$. The equivalent expression for the volume of the target space would be Vol $\Sigma = 2\pi^2\sqrt{1-\alpha'}$, which can be applied to the topological bound (2.10) from sec. 2.2:

$$E \geq 6(\deg\, \pi)(\text{Vol } \Sigma) = 12\pi^2(\deg\, \pi)\sqrt{1-\alpha'}\,, \qquad (5.9)$$

where (deg π) refers to the degree of the map π. Coming back to the energies E_2 and E_4, we can use eq. (2.7) to find:

$$\begin{aligned} E_2 &= \kappa_2(\text{Vol } S)\Big(2 + \frac{\alpha' - 1}{\alpha - 1}\Big) = 2\kappa_2\pi^2\sqrt{1-\alpha}\Big(2 + \frac{\alpha' - 1}{\alpha - 1}\Big), \qquad (5.10) \\ E_4 &= \kappa_4(\text{Vol } S)\left[1 + 2\Big(\frac{\alpha' - 1}{\alpha - 1}\Big)\right] = 2\kappa_4\pi^2\sqrt{1-\alpha}\left[1 + 2\Big(\frac{\alpha' - 1}{\alpha - 1}\Big)\right]. \qquad (5.11) \end{aligned}$$

Note that the energy $E = E_2 + E_4$ reduces to eq. (2.22), when $\alpha = 0$ and $\alpha' \equiv \alpha$, as was the case there.

A different topological bound can be derived through the use of the virial theorem[1]. Using $E \equiv \kappa_2 E_2 + \kappa_4 E_4$ together with eq. (5.9), we derive the following bound:

$$E \geq 3Q\sqrt{\frac{(1-\alpha')}{(3-\alpha')(3-2\alpha')}}\,, \tag{5.12}$$

where $Q = \deg \pi$ is the baryon number and eqs. (2.23, 2.24) have been used for κ_2 and κ_4.

Note that for the Skyrme model ($\alpha' = 0$) the inequality reduces to: $E \geq Q$. Recall that there is a stronger bound than the one given by eq. (2.10) (i.e. eq. (2.11)) by considering a target manifold that is isotropically bigger than the domain manifold. We have made attempts to apply this to generalized skyrme systems, but it is a tricky enterprise, since the squashed 3-sphere is not an object that is deformed isotropically as the parameter α is varied. If the bound (5.12) can be improved, then it can be done perhaps by adding an additional term such that it reduces to the Skyrme-Faddeev energy bound, introduced in sec. 2.3, $E \geq |Q|^{3/4}$ when $\alpha = 1$.

5.2 Symmetries

In an effort to learn more about the properties of generalized skyrme systems, we have decided to look at how the generalized energy density, eq. (2.26), and the components of the Berger sphere metric H, eq. (2.32), change under the symmetry generators of the Skyrme crystal (Tables 2.1 and 2.2) as well as other transformations. Note that, unlike in sec. 5.1, here we denote the target space metric H and the domain space metric corresponds to that of the standard 3-sphere (i.e. the fields Φ_β are maps $S^3 \mapsto S^3_\alpha$).

[1]Generally speaking, the virial theorem states that if $E = aE_2 + bE_4$, where a and b are constants, then $E \geq (ab)^{\frac{1}{2}}M$, where M is a minimum of the energy functional $E[\phi] = E_2[\phi] + E_4[\phi]$, for some choice of the field ϕ.

This was done using symbolic manipulation software by expressing both the generalized energy density and the Berger sphere metric in terms of the fields Φ_β and their derivatives, yielding functions $f(\Phi_\beta, \partial_i\Phi_\beta)$. We then apply the aforementioned transformations of the fields $\Phi_\beta \to \Phi'_\beta$, producing transformed functions $f(\Phi'_\beta, \partial_i\Phi'_\beta)$. Finally, we subtract the transformed functions from the original ones: $f(\Phi_\beta, \partial_i\Phi_\beta) - f(\Phi'_\beta, \partial_i\Phi'_\beta) \equiv g(\Phi_\beta, \partial_i\Phi_\beta)$, using the assumptions $\Phi_\beta^2 = 1$ and $\Phi_\beta\partial_i\Phi_\beta = 0$. If $g(\Phi_\beta, \partial_i\Phi_\beta) = 0$, then we know that the symmetry has "survived" the transition to generalized skyrme systems. In such a case, we write down a check mark next to that transformation in Table 5.1. If it does not survive the transition, we write down a cross next to it. The transformations that we checked for both the generalized energy density $\mathcal{E}$ and the Berger sphere metric components H, for $\alpha = 0$ and $\alpha \in (0, 1]$, are listed in Table 5.1 with the original state being $(\Phi_1, \Phi_2, \Phi_3, \Phi_4)$.

Not all of the symmetries of the Skyrme crystal survived the transition to the generalized Skyrme system. Assuming that the underlying spatial transformations are the same as in the Skyrme crystal case, it is rather surprising that reflection symmetries ($x_i \mapsto -x_i$) (i.e. $\Phi_i \mapsto -\Phi_i$) no longer hold in generalized skyrme systems, producing functions $g(\Phi_\beta, \partial_i\Phi_\beta)$ that are proportional to the parameter α in both the generalized energy density and in some of the Berger sphere components, as is the case in all symmetries that do not hold. However, note that we are considering generic fields Φ_β. One might have to explicitly substitute expressions for the fields into the functions $f(\Phi_\beta, \partial_i\Phi_\beta)$ and $f(\Phi'_\beta, \partial_i\Phi'_\beta)$ in order to see if certain transformations, such as reflections, really do survive the transition to generalized skyrme systems.

Something can be learned about generalized skyrme systems by looking at the symmetries that do survive. These include $\pi-$rotations about each of the 3 axes:

$$(\Phi_1, -\Phi_2, -\Phi_3, \Phi_4), (-\Phi_1, \Phi_2, -\Phi_3, \Phi_4), (-\Phi_1, -\Phi_2, \Phi_3, \Phi_4)\,,$$

as well as $\pi/2-$rotations about the $z-$axis, in both directions:

$$(\Phi_2, -\Phi_1, \Phi_3, \Phi_4), (-\Phi_2, \Phi_1, \Phi_3, \Phi_4)\,.$$

Note that a torus sitting on the $(x, y)-$plane, with the $z-$axis going through its centre, would have these same symmetries. Perhaps these surviving symmetries also reflect the fact that the squashed 3-sphere is only squashed along one direction.

If we think in terms of Skyrme crystal transformations, the other symmetries that survive:

$$(-\Phi_1, \Phi_2, \Phi_3, -\Phi_4), (\Phi_1, -\Phi_2, \Phi_3, -\Phi_4), (\Phi_1, \Phi_2, -\Phi_3, -\Phi_4)$$

correspond to $L/2-$translations along each of the axes. The successive application of these (i.e. a translation from the origin to the centre of a cube with side length L) corresponds to the other surviving symmetry: $(-\Phi_1, -\Phi_2, -\Phi_3, -\Phi_4)$.

The remaining surviving symmetries that we list are harder to explain in terms of three-dimensional space, as they involve transformations with the Φ_4 field (SO(4) rotations). Note that we only checked a few of these, so there might be more symmetries that we do not list.

Table 5.1: Symmetries of Generalized Skyrme Systems

Transformation	$\alpha = 0$		$\alpha \in (0, 1]$	
	H	$\mathcal{E}$	H	$\mathcal{E}$
$(-\Phi_1, \Phi_2, \Phi_3, \Phi_4)$	√	√	×	×
$(\Phi_1, -\Phi_2, \Phi_3, \Phi_4)$	√	√	×	×
$(\Phi_1, \Phi_2, -\Phi_3, \Phi_4)$	√	√	×	×
$(-\Phi_1, -\Phi_2, \Phi_3, \Phi_4)$	√	√	√	√
$(\Phi_1, -\Phi_2, -\Phi_3, \Phi_4)$	√	√	√	√
$(-\Phi_1, \Phi_2, -\Phi_3, \Phi_4)$	√	√	√	√
$(-\Phi_1, -\Phi_2, -\Phi_3, \Phi_4)$	√	√	×	×
$(\Phi_2, \Phi_3, \Phi_1, \Phi_4)$	√	√	×	×
$(\Phi_3, \Phi_1, \Phi_2, \Phi_4)$	√	√	×	×
$(\Phi_1, \Phi_3, \Phi_2, \Phi_4)$	√	√	×	×
$(\Phi_3, \Phi_2, \Phi_1, \Phi_4)$	√	√	×	×
$(\Phi_2, \Phi_1, \Phi_3, \Phi_4)$	√	√	×	×
$(\Phi_1, \Phi_3, -\Phi_2, \Phi_4)$	√	√	×	×
$(\Phi_3, \Phi_2, -\Phi_1, \Phi_4)$	√	√	×	×
$(\Phi_2, -\Phi_1, \Phi_3, \Phi_4)$	√	√	√	√
$(-\Phi_2, \Phi_1, \Phi_3, \Phi_4)$	√	√	√	√
$(-\Phi_2, -\Phi_1, \Phi_3, \Phi_4)$	√	√	×	×
$(\Phi_1, -\Phi_3, \Phi_2, \Phi_4)$	√	√	×	×
$(\Phi_1, -\Phi_3, -\Phi_2, \Phi_4)$	√	√	×	×
$(-\Phi_3, \Phi_2, \Phi_1, \Phi_4)$	√	√	×	×
$(-\Phi_3, \Phi_2, -\Phi_1, \Phi_4)$	√	√	×	×
$(-\Phi_1, \Phi_2, \Phi_3, -\Phi_4)$	√	√	√	√
$(\Phi_1, -\Phi_2, \Phi_3, -\Phi_4)$	√	√	√	√
$(\Phi_1, \Phi_2, -\Phi_3, -\Phi_4)$	√	√	√	√
$(-\Phi_1, -\Phi_2, \Phi_3, -\Phi_4)$	√	√	×	×
$(-\Phi_1, \Phi_2, -\Phi_3, -\Phi_4)$	√	√	×	×
$(\Phi_1, -\Phi_2, -\Phi_3, -\Phi_4)$	√	√	×	×
$(-\Phi_1, -\Phi_2, -\Phi_3, -\Phi_4)$	√	√	√	√
$(\Phi_1, \Phi_2, \Phi_4, \Phi_3)$	√	√	×	×
$(\Phi_1, \Phi_2, \Phi_4, -\Phi_3)$	√	√	√	√
$(\Phi_1, \Phi_2, -\Phi_4, \Phi_3)$	√	√	√	√
$(\Phi_2, \Phi_1, \Phi_4, -\Phi_3)$	√	√	×	×
$(-\Phi_2, \Phi_1, \Phi_4, -\Phi_3)$	√	√	√	√
$(\Phi_2, -\Phi_1, \Phi_4, -\Phi_3)$	√	√	√	√
$(-\Phi_2, -\Phi_1, \Phi_4, -\Phi_3)$	√	√	×	×
$(-\Phi_2, -\Phi_1, -\Phi_4, -\Phi_3)$	√	√	√	√
$(\Phi_2, \Phi_1, \Phi_4, \Phi_3)$	√	√	√	√

5.3 Behaviour as a function of α

In this section, we investigate triply-periodic crystalline solutions of generalized skyrme systems. These efforts were originally motivated by the question: what does the Skyrme crystal look like as a function of α? More specifically, what are the qualitative features of its energy density isosurfaces and the symmetries of the corresponding fields? As we shall see, when we approach the Skyrme-Faddeev model ($\alpha \to 1$), the answer to this question is related with vortex/antivortex configurations. This led us to explore such configurations, using a multi-vortex ansatz, in the context of generalized skyrme

systems with a focus on large periods in the $x-$ and $y-$ directions (i.e. isolated vortex configurations). A study of vortex configurations, in turn, led to the discovery of two triply-periodic solutions, as we shall see in sections 5.3.2 and 5.3.3. However, even though they are inextricably linked, since the purpose for this chapter is to discuss solutions which are not isolated but rather triply-periodic, as was the original motivation for the Skyrme crystal (see sec. 2.5), a detailed discussion of generalized vortex configurations has been relegated to chapter 6.

5.3.1 The V+AV+V+AV solution

We start by describing the techniques used in obtaining triply-periodic solutions to generalized Skyrme systems. As in Part II, we impose triply-periodic boundary conditions in an $n_x \times n_y \times n_z$ grid; however, we now have a non-zero value of the parameter α, which introduces extra terms in the energy density (see sec. 2.4) and energy gradient. The latter is used in the conjugate-gradient method of energy minimization, while the former is used in determining the energy of the relevant fields at each step of the minimization process. Moreover, for this section, we start each minimization procedure with an initial condition given by an approximate triply-periodic solution, which corresponds to the Skyrme crystal ansatz (eqs. (2.97, 2.98)), and subsequently minimizing it.

Our goal is to find the optimal periods for different values of α, i.e. the values of the periods in the $x-$, $y-$, and $z-$directions given by: $L_{x,y_{\min}} \equiv L_{x\min} = L_{y_{\min}}$ and $L_{z\min}$, which correspond to the periods at the minima of the energy plotted as a function of $L_{x,y}$ and L_z, respectively, for each value of α. This could be done in a variety of ways. However, in this section, we use a technique that is slightly different than that of sections 5.3.2 and 5.3.3. It is one which takes somewhat more computer processing time, but yields precise values for the optimal periods.

We start with the $\alpha = 0$ case. The procedure consists of starting with a relatively low value for the periods. Since we know that the Skyrme crystal has optimal periods $L_{x,y,z} = 4.71$ (see e.g. [47]), we start with a lower value of $L_{x,y,z} = 4.4$ and increase it up to $L_{x,y,z} = 5.0$. This was done as a way of verifying the results in the literature, while at the same time testing our own procedure. We increase $L_{x,y,z} \equiv h_{x,y,z} * n_{x,y,z}$ (recall that $h_{x,y,z}$ is the lattice size) by keeping $h_{x,y,z}$ constant and increasing the number of lattice points in the $x-$, $y-$, and $z-$directions – carried out by adding a copy of the lattice points along the edges of the grid in all three directions. We proceed by minimizing the fields, and then calculating the energy E and charge Q of the minimized fields using a first-order finite difference method. This is repeated for the aforementioned range of $L_{x,y,z}$ values and a plot of the energy as a function of the period $L_{x,y,z}$ is produced. We then fit a second-order polynomial to the three lowest-energy data points (since such a function is usually a good fit) and determine the minimum-energy value and corresponding "optimal" period of the fit; we also determine the approximate charge of the minimal-energy configuration by comparing the charges of two configurations whose periods are closest in value to the optimal one and interpolating. The optimal periods, charges, and energies are calculated for three different values of lattice size: $h_{x,y,z} = 0.1, 0.15, 0.2$ and we plot them as functions of h^2, since these are proportional to h^2. Finally, we fit a line through these points, extrapolate in h^2, and read off their values at $h = 0$ (see Fig. 5.1). The extrapolated optimal periods $(L_{x,y}, L_z)$ for $\alpha \geq 0$, along with the associated energy (E) and normalized energy $(E_N \equiv E/4)$ are listed in Table 5.2, where the error in E_N is given by $(Q-4)/4$, with Q calculated at $h = 0$.

The procedure used in determining the optimal periods for $\alpha > 0$ is slightly different, since $L_{x,y_{\min}}$ and $L_{z\min}$ are no longer necessarily equal to each other – the main difference being that $L_{x,y}$ is varied independently from L_z. That is, we take a certain value of $L_{x,y}$, fix it, vary L_z, and make a note of the minimal

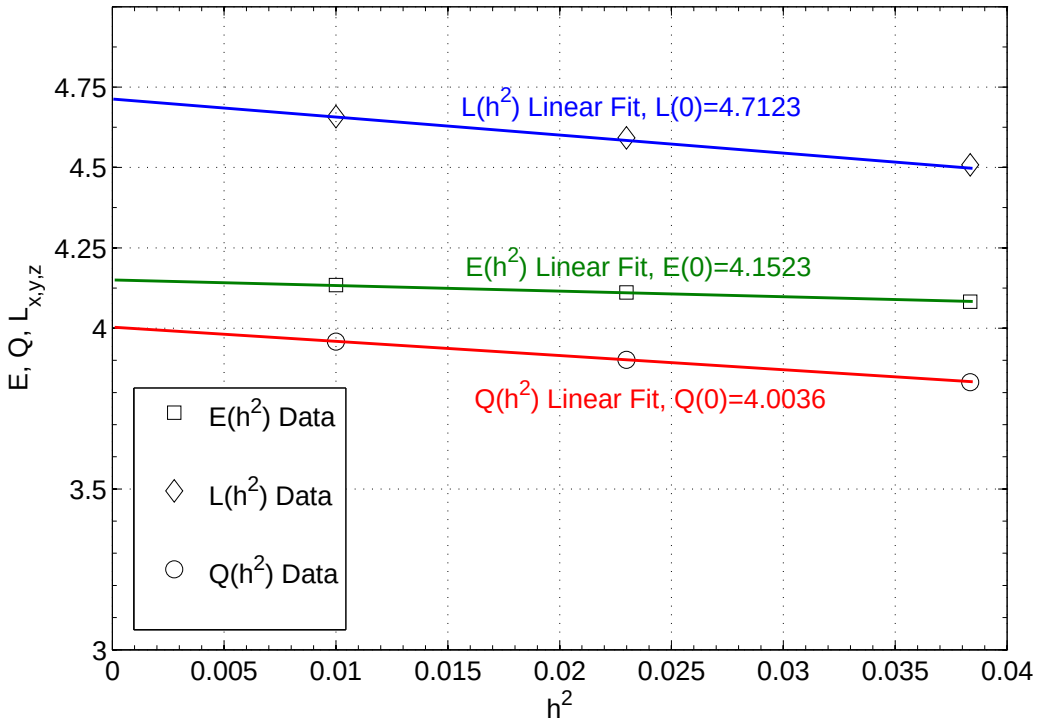

Figure 5.1: Skyrme crystal ($\alpha = 0$) optimal periods $L_{x,y,z}$ with a blue linear fit, charges Q with a red linear fit, and energies E with a green linear fit, calculated with $h^2 = 0.01, 0.023, 0.038$.

energy value $E(L_{z\min})$, along with the associated value of $L_{z\min}$, calculating these by fitting a second-order polynomial, as in the $\alpha = 0$ case. This is then repeated for a range of $L_{x,y}$ values, until we find that we have enough information to also determine an optimal value of $L_{x,y}$. We then produce a plot of the minimal-energy $E(L_{z\min})$ values for each value of $L_{x,y}$ and fit a polynomial to these points to find a "global" energy minimum $E'(L'_{z\min})$, along with its associated optimal "global" $L'_{z\min}$ value. Finally, to find the associated "global" value of $L_{x,y_{\min}}$, we interpolate by fitting a second-order polynomial to a series of points on an $L_{x,y}$ vs. $L_{z\min}$ plot and determining what the value of $L_{x,y} \equiv L_{x,y_{\min}}$ is for $L'_{z\min}$. This process is repeated for $h_{x,y,z} = 0.1, 0.15, 0.2$, as was done for the $\alpha = 0$ case, and we determine the optimal periods $L_{x,y}$, L_z, and minimal energies E, for different values of α, by extrapolating $h^2 \to 0$. These, along with the normalized energies E_N with associated errors (as calculated for the $\alpha = 0$ case) are listed in Table 5.2; we plot these values as functions of α: $L_{x,y}(\alpha)$, $L_z(\alpha)$, and $E_N(\alpha)$ in Figs. 5.2 and 5.3, respectively.

Table 5.2: Optimal periods, minimal energies, and normalized energies ($E_N \equiv E/4$) of V+AV+V+AV solution

α	$L_{x,y}$	L_z	E	E_N
0	4.7123	4.7123	4.1523	1.0381 ± 0.0009
0.3	5.112	4.267	4.135	1.034 ± 0.001
0.6	5.761	3.776	4.046	1.011 ± 0.002
0.9	6.906	3.197	3.762	0.941 ± 0.004
0.95	7.514	3.015	3.672	0.918 ± 0.004

In Fig. 5.4, we plot the energy density $\mathcal{E}$ of the minimal-energy fields for $\alpha = 0, 0.3, 0.6, 0.95$, where $\mathcal{E}$ is 0.6 times the maximum value. Note that, as α increases, the half-skyrmions of the Skyrme crystal merge pairwise in the $z-$direction, becoming more homogeneous in the $z-$direction as $\alpha \to 1$. In fact, in this limit, the fields can be described as vortices; more specifically, a pair of vortices and a pair of antivortices. We now turn to a brief discussion of vortex fields.

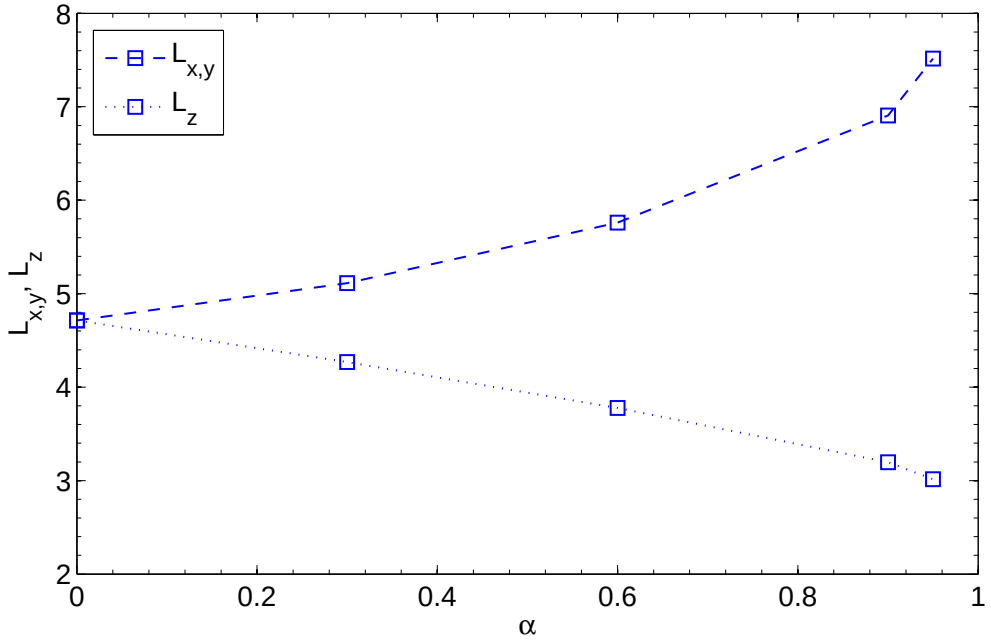

Figure 5.2: V+AV+V+AV optimal periods $L_{x,y}$ and L_z as a function of the parameter α.

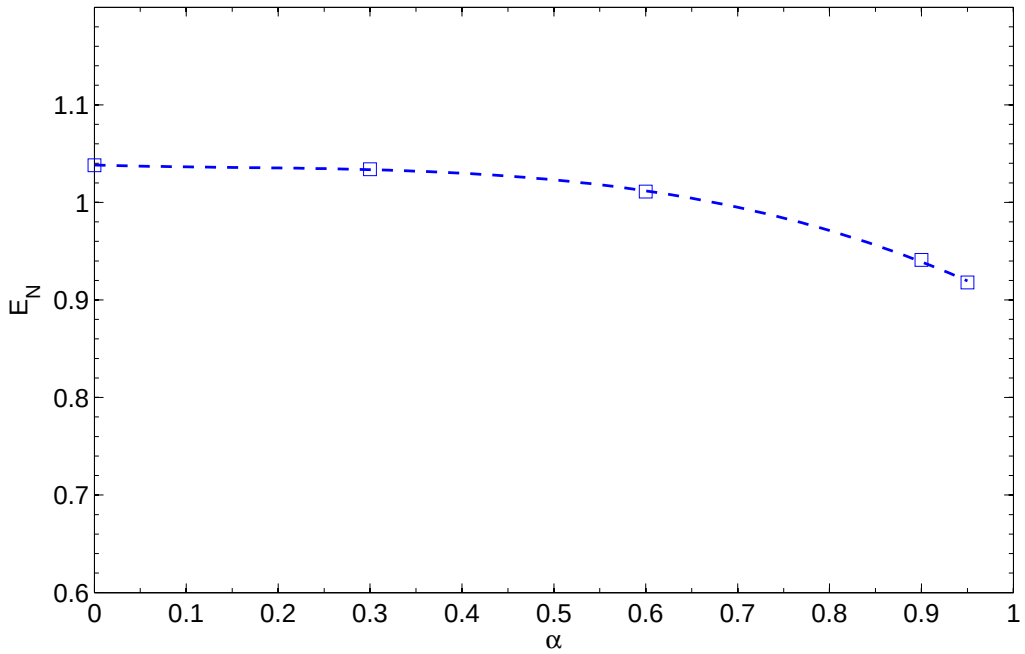

Figure 5.3: V+AV+V+AV normalized energy, as a function of the parameter α with a fitted polynomial of order 3.

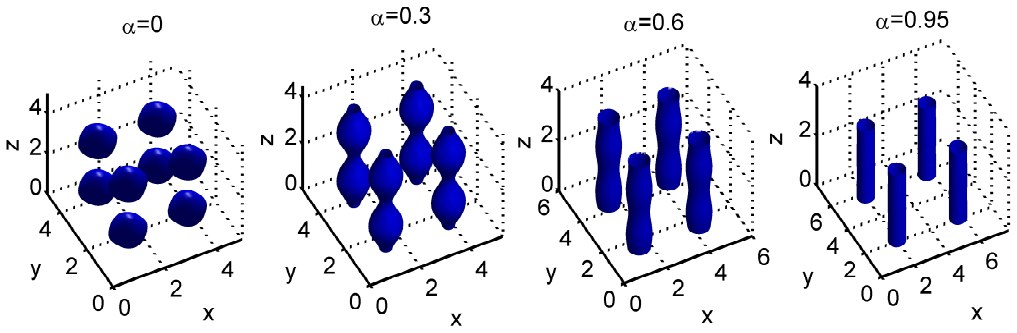

Figure 5.4: Energy density $\mathcal{E}$ of V+AV+V+AV solution, with $\mathcal{E} = 0.6 * \mathcal{E}_{\max}$, for $\alpha = 0, 0.3, 0.6, 0.95$.

Vortices that are aligned in the $z-$direction have a pair of winding numbers: one we call p corresponding to a winding of the fields in the $(x, y)-$plane at $z = c$ (independent of the constant c) and the other one, which we call q, corresponding to a winding in the $z-$direction. Generic vortices with such "charges" are dubbed "(p, q) − vortices". Moreover, a vortex with $q = 1$ and $p > 0$ we call a "$p-$vortex" (pV) and with $q = -1$ and $p < 0$ we call a "$p-$antivortex" (pAV). The fields of a $(p, q)-$vortex near its core (located along the $z-$axis) can be approximated as follows [1]:

$$\Phi_1 + i\Phi_2 \approx (x + iy)^p = e^{i\theta p} \qquad \Phi_3 + i\Phi_4 \approx e^{\frac{2\pi i q z}{L_z}} . \tag{5.13}$$

If we restrict ourselves to the plane $z = c$, where c is a constant, and we make a Hopf projection[2] of the fields Φ_β (corresponding to the limit $\alpha \to 1$) using $\psi^a = Z^\dagger \sigma_a Z$, where $Z \equiv (Z_1, Z_2)^T \equiv (\Phi_4 + i\Phi_3, -\Phi_2 + i\Phi_1)^T$ (see sec. 2.4.1), we end up with a map $\vec{\psi} : T^2 \to S^2$. The degree of this map corresponds to the integer p. Note that, since it is a Hopf-projected field, we must have $p = 0$ or, in the case of multi-vortices, $\sum_j p_j = 0$. In other words, multi-vortices can coexist as long as their $p-$charges add up to zero, which means that we must have an equal number of vortices and antivortices. The

[2]If we restrict to so-called "algebraically-inessential" fields (see [37]), then the classification of maps at $\alpha = 1$, $\psi : S^3 \to S^2$ (i.e. the Hopf charge) is still the single integer $Q \in \mathbb{Z}$, which is equal to the degree of Φ, so Q may denote either case.

$p-$charges, coupled with the twists q in the $z-$direction are the factors which give rise to the topological charge, given by the sum of the products of these charges for each vortex: $Q = \sum_j p_j q_j$. The fields Φ_β of a multi-vortex can be approximated by generalizing eq. (5.13) as follows:

$$\frac{U}{V} \equiv \frac{\Phi_3 + i\Phi_4}{\Phi_1 + i\Phi_2} = \sum_{j=1}^{d} \frac{e^{\frac{2\pi i q_j z}{L_z}}}{(w_j)^{p_j}}\,, \tag{5.14}$$

where d is the total number of vortices and antivortices and $w_j = (x - c_j^1) + i(y - c_j^2)$; $(x, y) = (c_j^1, c_j^2)$ corresponding to the location in the $(x, y)-$plane of the core of vortex j.

The $\alpha = 0.95$ field surfaces Φ_β are shown in Fig. 5.5, with $\Phi_\beta = 0.7$ shown in blue and $\Phi_\beta = -0.7$ shown in green, for $\beta = \{1, 2, 3, 4\}$. This allows us to easily determine the symmetry generators of the fields under certain rotations, translations, and reflections – listed in Table 5.3. Note that they correspond to the symmetries of a configuration consisting of two 1-vortices and two 1-antivortices (as can be easily seen by looking at Φ_4 from the $+z-$direction, with 2 blue surfaces and 2 green surfaces on the $(x, y)-$plane), and thus justifying the title for this section.

Table 5.3: Symmetry generators of the $\alpha = 0.95$ V+AV+V+AV solution, where $j = \{1, 2, 3\}$

Spatial Transformation	Isospin Transformation
$x_j \to x_j + L_j/2$	$(\Phi_j, \Phi_4) \to (-\Phi_j, -\Phi_4)$
$x_1 \to -x_1 + L_1/2$	$(\Phi_1, \Phi_2, \Phi_3, \Phi_4) \to (-\Phi_1, \Phi_2, \Phi_3, \Phi_4)$
$x_2 \to -x_2 + L_2/2$	$(\Phi_1, \Phi_2, \Phi_3, \Phi_4) \to (\Phi_1, -\Phi_2, \Phi_3, \Phi_4)$
$(x_1, x_2, x_3) \to (x_2, -x_1, x_3)$	$(\Phi_1, \Phi_2, \Phi_3, \Phi_4) \to (\Phi_2, \Phi_1, \Phi_3, -\Phi_4)$
$(x_1, x_2, x_3) \to (-x_1, x_2, x_3)$	$(\Phi_1, \Phi_2, \Phi_3, \Phi_4) \to (\Phi_1, \Phi_2, \Phi_3, -\Phi_4)$
$(x_1, x_2, x_3) \to (x_1, -x_2, x_3)$	$(\Phi_1, \Phi_2, \Phi_3, \Phi_4) \to (\Phi_1, \Phi_2, \Phi_3, -\Phi_4)$
$(x_1, x_2, x_3) \to (x_1, x_2, -x_3)$	$(\Phi_1, \Phi_2, \Phi_3, \Phi_4) \to (\Phi_1, \Phi_2, -\Phi_3, -\Phi_4)$

To end this section, we present an $\alpha-$dependent ansatz for the V+AV+V+AV solution. It was motivated by an ansatz, proposed by Prof. Ward, for the limiting case $\alpha \to 1$ — given by writing $\alpha = 1$ in the expressions below.

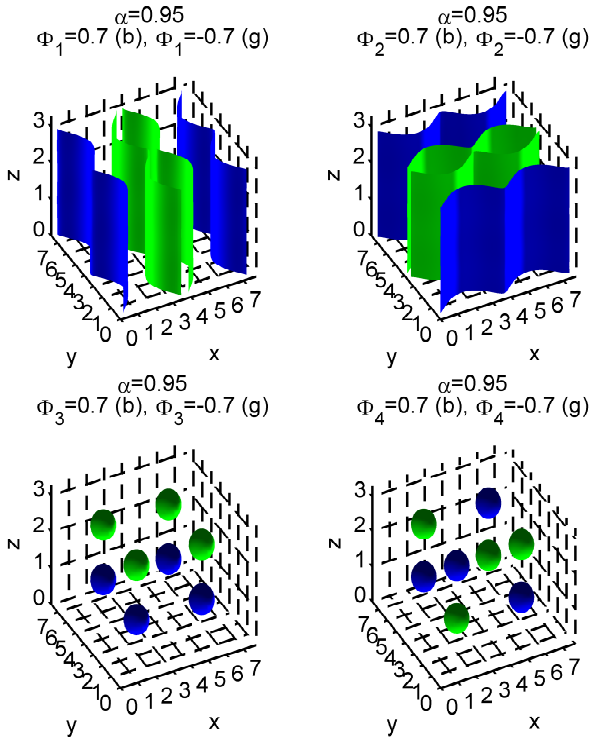

Figure 5.5: Fields $\Phi_\beta = 0.7$ (blue surfaces) and $\Phi_\beta = -0.7$ (green surfaces) of $\alpha = 0.95$ V+AV+V+AV solution, with $\beta = 1, 2, 3, 4$.

Our goal was to extend this to all values of α as follows:

$$\Phi_4 = c_1 c_2 c_3 \tag{5.15}$$

$$\Phi_1 = -s_1 \left(1 - \frac{s_2^2}{2} - (1-\alpha)\left(\frac{s_3^2}{2} - \frac{s_2^2 s_3^2}{3}\right)\right)^{\frac{1}{2}} \tag{5.16}$$

$$\Phi_2 = -s_2 \left(1 - \frac{s_1^2}{2} - (1-\alpha)\left(\frac{s_3^2}{2} - \frac{s_1^2 s_3^2}{3}\right)\right)^{\frac{1}{2}} \tag{5.17}$$

$$\Phi_3 = -s_3 \left(1 - \left(\frac{\alpha+1}{2}\right)(s_1^2 + s_2^2) + \left(\frac{1+2\alpha}{3}\right) s_1^2 s_2^2\right)^{\frac{1}{2}} , \tag{5.18}$$

where $s_i \equiv \sin(2\pi x_i/L_i)$ and $c_i \equiv \cos(2\pi x_i/L_i)$. Note that, in the Skyrme limit $\alpha = 0$, eqs. (5.15)-(5.18) reduce to the Skyrme crystal ansatz (2.97), (2.98). In order to see how close this ansatz is to the V+AV+V+AV solution, we have determined the optimal periods, minimal energies, and normalized energies for the ansatz at the α values previously mentioned for the V+AV+V+AV solution, except for $\alpha = 0.95$, which we have replaced with $\alpha = (0.9, 1)$. We also calculated the percent difference in the normalized energies between the ansatz and the V+AV+V+AV solution, given by $\%\Delta \equiv (E_{N\,\text{ansatz}} - E_{N,\text{V+AV+V+AV}})/E_{N\,\text{ansatz}}$, where $E_{N,\text{V+AV+V+AV}}$ was determined with the same lattice spacing and finite difference method as $E_{N\,\text{ansatz}}$; note that for $\alpha = 1$, $\%\Delta$ was calculated by using the $E_{N,\text{V+AV+V+AV}}$ for $\alpha = 0.95$. The minimal energies for each α were found by scanning through a range of periods, calculating the energy for each period through a first-order finite difference method, with lattice spacing $h = 0.1$, and picking the minimal ones, which we list in Table 5.4 along with the associated periods and $\%\Delta$. Note that the ansatz works particularly well for intermediate values of $\alpha \approx 0.3 - 0.6$. The corresponding energy densities $\mathcal{E}$ are plotted in Fig. 5.6, where $\mathcal{E}$ is 0.6 times the maximum value.

Table 5.4: Optimal periods, minimal energies, and normalized energies of V+AV+V+AV ansatz and its difference %Δ from V+AV+V+AV solution

α	$L_{x,y}$	L_z	E_{ansatz}	$E_{N\,\text{ansatz}}$	%Δ
0	4.7	4.7	4.2534	1.06 ± 0.01	0.03
0.3	4.9	4.2	4.1828	1.046 ± 0.002	0.02
0.6	5.2	3.8	4.0809	1.020 ± 0.005	0.01
0.9	5.6	3.2	3.8811	0.97 ± 0.01	0.04
1	5.7	2.8	3.8454	0.96 ± 0.01	0.05

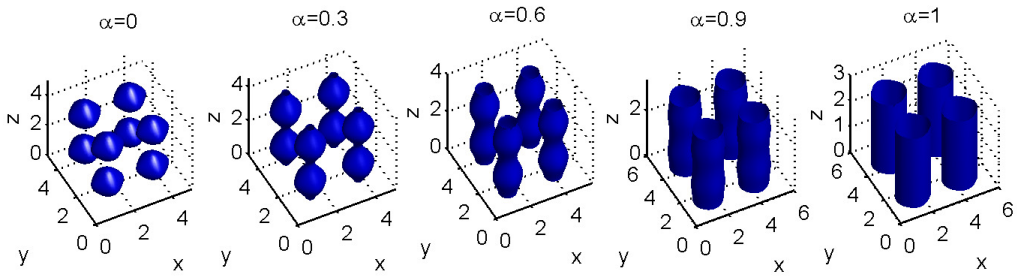

Figure 5.6: Energy density $\mathcal{E}$ of V+AV+V+AV ansatz, with $\mathcal{E} = 0.6 * \mathcal{E}_{\text{max}}$, for $\alpha = 0, 0.3, 0.6, 0.9, 1$.

5.3.2 The 2V+2AV solution

In trying to reproduce Prof. Ward's optimal period results for the multi-sheet solution, using its associated ansatz as an initial condition (see sec. 5.3.3 for details) and a parameter of generalized skyrme systems given by $\alpha = 0.95$, I accidentally discovered a local minimum in the energy, which features a pair of $|p| = 2$ vortices (see previous section for a discussion on the significance of p), which we call from now on 2-vortices (2V) for $p = +2$ and 2-antivortices (2AV) for $p = -2$. We now focused on investigating these solutions further by finding their optimal periods, as a function of α. Fig. 5.7 shows the energy density isosurfaces of the $\alpha = 0.6, 0.7, 0.8$, and 0.99 solutions – the reason we do not show the energy density isosurfaces for a lower value of α is because using the aforementioned ansatz for these values minimizes to the generalized skyrme crystal energy density isosurfaces of sec. 5.3.1. We have come to the conclusion that we stumbled upon this solution, rather than the multi-sheet solution, due to the sensitivity to the periods used as a starting

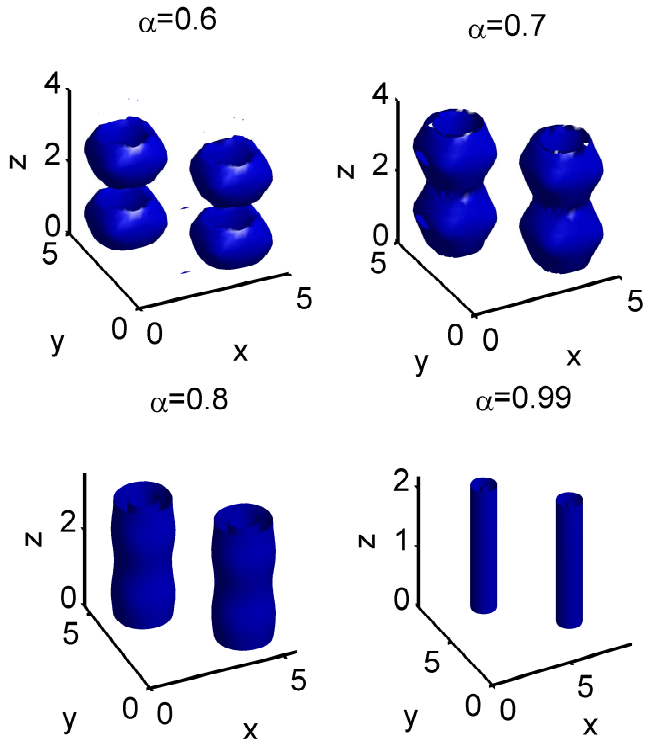

Figure 5.7: Energy density isosurfaces, with $\mathcal{E} = 0.8 * \mathcal{E}_{\max}$, of 2V+2AV solution for $\alpha = 0.6, 0.7, 0.8, 0.99$.

point ($L_{x,y,z} = 3$) in scanning through a range of periods in order to find the optimal one – it turns out that Prof. Ward and I used different initial periods. This hints to a vast number of triply-periodic solutions to the field equations of generalized skyrme systems, corresponding to different local minima in the energy.

Note from Fig. 5.7 that the isosurfaces become more homogeneous in the $z-$direction as α increases, becoming a 2-vortex and a 2-antivortex as $\alpha \to 1$. It is a simple exercise to determine the $|(p,q)|-$charges of a general configuration consisting of vortices and antivortices through a careful examination of its fields. See, for instance, Fig. 5.8, which shows the field isosurfaces $\Phi_\beta = 0.7$ (coloured blue) and $\Phi_\beta = -0.7$ (coloured green) with $\beta = \{1, 2, 3, 4\}$, for the 2V+2AV solution at $\alpha = 0.99$. One can "read off" the $|p|-$charge by looking at the Φ_1, Φ_2 isosurfaces and counting how many times one goes through the "blue-green" cycle around an imaginary circle

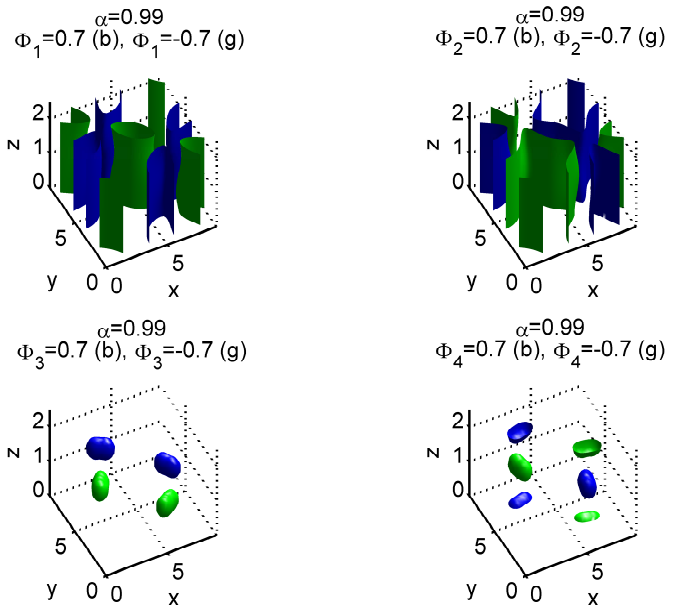

Figure 5.8: Field isosurfaces of the $\alpha = 0.99$ 2V+2AV solution with values $\Phi_\beta = 0.7$ (blue) and $\Phi_\beta = -0.7$ (green), where $\beta = 1, 2, 3, 4$.

centred at either of the vertices' cores ($(x, y) \approx (3, 7)$ and $(7, 3)$), yielding $|p_1| = |p_2| = 2$. Similarly, one can read off the $|q|-$ charge by looking at the Φ_3, Φ_4 isosurfaces and counting the "blue-green" cycles over one period in the $z-$direction at the location of the vortex cores, yielding $|q_1| = |q_2| = 1$. Unfortunately, one cannot determine the signs of (p, q) – this can be determined, for example, by mapping the vortex fields to vector fields and looking at their relative orientations. One can also analyze the $(p, q)-$charges numerically (including relative signs), which we have done as well. However, a discussion of this will be relegated to Chapter 6, where we delve into the topic of "Generalized Vortices". Field isosurfaces are also useful in investigating their symmetries – Table 5.5 shows a list of the 2V+2AV symmetry generators.

Table 5.5: Symmetry generators of the $\alpha = 0.99$ 2V+2AV solution

Spatial Transformation	Isospin Transformation
$(x_1, x_2, x_3) \to (-x_1, -x_2, x_3)$	$(\Phi_1, \Phi_2, \Phi_3, \Phi_4) \to (\Phi_1, -\Phi_2, \Phi_3, -\Phi_4)$
$(x_1, x_2, x_3) \to (-x_2, -x_1, x_3)$	$(\Phi_1, \Phi_2, \Phi_3, \Phi_4) \to (\Phi_1, -\Phi_2, \Phi_3, \Phi_4)$
$(x_1, x_2, x_3) \to (x_1, x_2, -x_3)$	$(\Phi_1, \Phi_2, \Phi_3, \Phi_4) \to (\Phi_1, \Phi_2, -\Phi_3, \Phi_4)$

We now turn to the analysis of the optimal periods of the 2V+2AV solution, as a function of α. The procedure used was to first vary $L_{x,y}$ whilst keeping L_z constant, scanning the (minimized) energies in the process. We then pick the period that produces the lowest energy and keep it constant while this time varying L_z and finding the one with minimal energy. For the $\alpha = 0.9, 0.95$ cases, the periods $L_{x,y}$ and L_z were varied by keeping $n_{x,y}$ and n_z constant and changing $h_{x,y}$ and h_z, respectively. This was done to keep the minimization from breaking down, as it tends to become unstable for α close to 1. For the other α cases, the periods $L_{x,y}$ and L_z were generally varied by keeping h constant and varying the number of lattice points $n_{x,y}$ and n_z, respectively, with steps of $\Delta n = 3$. These were usually increased to find the optimal periods. To do this, we made a copy of the fields at the lattice points along the edges of the fundamental cell and added them along each direction in order to produce two exact surfaces of lattice points: the edge and the one immediately preceding the edge.

Table 5.6 lists the optimal periods, the associated energies E and normalized energies $E_N \equiv E/4$, for the 2V+2AV configuration with different α values – the normalized energies and corresponding periods are plotted as functions of α in Fig. 5.9 and Fig. 5.10, respectively. The quoted values of energy E were determined by using a second-order finite difference method, with $h = 0.2$. Therefore, the periods are associated with even-numbered $n_{x,y}$ and n_z values[3]. The quoted normalized energy errors in Table 5.6 were obtained by taking the difference between the associated second-order charges and $Q = 4$, then dividing by 4. Note that we scanned through the different periods for each α in big steps ($\Delta L = 0.6$). In order to get a better idea of where the "true" optimal periods lie (in between these steps), we have fitted a second-order polynomial to the three lowest-energy periods, for each α, and determined

[3]Note that the relatively large lattice spacing produces $L_{x,y}$ and L_z vs. α curves that are not as smooth as the ones for other solutions that we present (with lower lattice spacing); the periods do, however, clearly show different behaviours as functions of α, which is what we are interested in presenting.

its minimum value. These minima correspond to the periods quoted in Table 5.7. Note that these values are just meant to give a rough idea of where one might start looking for the "actual" optimal periods, if one is interested in precision. For example, a period listed in Table 5.6 could be used as the upper limit (if the corresponding period listed in Table 5.7 is smaller) or the lower limit (if the period in Table 5.7 larger) of a list of periods that one could scan through.

Note that there is a jump in the optimal periods, as a function of α, in the range $\alpha = 0.4 - 0.6$. Even though we do not know the reason for this feature, it is worth pointing out that there is a transition taking place in the solutions for these values of α, since their energy density isosurfaces look qualitatively different. For $\alpha = 0.4$, these look like the V+AV+V+AV solution from sec. 5.3.1, and for $\alpha = 0.5$, they look more like a 2V+2AV solution. In other words, if one keeps the initial periods fixed, the possible solutions that one obtains depends on the value of α, with a preference towards V+AV+V+AV-like solutions for $\alpha \leq 0.4$ and 2V+2AV-like solutions for $\alpha \geq 0.5$.

Table 5.6: Optimal periods, minimal energies, and normalized energies $E_N \equiv E/4$ of 2V+2AV solution

α	$L_{x,y}$	L_z	E	E_N
0	4.4	4.4	4.1568	1.039 ± 0.004
0.1	4.4	4.4	4.1568	1.039 ± 0.004
0.2	4.4	4.0	4.1610	1.040 ± 0.004
0.3	4.8	4.0	4.1352	1.034 ± 0.004
0.4	4.8	3.6	4.13	1.033 ± 0.005
0.5	4.4	4.0	4.0792	1.020 ± 0.004
0.6	4.8	3.6	3.9779	0.995 ± 0.004
0.7	4.8	3.6	3.8420	0.961 ± 0.004
0.8	5.2	3.2	3.6463	0.912 ± 0.005
0.9	7.2	2.8	3.3899	0.848 ± 0.008
0.95	8.0	2.6	3.1731	0.793 ± 0.008
0.97	8.0	2.4	3.0673	0.767 ± 0.009
0.99	8.8	2.2	2.9439	0.74 ± 0.01

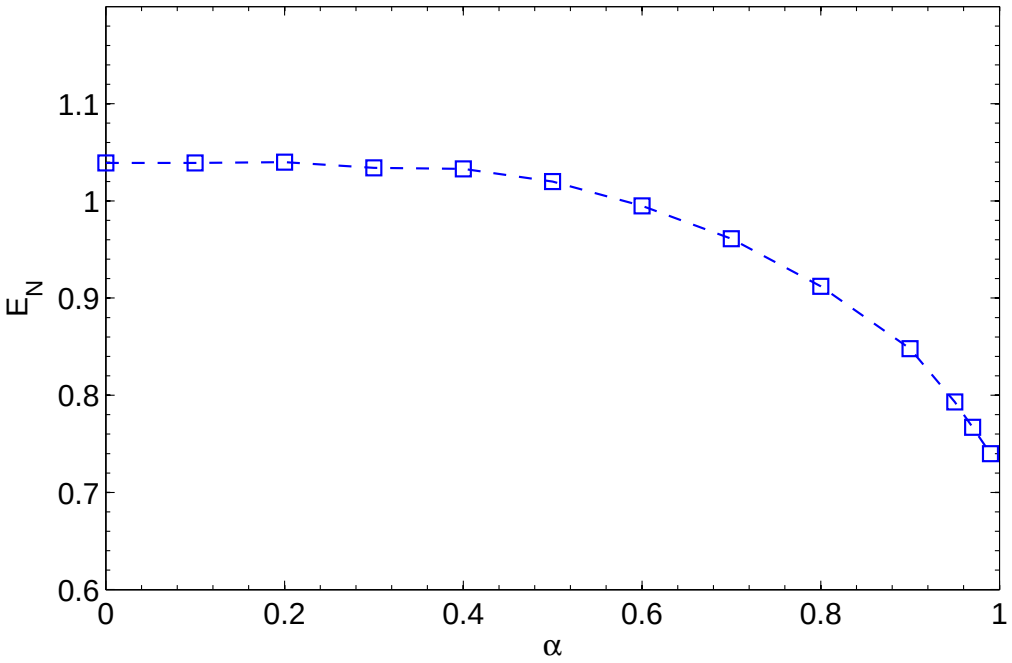

Figure 5.9: 2V+2AV normalized energy, as a function of the parameter α.

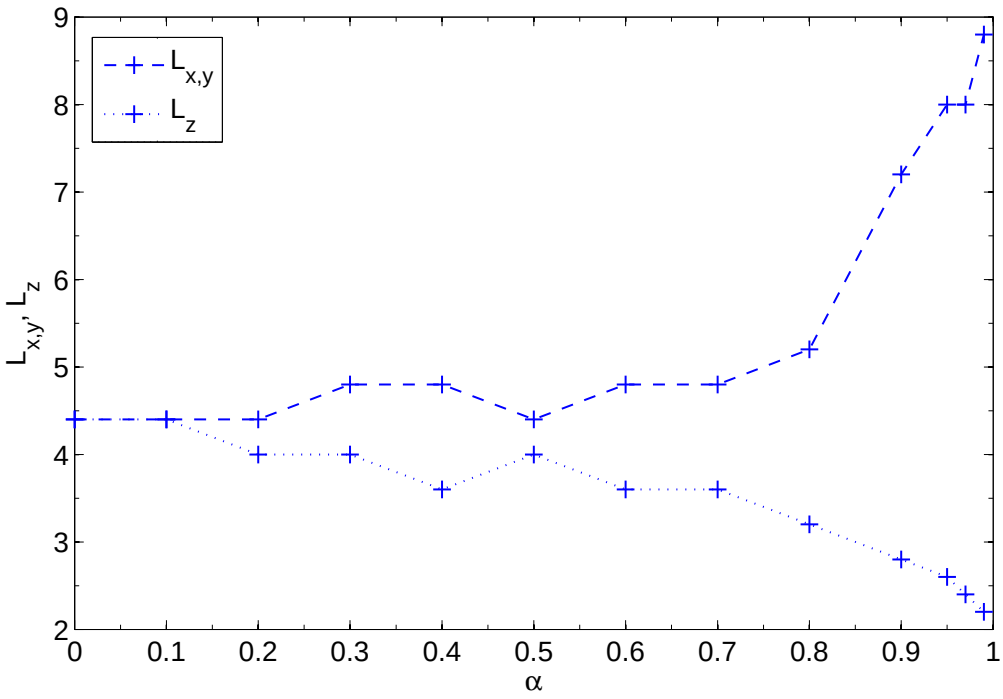

Figure 5.10: 2V+2AV optimal periods $L_{x,y}$ and L_z, as a function of the parameter α.

Table 5.7: Interpolated optimal periods of 2V+2AV solution

α	$L_{x,y}$	L_z
0	4.30	4.63
0.1	4.47	4.37
0.2	4.60	4.20
0.3	4.68	4.10
0.4	5.02	3.93
0.5	4.29	4.14
0.6	4.55	3.77
0.7	4.74	3.46
0.8	5.14	3.21
0.9	7.43	2.80
0.95	7.95	2.60
0.97	8.04	2.40
0.99	8.71	2.18

5.3.3 The multi-sheet solution

While working with Vortex-AntiVortex (V+AV) pairs (see next chapter) in the range $0 < \alpha < 1$, we noticed a peculiar configuration with 2 holes facing in the $x-$direction as well as in the $y-$direction. This configuration was noticed at $\alpha = 0.5$, after stacking two copies of optimal L_z-valued, merged V+AV pairs, in the $z-$direction and introducing a perturbation by translating the top copy by a distance of $D = 0.5$ with respect to the bottom copy, and then minimizing to obtain Fig. 5.11. Prof. Ward used a similar-looking configuration, at $\alpha = 0.8$, as the initial condition to look for its optimal periods in the $x-, y-$, and $z-$directions. In the process, a new periodic structure was seen to emerge, with an E/Q value lower than any of the other configurations previously seen. However, producing this new periodic structure turned out to be a very convoluted process. This was one of the motivations in looking for an ansatz that approximates the fields of the new periodic solution, which we now call the "multi-sheet solution". This ansatz was conceived by Ward and is given by:

$$\begin{aligned} \Phi_1 &= \cos\left(\frac{2\pi y}{L_y}\right)\sin\left(\frac{2\pi z}{L_z}\right), \quad \Phi_2 = \sin\left(\frac{2\pi y}{L_y}\right)\left|\sin\left(\frac{2\pi z}{L_z}\right)\right| \\ \Phi_3 &= \sin\left(\frac{2\pi x}{L_x}\right)\left|\cos\left(\frac{2\pi z}{L_z}\right)\right|, \quad \Phi_4 = \cos\left(\frac{2\pi x}{L_x}\right)\cos\left(\frac{2\pi z}{L_z}\right). \end{aligned} \tag{5.19}$$

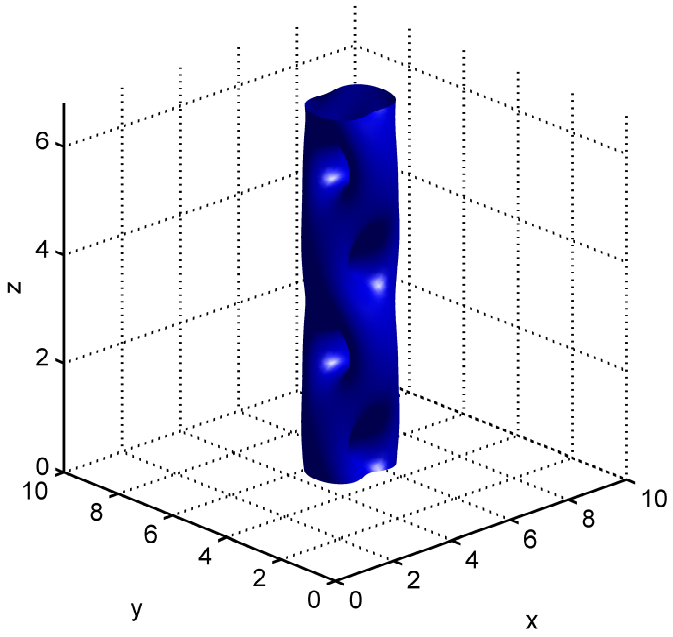

Figure 5.11: Energy density isosurface, with $\mathcal{E} = 0.5 * \mathcal{E}_{\max}$, of an $\alpha = 0.5$ V+AV 2-stack solution, with $Q = 4$ and $E/Q = 1.0658 \pm 0.0003$.

It should be noted that omitting the absolute value signs in the expressions for the fields Φ_2 and Φ_3 would cause them to cancel in such a way over the course of one period to produce a configuration with zero charge; including them produces the desired charge of $Q = 4$.

Expressions (5.19) were used as the initial condition for the conjugate-gradient method of energy minimization, for several different values of α in the range[4] $\alpha = 0.6$ to $\alpha = 0.99$. Again, the goal here is to find the optimal periods of the multi-sheet solution.

For this section, we have used a second order finite-difference scheme for both E and Q, with a lattice spacing of $h = 0.1$. The procedure used in finding the optimal periods is similar to the one used for the 2V+2AV solution from sec. 5.3.2. The only exception to this procedure is for the $\alpha = 0.95, 0.98,$ and 0.99 cases where the L_z values are reduced in order to find their optimal

[4]The reason we did not investigate the solutions for $\alpha < 0.6$ was that, through discussions with Prof. Ward, we had learnt that the energy of the multi-sheet solution for this region is seemingly not any lower than the V+AV+V+AV solution and, therefore, was deemed not important enough to investigate further.

values since starting from low L_z values causes the configuration to become unstable as it is being minimized. We also noticed that reducing L_z by subtracting n_z (i.e. deleting the top and bottom faces in the $z-$direction) causes a significant decrease in the charge. Therefore, we decided to lower L_z by decreasing h_z, while keeping n_z constant. Table 5.8 lists the optimal $L_{x,y}$ and L_z values, along with the minimal energies E and the normalized energies $E_N \equiv E/4$. The errors in the normalized energies were obtained by calculating the difference of the charge obtained using a second-order finite difference scheme with $Q = 4$, then dividing by 4.

Table 5.8: Optimal periods, minimal energies, and normalized energies of multi-sheet solution

α	$L_{x,y}$	L_z	E	E_N
0.6	4.0	5.0	4.0304	1.0076 ± 0.0003
0.7	3.8	5.4	3.8978	0.9745 ± 0.0003
0.75	3.6	5.6	3.8046	0.9512 ± 0.0003
0.8	3.4	6.0	3.6836	0.9209 ± 0.0004
0.85	3.2	6.4	3.5247	0.8812 ± 0.0005
0.9	3.0	7.0	3.3096	0.8274 ± 0.0005
0.95	2.6	7.8	2.9968	0.7492 ± 0.0008
0.98	2.0	8.4	2.7030	0.6758 ± 0.001
0.99	1.8	8.8	2.5583	0.6396 ± 0.002

Note that, since we have used a second-order finite-difference method here, n_x, n_y, and n_z must be even-valued, so as we varied the n values, the periods varied by 0.2. Therefore, as in the previous section, in order to get a better idea of where the optimal periods lie, we fit a second-order function to the minimal $L_{x,y}$ and L_z values listed in Table 5.8, as well as two other data points to either side of these minima, and calculated the minimum of the fit to find the interpolated values of the optimal periods as well as the associated values of the energy, all of which are listed in Table 5.9. As before, these values are meant to give a better idea of where the optimal values lie, rather than give a precise value of the actual optimal periods.

Fig. 5.12 shows the energy density isosurfaces where $\mathcal{E} = 0.8$ times its maximum value for $\alpha = 0.6, 0.8, 0.9, 0.99$, using the corresponding optimal periods

Table 5.9: Interpolated optimal periods, minimal energies, and normalized energies of multi-sheet solution

α	$L_{x,y}$	L_z	E	E_N
0.6	4.058	4.967	4.0301	1.0075 ± 0.0003
0.7	3.803	5.425	3.8978	0.9745 ± 0.0003
0.75	3.598	5.688	3.8043	0.9511 ± 0.0003
0.8	3.461	6.019	3.6831	0.9208 ± 0.0004
0.85	3.223	6.443	3.5246	0.8812 ± 0.0005
0.9	2.945	7.046	3.3095	0.8274 ± 0.0005
0.95	2.561	7.835	2.9966	0.7492 ± 0.0008
0.98	2.071	8.38	2.7021	0.6755 ± 0.001
0.99	1.738	8.833	2.5577	0.6394 ± 0.002

of Table 5.8. Note that at $\alpha = 0.6$, the solution resembles a deformed version of the V+AV+V+AV solution, but as α is increased, it transforms into a series of parallel sheets orthogonal to the $z-$direction and with some $x-$ and $y-$ dependence at $\alpha = 0.8, 0.9$, but homogeneous at $\alpha = 0.99$.

Fig. 5.13 shows the energy density as a function of z for the $\alpha = 0.99$ solution, which we singled out since it has the lowest energy-per-charge of any of the solutions we have encountered so far. It clearly shows the location of the sheets – corresponding to the peaks in the energy density curve. The curve was obtained by integrating the energy density of the minimized solution along the $x-$ and $y-$directions, which is numerically equivalent to taking the average of the energy density at each lattice site along these directions, leaving an energy density which is just a function of z.

Finally, as in the previous section, to investigate the symmetries of the multi-sheet solution we look at its fields. More specifically, we investigate the isosurfaces where $\Phi_\beta = \pm 0.8$, for the $\alpha = 0.99$ solution. Fig. 5.14 shows Φ_β, where $\beta = \{1, 2, 3, 4\}$, where the blue surfaces correspond to $\Phi_\beta = 0.8$ and the green surfaces correspond to $\Phi_\beta = -0.8$.

It is not hard to conclude, by looking at the field isosurfaces in Fig. 5.14, that the transformations listed in Table 5.10, corresponding to translations, rotations, and reflections, are the symmetry generators of the $\alpha = 0.99$ multi-sheet solution.

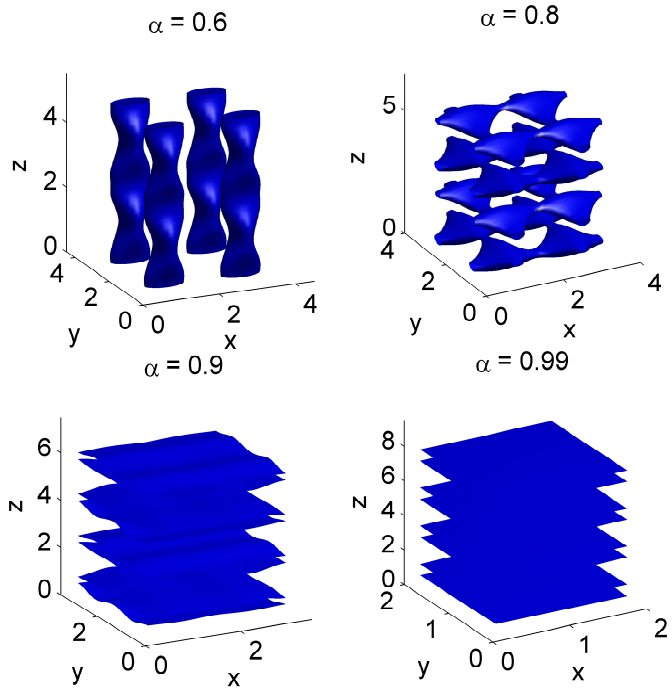

Figure 5.12: Energy density isosurfaces of multi-sheet solution for $\alpha = 0.6, 0.8, 0.9, 0.99$, where $\mathcal{E} = 0.8 * \mathcal{E}_{\max}$.

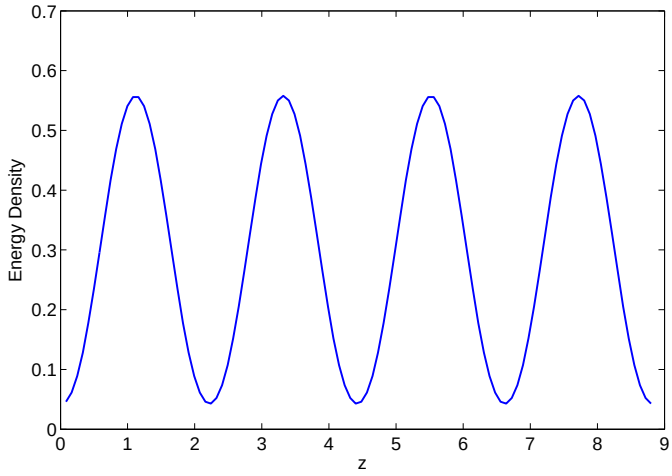

Figure 5.13: Energy density as a function of z for $\alpha = 0.99$ multi-sheet solution.

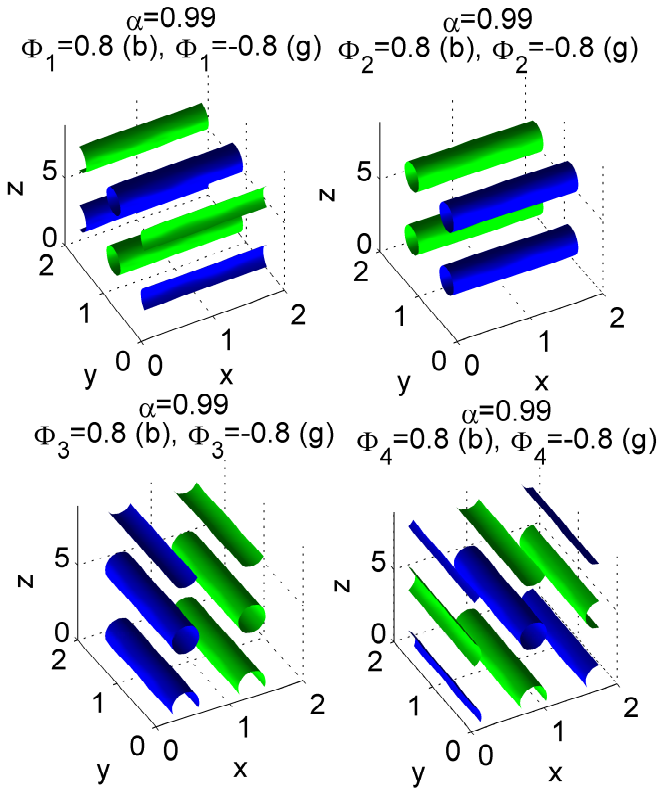

Figure 5.14: Field isosurfaces of multi-sheet solution with values $\Phi_\beta = 0.8$ (blue) and $\Phi_\beta = -0.8$ (green), where $\beta = 1, 2, 3, 4$.

Table 5.10: Symmetry generators of the $\alpha = 0.99$ multi-sheet solution

Spatial Transformation	Isospin Transformation
$(x_1, x_2, x_3) \to (x_1 + L_1/2, x_2, x_3)$	$(\Phi_1, \Phi_2, \Phi_3, \Phi_4) \to (\Phi_1, \Phi_2, -\Phi_3, -\Phi_4)$
$(x_1, x_2, x_3) \to (x_1, x_2 + L_2/2, x_3)$	$(\Phi_1, \Phi_2, \Phi_3, \Phi_4) \to (-\Phi_1, -\Phi_2, \Phi_3, \Phi_4)$
$(x_1, x_2, x_3) \to (x_1, x_2, x_3 + L_3/2)$	$(\Phi_1, \Phi_2, \Phi_3, \Phi_4) \to (-\Phi_1, \Phi_2, \Phi_3, -\Phi_4)$
$(x_1, x_2, x_3) \to (x_2, -x_1, x_3 - L_3/4)$	$(\Phi_1, \Phi_2, \Phi_3, \Phi_4) \to (-\Phi_4, -\Phi_3, \Phi_2, \Phi_1)$
$(x_1, x_2, x_3) \to (-x_1, x_2, x_3)$	$(\Phi_1, \Phi_2, \Phi_3, \Phi_4) \to (\Phi_1, \Phi_2, -\Phi_3, \Phi_4)$
$(x_1, x_2, x_3) \to (x_1, -x_2, x_3)$	$(\Phi_1, \Phi_2, \Phi_3, \Phi_4) \to (\Phi_1, -\Phi_2, \Phi_3, \Phi_4)$
$(x_1, x_2, x_3) \to (x_1, x_2, -x_3)$	$(\Phi_1, \Phi_2, \Phi_3, \Phi_4) \to (-\Phi_1, \Phi_2, \Phi_3, \Phi_4)$

5.3.4 The multi-sheet ansatz

A more graceful way of writing the multi-sheet ansatz, introduced in (5.19) in the previous section, was shown in [1]. It is given by:

$$Z_1 := \Phi_1 + i\Phi_2 = \sin(f) e^{i\gamma_2 by}\,, \tag{5.20}$$

$$Z_2 := \Phi_3 + i\Phi_4 = \cos(f) e^{i\gamma_1 ax}\,, \tag{5.21}$$

where (a, b) are real numbers, which we take to be $(a, b) = (2\pi/L_x, 2\pi/L_y)$, $(\gamma_1, \gamma_2) = (\pm 1, \pm 1)$, and $f = f(z)$ is a real function with the following values: $f(0) = 0$, $f(L_z/4) = \pi/2$, $f(L_z/2) = \pi$, $f(3L_z/4) = 3\pi/2$, $f(L_z) = 2\pi$. Note that, in order for the fields to be continuous and for the charge to be non-zero, one has to flip the sign of the fields in a certain way, as a function of z. In particular, we choose the following configuration:

$$(\gamma_1, \gamma_2) = \begin{cases} (1,1) & \text{for } z \in [0, L_z/4)\,, \\ (-1,1) & \text{for } z \in [L_z/4, L_z/2)\,, \\ (-1,-1) & \text{for } z \in [L_z/2, 3L_z/4)\,, \\ (1,-1) & \text{for } z \in [3L_z/4, L_z)\,, \end{cases}$$

which is analogous to using the absolute value signs in the form of the ansatz given in eq. (5.19).

Looking at (5.20) and (5.21), one can see that a translation in either the $x-$direction ($x \mapsto x + c$) or the $y-$direction ($y \mapsto y + c$) would leave half

of the fields invariant. Such transformations, in that order, when acting on fields $Z \equiv (Z_1, Z_2)^T$, can be represented as follows:

$$\begin{pmatrix} 1 & 0 \\ 0 & e^{iac} \end{pmatrix} \qquad \text{or} \qquad \begin{pmatrix} e^{ibc} & 0 \\ 0 & 1 \end{pmatrix} . \tag{5.22}$$

The suggestive form of the transformations (5.22) makes it apparent that they correspond to a subgroup of $\mathrm{U}(2)$, which corresponds to the symmetry group of the one-parameter family of generalized Skyrme systems.

This allows us to invoke the "Principle of Symmetric Criticality" [10], which states that, for a certain field configuration which is: (i) invariant under elements of a subset of the full symmetry group of the theory, and (ii) a stationary point of the reduced action of the theory (corresponding to the action, restricted to such field configurations); such a field configuration is automatically a stationary point of the full action.

What this means is that, generally, whenever one has fields that have property (i), the action reduces to a simpler, lower-dimensional one, and due to the principle of symmetric criticality, one can claim that its stationary points are also the ones for the full theory.

In our case, what this practically means is that the expression for the generalized energy density (2.26), using the fields (5.20) and (5.21), will reduce to one which depends only on $f(z)$ and df/dz. In particular, it can be put in the following form:

$$E[f] = \int \left(A(f)(f')^2 + B(f) \right) dz \tag{5.23}$$

$$= \int \left(\sqrt{A} f' \pm \sqrt{B} \right)^2 dz \mp 2 \int \sqrt{AB}\, df \,, \tag{5.24}$$

where $f' = df/dz$. The associated Bogomolny bound and Bogomolny equa-

tion is given by:

$$E[f] \geq 2\int \sqrt{AB}\, df\,, \tag{5.25}$$

$$f' = \sqrt{B/A}\,. \tag{5.26}$$

The Principle of Symmetric Criticality guarantees that the fields which minimize the energy (5.23) (or the ones which saturate the Bogomolny bound (5.25)) are also fields which minimize the full energy, which in our case is given by integrating the energy density (2.26).

After substituting the fields (5.20) and (5.21) into the energy (2.26), we get the following expressions for the energy density:

$$\mathcal{E}_2 = \kappa_2[a^2\cos^2(f) + b^2\sin^2(f) + (f')^2 - \alpha(a^2\cos^4(f) + b^2\sin^4(f))]\,, \tag{5.27}$$

$$\begin{aligned}\mathcal{E}_4 = \kappa_4[&(1-\alpha)((f')^2b^2\sin^2(f) + (f')^2a^2\cos^2(f) + (a^2b^2\sin^2(2f))/4) \\ &+ (\alpha/4)((f')^2(a^2+b^2)\sin^2(2f))]\,,\end{aligned} \tag{5.28}$$

where $\kappa_2 = 1/4\pi^2(3-\alpha)$ and $\kappa_4 = 1/4\pi^2(3-2\alpha)$, as before.

Putting these expressions into the form (5.23), we find the following values:

$$\begin{aligned}A = L_xL_y[&\kappa_2 + \kappa_4((1-\alpha)(b^2\sin^2(f) + a^2\cos^2(f)) \\ &+ (\alpha/4)(a^2+b^2)\sin^2(2f))]\,,\end{aligned} \tag{5.29}$$

$$\begin{aligned}B = L_xL_y[&\kappa_2(a^2\cos^2(f) + b^2\sin^2(f) - \alpha(a^2\cos^4(f) + b^2\sin^4(f))) \\ &+ (\kappa_4/4)(1-\alpha)(a^2b^2\sin^2(2f))]\,.\end{aligned} \tag{5.30}$$

Through our numerical investigations, we have concluded that the preferred state is for $L_x = L_y$, so we can set $a = b$, which simplifies these expressions considerably. With this in mind, we now wish to solve the differential

equation (5.26), which can be done through separation of variables:

$$L_z(\alpha, a) = 4\sqrt{2}\int_0^{\pi/2} \sqrt{\frac{2\kappa_2 + \kappa_4 a^2[2(1-\alpha) + \alpha\sin^2(2f)]}{\kappa_2 a^2[4(1-\alpha) + 2\alpha\sin^2(2f)] + \kappa_4 a^4(1-\alpha)\sin^2(2f)}}\, df\,. \tag{5.31}$$

Note that on the limits, the integrand becomes:

$$\sqrt{\frac{\kappa_2 + \kappa_4 a^2(1-\alpha)}{2\kappa_2 a^2(1-\alpha)}}\,,$$

which is convergent in the range $0 \leq \alpha < 1$ and divergent for $\alpha = 1$. This implies that, for $\alpha \in [0, 1)$, the bound (5.25) can be saturated and there is an associated, minimal, $L_{z,\min}$. On the other hand, when $\alpha = 1$, the bound cannot be saturated and the energy can be made arbitrarily small by increasing L_z (or decreasing $L_x = L_y$, as one can see (with a bit of effort) from $E(\alpha, a)$ below).

The associated expression for the energy (with $a = b$) is given by:

$$\begin{aligned} E(\alpha, a) = 2L_x^2 \int_0^{\pi/2} \Big[\big(4\kappa_2 + \kappa_4 a^2[4(1-\alpha) + 2\alpha\sin^2(2f)]\big) \\ \times \big(\kappa_2 a^2[4(1-\alpha) + 2\alpha\sin^2(2f)] + \kappa_4 a^4(1-\alpha)\sin^2(2f)\big) \Big]^{\frac{1}{2}} df\,. \end{aligned} \tag{5.32}$$

The integrals (5.31) and (5.32) can be evaluated numerically. We calculated $E(\alpha, a)$ for several different values of (α, a), where $\alpha \in [0.6, 0.99]$ and found that there is indeed a minimal energy value associated with a certain value of $a \equiv a_{\min}$, for each α, which we call $E_{\min} \equiv E(\alpha, a_{\min})$. We then evaluated $L_z(\alpha, a_{\min}) \equiv L_{z,\min}$, for each α. Table 5.11 lists the values of $L_{x,y,\min} \equiv 2\pi/a_{\min}$, $L_{z,\min}$, $E_{\min}$, and $E_N \equiv E_{\min}/4$ obtained in this way, for each α.

Fig. 5.15 shows the energy density of the multi-sheet ansatz as a function

Table 5.11: Optimal periods and minimal energies of multi-sheet ansatz

α	$L_{x,y,\min}$	$L_{z,\min}$	$E_{\min}$	E_N
0.6	3.4	7.4704	4.6501	1.1625
0.7	3.3	7.8368	4.3536	1.0884
0.75	3.2	8.0198	4.1759	1.0440
0.8	3.1	8.2665	3.9713	0.9928
0.85	3.0	8.6162	3.7303	0.9326
0.9	2.8	8.9895	3.4364	0.8591
0.95	2.4	9.3970	3.0507	0.7627
0.98	2.0	9.8947	2.7193	0.6798
0.99	1.7	10.0661	2.5618	0.6404

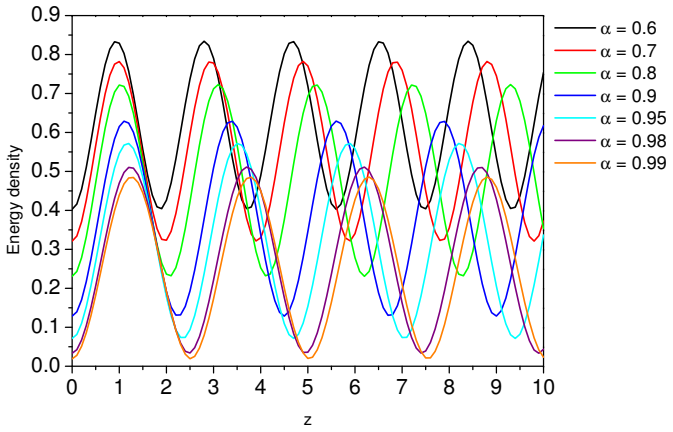

Figure 5.15: Energy density plots as functions of z, for $\alpha = 0.6$ to $\alpha = 0.99$, of multi-sheet ansatz.

of z, for different α values. Note that, as α increases, the sheets become increasingly localized.

In Fig. 5.16, we compare the plots of the normalized energy E_N as a function of α for the minimized fields, obtained through the conjugate gradient method, and for the ansatz. We also compare their optimal periods $L_{x,y,\min}$ and $L_{z,\min}$ as a function of α in Fig. 5.17.

Finally, as a way of summing up the work described in this section, Fig. 5.18 shows the normalized energies of the V+AV+V+AV, 2V+2AV, and multi-sheet solutions, as functions of α. This clearly shows how the multi-sheet solution ends up being the one with lowest energy E_N as $\alpha \to 1$.

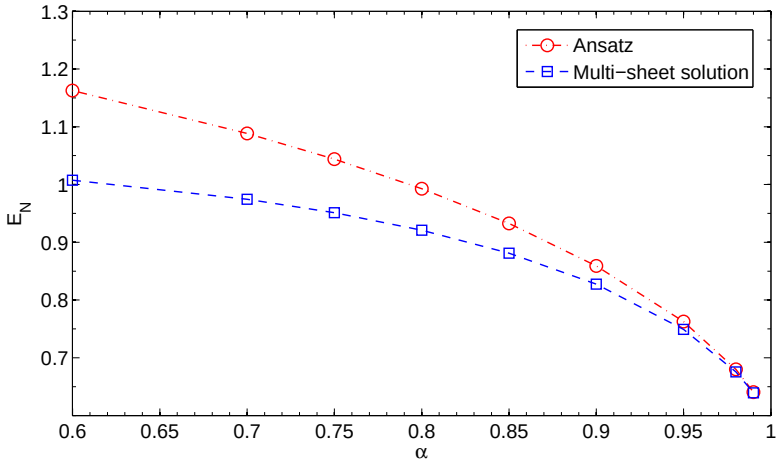

Figure 5.16: Normalized energy of multi-sheet solution and of ansatz, as a function of α.

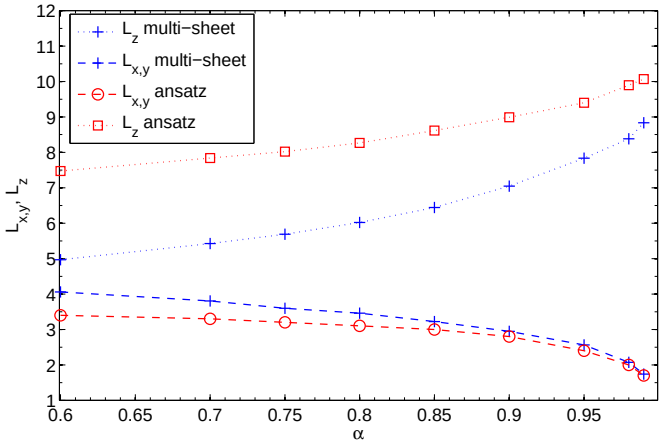

Figure 5.17: Optimal periods $L_{x,y}$ and L_z of multi-sheet solution and of ansatz as a function of the parameter α.

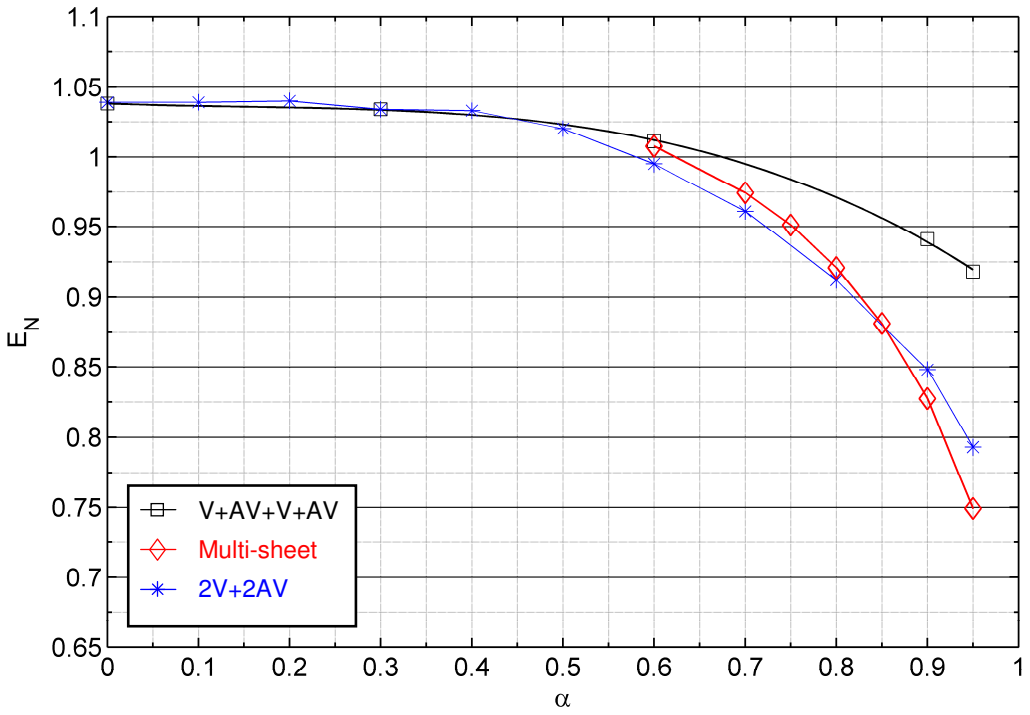

Figure 5.18: Normalized energy of V+AV+V+AV, 2V+2AV, and multi-sheet solutions, as functions of α.

Chapter 6

Generalized vortices

The investigation of vortices in generalized skyrme systems was originally motivated by the solution observed when taking the Skyrme crystal to the $\alpha \to 1$ limit, resulting in a configuration consisting of 2 vortices and 2 antivortices (see sec. 5.3.1). This prompted us to study two different types of configurations: a vortex and an antivortex (V+AV) in sec. 6.1 and a pair of both vortices and antivortices (V+AV+V+AV) in sec. 6.2. The main difference between the solutions presented in this chapter and those presented in the previous chapter is that here we study vortex solutions in their own right and not as the result of certain processes under certain initial conditions, such as starting with the Skyrme crystal and then varying α (obtaining the V+AV+V+AV solution from sec. 5.3.1 in the process), or starting with the multi-sheet ansatz for certain periods at certain α values (obtaining the 2V+2AV solution from sec. 5.3.2 in the process). That is, we now use a multi-vortex ansatz (introduced in sec. 5.3.1) or an alternative "product ansatz" (introduced shortly) as an initial condition and we take the periods in the $x-$ and $y-$directions to be large and fixed at $L_{x,y} = 10$. In terms of the $x-$ and $y-$dependent vortex fields, if one introduces a factor that increases exponentially with the distance from the vortex cores, these large $L_{x,y}$ periods would simulate isolated vortices in our triply-periodic lattice

(assuming they are located near the centre of the fundamental cell), as these fields would approach their asymptotic values exponentially quickly.

After introducing the product ansatz, in sec. 6.1.1 we present an analytical calculation which determines the energy of a vortex-antivortex configuration as a function of inter-vortex separation, in the context of generalized skyrme systems. Afterwards, we show the results of some numerical investigations that were carried out to provide a description of inter-vortex forces, where $\alpha \geq 0$. Then, in sec. 6.1.2, we show a variety of V+AV N-stack solutions (i.e. V+AV configurations stacked N times in the $z-$direction), for different values of α. We shall see that braided structures emerge for certain values of α and N, motivating a "Braided V+AV Ansatz", which we present in sec. 6.1.3, leading to a discussion of its usefulness in numerically calculating the $(p,q)-$charges of V+AV configurations. Finally, in sec. 6.2, we present solutions of V+AV+V+AV configurations for different values of α and N.

6.1 V+AV

We start by introducing an ansatz, called the "product ansatz" [8], that we shall be using throughout most of this section as an initial condition for the numerical minimization of multi-vortex fields. It consists of using a matrix U_j for vortex j, given by:

$$U_j = \begin{pmatrix} \Phi_{4,j} + i\Phi_{3,j} & \Phi_{2,j} + i\Phi_{1,j} \\ -\Phi_{2,j} + i\Phi_{1,j} & \Phi_{4,j} - i\Phi_{3,j} \end{pmatrix} , \tag{6.1}$$

where, for this section, $j = \{1, 2\}$ as we only deal with a vortex-antivortex pair. The fields $\Phi_{\beta,j}$ are given by:

$$\Phi_{1,j} + i\Phi_{2,j} = (w_j)^{p_j} e^{\Lambda\rho_j} , \tag{6.2}$$

$$\Phi_{3,j} + i\Phi_{4,j} = e^{i\beta q_j z} , \tag{6.3}$$

where $\beta = 2\pi/L_z$, Λ is a constant which determines how quickly $\Phi_{1,j}$ and $\Phi_{2,j}$ reach their asymptotic values (we take $\Lambda = L_{x,y} = 10$), (p_j, q_j) are the $(p,q)-$charges of vortex j (see sec. 5.3.1 for details), $w_j = (x - c_j^1) + i(y - c_j^2)$, with the core of vortex j at $(x,y) = (c_j^1, c_j^2)$, and $\rho_j = \sqrt{(x-c_j^1)^2 + (y-c_j^2)^2}$.

The product ansatz then consists of multiplying the U matrices for the various vortices and obtaining their product, called U, consisting of fields Φ_β:

$$U = U_1 \cdot U_2 \cdots U_d = \begin{pmatrix} \Phi_4 + i\Phi_3 & \Phi_2 + i\Phi_1 \\ -\Phi_2 + i\Phi_1 & \Phi_4 - i\Phi_3 \end{pmatrix}, \tag{6.4}$$

where d is the total number of vortices and antivortices. We subsequently normalize the fields: $\Phi'_\beta \equiv \Phi_\beta / ||\Phi_\beta||$, where $||\Phi_\beta|| \equiv (\sum_\beta (\Phi_\beta)^2)^{1/2}$, and use Φ'_β as an initial condition for the minimization procedure.

6.1.1 The inter-vortex force

It has been shown analytically [8] that in the Skyrme model the force between a vortex and an antivortex, when separated by large distances, is an attractive one. We now wish to see if this is still the case for generalized skyrme systems.

The vortex ansatz used in [8], for a vortex j located at the origin, is given by:

$$U_j = \exp\left[\frac{1}{2}(d_j\theta_j - k_j\beta z)i\sigma_3\right] \exp\left[f_j(r)i\sigma_1\right] \exp\left[\frac{1}{2}(d_j\theta_j + k_j\beta z)i\sigma_3\right], \tag{6.5}$$

where (r, θ_j) are polar coordinates in $\mathbb{R}^2$, $\beta = 2\pi/L_z$, d_j, and k_j are constants. The boundary conditions are such that the profile function $f_j(r)$ satisfies $f_j(0) = \pi/2$ and $f_j(r) \to 0$ as $r \to \infty$. Note that, for a vortex-antivortex pair, we choose $d_1 = -d_2 = 1$ and $k_1 = -k_2 = 1$, as they wind in opposite directions.

Using the product ansatz (6.4), the fields of a vortex-antivortex pair in the

asymptotic region (i.e. where $f_j(r) \approx 0$) are given by:

$$U = U_1 \cdot U_2 \approx \begin{pmatrix} e^{i(\theta_1-\theta_2)} & 0 \\ 0 & e^{-i(\theta_1-\theta_2)} \end{pmatrix} \equiv \begin{pmatrix} Z_1 & -Z_2^* \\ Z_2 & Z_1^* \end{pmatrix}, \tag{6.6}$$

where we have represented U in terms of (Z_1, Z_2) fields, as we did in sec. 2.4.1. Note that $Z_2 = -\Phi_2 + i\Phi_1 = 0$, so we can represent the vortex-antivortex fields as the U(1) fields $Z \equiv Z_1 = \Phi_4 + i\Phi_3$. Recall that the generalized energy density is given by (2.26), which we reproduce here:

$$\mathcal{E} = \kappa_2[(\partial_j\Phi_\beta)(\partial_j\Phi_\beta) - \alpha P_j P_j] + \kappa_4[2(1-\alpha)F^j_{\beta\gamma}F^j_{\beta\gamma} + \alpha Q^j Q^j], \tag{6.7}$$

where

$$\begin{aligned} P_j &= \Omega^{\beta\gamma}\Phi_\beta\partial_j\Phi_\gamma, \\ F^j_{\beta\gamma} &= \frac{1}{2}\varepsilon^{jkl}(\partial_k\Phi_\beta)(\partial_l\Phi_\gamma), \\ Q^j &= \Omega^{\beta\gamma}F^j_{\beta\gamma}, \end{aligned}$$

and where $\Omega_{12} = -\Omega_{21} = -\Omega_{34} = \Omega_{43} = 1$. However, note that for U(1) fields, the terms of order 4 in derivatives vanish, since they are antisymmetrized. Moreover, the terms $(\partial_j\Phi_\beta)^2$ and $(P_j)^2$ are equal, as can be checked by substituting the relevant fields Φ_3, Φ_4 and using the properties $\Phi_\beta\partial_i\Phi_\beta = 0$ and $(\Phi_\beta)^2 = 1$. This leaves us with the following expression for the energy density of a vortex-antivortex pair, in the asymptotic region:

$$\mathcal{E} = \kappa_2(1-\alpha)(\partial_j\Phi_\beta)^2 = \kappa_2(1-\alpha)||Z^*\partial_j Z||^2. \tag{6.8}$$

In [8], the energy (i.e. the integral of eq. (6.8) over the asymptotic region) is analytically calculated in quite an elegant fashion, as we now briefly explain. The $\mathbb{R}^2$ plane is divided into three regions: two discs of radii C centred on each of the vortices, which are separated by a distance of $2a$, and the rest

of the $\mathbb{R}^2$ plane. The distances C and a are such that $a > C$ and C is large enough so that one can make the approximation $f_j(r) \approx 0$ outside of the discs. The plane is then stereographically projected onto the two-sphere S^2, which is allowed, as the energy is conformally invariant. The projection can be chosen such that the two circles are now described on S^2 by $\theta = \gamma$ and $\theta = \pi - \gamma$, where $\theta \in [0, \pi]$ is now a spherical coordinate (the other coordinate given by $\phi \in [0, 2\pi)$) and where $\sin(\gamma) = C/a$. The asymptotic region is then equivalent to the region on S^2 given by $\theta \in [\gamma, \pi - \gamma]$ and $\phi \in [0, 2\pi]$. The energy is thus given by:

$$E = \kappa_2 L_z (1-\alpha) \int_0^{2\pi} \int_\gamma^{\pi-\gamma} (||Z^* \partial_\theta Z||^2 + \sin^{-2}\theta ||Z^* \partial_\phi Z||^2) \sin(\theta)\, d\theta\, d\phi\,, \tag{6.9}$$

where an integral in the $z-$direction over one period L_z has been performed. In [8], a Bogomolny argument was used to show that E is minimized by $Z(\theta, \phi) = \exp[i\phi]$. Alternatively, one could use a variational method to find functions Z that extremize the functional $E(Z, \partial_j Z)$, so that $\delta E = 0$. One finds that such functions are given by $Z(\theta, \phi) = \exp[ig(\theta, \phi)]$, where g is a function consisting of some linear combination of θ and ϕ. However, note that in the asymptotic region Z does not depend on θ, leaving us with functions $g(\theta, \phi) = \phi$.

Performing the integral with $Z(\theta, \phi) = \exp[i\phi]$ yields:

$$E = 4\pi L_z \kappa_2 (1-\alpha) \log(\cot(\gamma/2)) \tag{6.10}$$

$$\approx \frac{L_z}{\pi} \left(\frac{1-\alpha}{3-\alpha}\right) \log(\cot(C/2a)) \tag{6.11}$$

$$\approx \frac{L_z}{\pi} \left(\frac{1-\alpha}{3-\alpha}\right) \log(a)\,, \tag{6.12}$$

where we have used $\kappa_2 = 1/[4\pi^2(3-\alpha)]$, made the approximation $\gamma \approx C/a$, for $a >> C$, and picked out the leading log contribution to the energy. Note that in [8] the "normalization" constant κ_2 was not used. Therefore,

to reproduce their result, one would have to take $\alpha = 0$ in eq. (6.12) and multiply by $12\pi^2$.

If we think of α as being fixed, what (6.12) tells us is that the energy of the asymptotic region for a vortex-antivortex pair decreases when the distance between the vortices decreases, which means that the inter-vortex force is attractive. Moreover, what the multiplicative factor $(1 - \alpha)$ tells us is that this is the case for $\alpha \in [0, 1)$, with the leading term becoming less pronounced as α increases and vanishing altogether in the $\alpha \to 1$ limit. Our numerical results for the V+AV+V+AV solution from sec. 5.3.1 (Fig. 5.2) show the optimal $L_{x,y}$ periods increasing for $\alpha \to 1$. This seems to suggest that the vortices repel each other in this limit. However, this has yet to be proven rigorously.

Numerical Results

In an effort to better understand the interactions between a vortex and an antivortex in generalized skyrme systems, we have made some numerical investigations of this system in a triply-periodic lattice at different values of α with the introduction of certain perturbations, which we shall describe shortly. However, we first start by describing an array of solutions obtained at $\alpha = 0.5$, by using different initial conditions.

Fig. 6.1 (a)-(d) shows the energy density isosurfaces $\mathcal{E}$, where $\mathcal{E}$ is 0.5 times its maximum value, for four different solutions of the V+AV system with $\alpha = 0.5$. The quoted values of E/Q were obtained through a second-order finite difference method, using a lattice spacing of $h = 0.1$, and with associated errors calculated by taking the difference between the V+AV charge ($Q = 2$) and the charge obtained numerically, then dividing by 2.

These solutions were obtained through different mechanisms. Figs. 6.1 (a),(b) are local energy minima obtained by using the product ansatz (6.4) as an initial condition, with vortex cores at $(c_1^1, c_1^2) = (L_x/4, 3L_y/4)$, $(c_2^1, c_2^2) =$

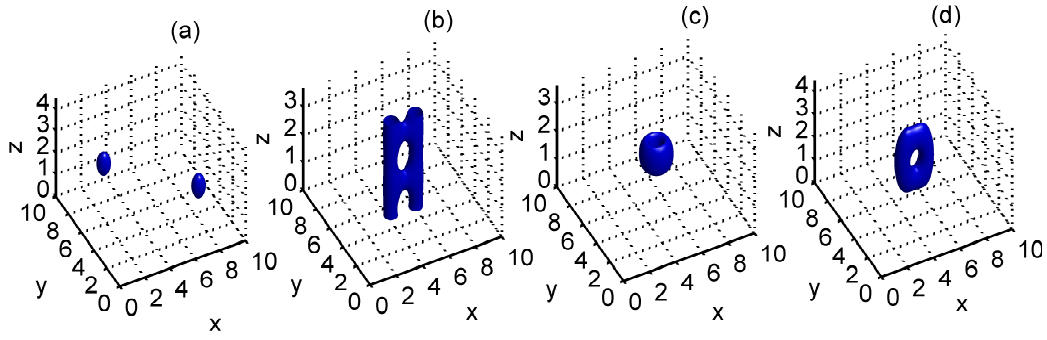

Figure 6.1: Energy density isosurfaces ($\mathcal{E} = 0.5 * \mathcal{E}_{\max}$) of V+AV solutions, for $\alpha = 0.5$ and $L_{x,y} = 10$: (a) Lumps ($E/Q = 1.22 \pm 0.02$, $L_z = 4.4$), (b) Merged Vortices ($E/Q = 1.09 \pm 0.01$, $L_z = 3.6$), (c) Coaxial Torus ($E/Q = 1.16 \pm 0.02$, $L_z = 3.6$), (d) Vertical Torus ($E/Q = 1.11 \pm 0.01$, $L_z = 4.4$).

$(3L_x/4, L_y/4)$, and $(c_1^1, c_1^2) = (L_x/4, L_y/2)$, $(c_2^1, c_2^2) = (3L_x/4, L_y/2)$, respectively, and vortex charges $(p_1, q_1) = (1, 1)$ and $(p_2, q_2) = (-1, -1)$ for both cases. Moreover, for Fig. 6.1 (a), a value of $\alpha = 0.5$ was used and for Fig. 6.1 (b) it was $\alpha = 0$, and afterwards re-minimized with $\alpha = 0.5$. A range of L_z values were scanned for both configurations, monitoring their energies in the process, and picking the minimal values, producing the configurations displayed in Figs. 6.1 (a),(b). Fig. 6.1 (c) was obtained by taking the field of Fig. 6.1 (a) as an initial condition and minimizing, after setting the energy gradient to zero at the edges of the fundamental cell and having the fields take the following values at the edges: $\Phi_1(0, y, z) = \Phi_1(L_x, y, z) = \Phi_1(x, 0, z) = \Phi_1(x, L_y, z) = 1$ and $\Phi_{2,3,4}(0, y, z) = \Phi_{2,3,4}(L_x, y, z) = \Phi_{2,3,4}(x, 0, z) = \Phi_{2,3,4}(x, L_y, z) = 0$ (more on this shortly). Finally, Fig. 6.1 (d) was obtained by taking the field of the "merged vortices" of Fig. 6.1 (b) as an initial condition, increasing L_z from 3.6 to 4.4, minimizing, and producing a "vertical torus" in the process. Note that its energy is larger than the merged vortices and it keeps increasing if L_z is increased further, so it is not a local energy minimum. Also note that the "coaxial torus" (Fig. 6.1 (c)) is not a local energy minimum. Its energy decreases as L_z is increased; the most likely explanation for this is that neighbouring coaxial

tori stacked in the $z-$direction would repel each other, unless an appropriate transformation is performed on the fields of one of them. A transformation that could work might consist of flipping one of them by π about the $x-$ or $y-$axes. If such a transformation makes them attractive, then the tori would subsequently merge, presumably producing a charge $Q = 4$ configuration with cubic symmetry.

We should stress at this point that there are different ways of obtaining the coaxial torus. For example, instead of imposing the asymptotic values for the fields at the edges of the fundamental cell, as previously mentioned, we take the fields of Fig. 6.1 (a) and introduce a perturbation by bringing the "lumps" closer together by varying amounts. This is done by deleting a varying number of vertical sheets of lattice sites (i.e. with $z \in [0, L_z]$) along the middle of the configuration in both the $x-$ and $y-$directions and adding the same number along the edges (by making a copy of the (y, z) and (x, z) sheets at the edges and adding them along the $x-$ and $y-$directions, respectively), thereby keeping $L_{x,y} = 10$ the same. Surprisingly, only when the number of deleted rows is > 20, corresponding to bringing them closer by a distance $D > 2$ along the $x-$ and $y-$directions (for $h = 0.1$), will the lumps merge into a coaxial torus. Otherwise, they repel each other until they are maximally separated, even when increasing $L_{x,y}$, which we checked up to a value of $L_{x,y} = 14$. This leads us to conclude that there are edge effects, removed by imposing a zero energy gradient at the edges as well as imposing the asymptotic value for one of the $(x, y)-$dependent fields at the edges. It is also worth noting that a torus is likely to exist for $\alpha \in [0, 1]$, as was suggested in [4]. For example, if one starts at $\alpha = 0$ with a charge $Q = 2$ skyrmion, whose energy density isosurfaces resemble tori, and α is subsequently increased (with the fields minimized for each value of α), one is likely to end up with a family of tori for different α values. However, this has yet to be investigated in detail.

We now turn to an analysis of the energy density isosurfaces of merged vortices as a function of α, which was carried out prior to obtaining the energy minima of Figs. 6.1 (a),(b). Recall that, in order to obtain Fig. 6.1 (b), the product ansatz was originally minimized with a value of $\alpha = 0$. Afterwards, a range of L_z values were scanned and found that $L_z = 4$ is the optimal one, coinciding with the results from [8]. To investigate the corresponding field configurations for different values of α, we initially guessed what the respective optimal values of L_z would be by comparing the $\alpha = 0$ optimal value with our results from the V+AV+V+AV configuration (see sec. 5.3.1) and claiming that the same difference would hold for other values of α. Later, we looked for the optimal L_z values more carefully, which we describe in the next section. The values of α and L_z used here are given by $\alpha = \{0, 0.5, 0.6, 0.7, 0.8, 0.9\}$ and $L_z = \{4.0, 3.3, 3.2, 3.1, 3.0, 2.9\}$. The minimized fields obtained for a certain value of α were used as an initial condition for the next (higher) value of alpha, with a corresponding change in L_z. Fig. 6.2 (a)-(f) shows their energy density isosurfaces, where $\mathcal{E} = 0.15 * \mathcal{E}_{\max}$ for Fig. 6.2 (a) and $\mathcal{E} = 0.5 * \mathcal{E}_{\max}$ for Figs. 6.2 (b)-(f), and with errors as calculated for Fig. 6.1. As with the V+AV+V+AV case, there is a tendency for the vortex-antivortex pair to become more homogeneous in the $z-$direction as α increases, having no noticeable $z-$dependence for $\alpha = 0.9$. Moreover, the distance between the vortices D, calculated by finding the distance between the maximum values of the energy density at $z = L_z/2$, was found to increase as α increases: $D = \{1.5, 1.9, 1.9, 2.1, 2.5, 2.8\}$. This seems to support our claim from the previous section that vortices repel each other when $\alpha \to 1$.

Further investigation of the V+AV configuration has been carried out by investigating its stability for different values of α. This will be analyzed in the next section by stacking multiple copies of the optimal L_z-valued fields in the $z-$direction, but first, we describe the process of obtaining these optimal values.

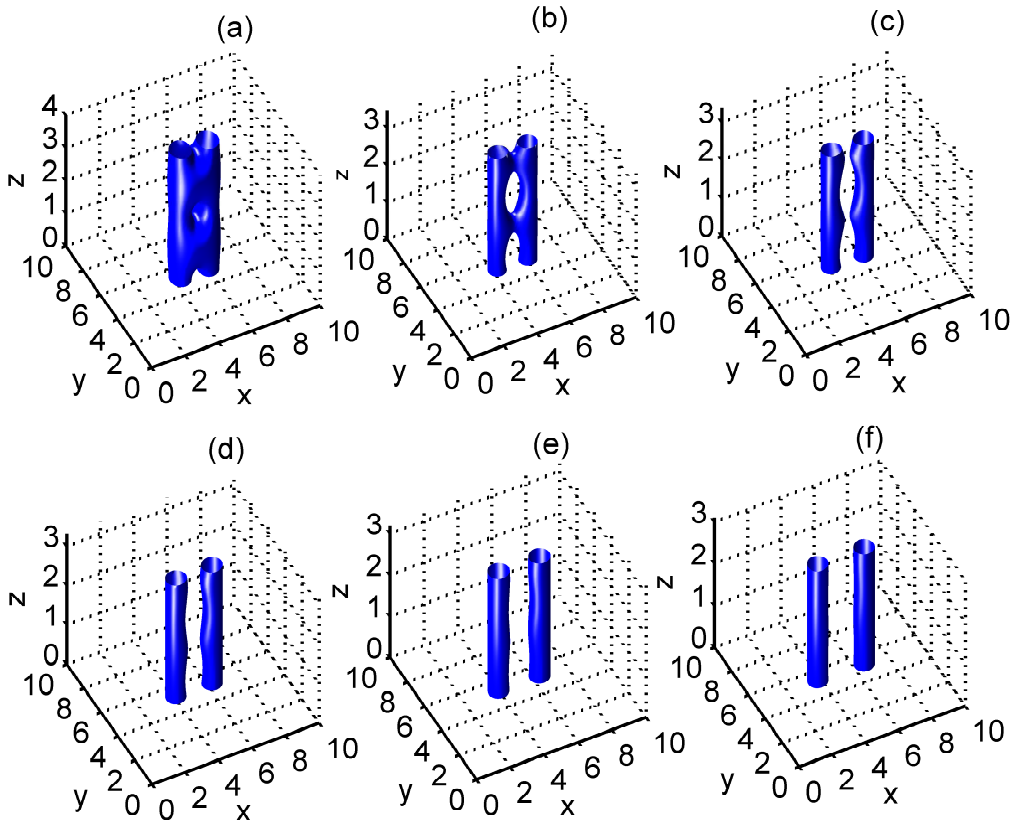

Figure 6.2: Energy density isosurfaces ($\mathcal{E} = 0.15 * \mathcal{E}_{\max}$ for Fig. (a) and $\mathcal{E} = 0.5 * \mathcal{E}_{\max}$ for Figs. (b)-(f)) of V+AV merged vortex solutions, for $L_{x,y} = 10$: (a) $\alpha = 0$ ($E/Q = 1.15 \pm 0.01$, $L_z = 4$), (b) $\alpha = 0.5$ ($E/Q = 1.09 \pm 0.01$, $L_z = 3.3$), (c) $\alpha = 0.6$ ($E/Q = 1.07 \pm .01$, $L_z = 3.2$), (d) $\alpha = 0.7$ ($E/Q = 1.04 \pm 0.01$, $L_z = 3.1$), (e) $\alpha = 0.8$ ($E/Q = 1.00 \pm 0.01$, $L_z = 3.0$), (f) $\alpha = 0.9$ ($E/Q = 0.95 \pm 0.01$, $L_z = 2.9$).

6.1.2 V+AV multi-stack solutions

The techniques used in obtaining the optimal L_z values for the V+AV configuration, as a function of α, are similar to the ones used for the V+AV+V+AV solution from sec. 5.3.1, which we summarize here. The technique consists of scanning the energies of the V+AV configuration, using a first-order finite-difference method, through a range of L_z values and fitting a second-order polynomial through the three points with lowest energy and determining the minimal $E_{\min}$ and $L_{z,\min}$ values of the fit; the associated charge $Q_{\min}$ is also obtained through interpolation, by comparing the charges corresponding to the points nearest to the minimum. These minimal values are obtained for three different values of lattice spacing ($h = 0.1, 0.15, 0.2$), for different values of α. Therefore, at each value of α, we fit a line through $E_{\min}(h^2)$, $L_{z,\min}(h^2)$, and $Q_{\min}(h^2)$ and extrapolate $h^2 \to 0$. The extrapolated values $E_{\min}(0) \equiv E$, $E_{\min}(0)/2 \equiv E_N$, and $L_{z,\min}(0) \equiv L_z$, for $\alpha = \{0, 0.2, 0.5, 0.7, 0.9\}$, are listed in Table 6.1. The quoted errors for the normalized energies E_N were calculated by taking the difference between $Q_{\min}(0)$ and the "true" charge $Q = 2$ and dividing by 2. Fig. 6.3 shows a plot of E_N and L_z vs α. Note that the pattern is similar to that of the V+AV+V+AV solution, whose values of E_N and L_z were shown to decrease as α increases.

Table 6.1: Optimal periods and minimal energies of V+AV configuration

α	L_z	E	E_N
0	4.03	2.317	1.159±0.002
0.2	3.77	2.284	1.142±0.001
0.5	3.48	2.196	1.098±0.002
0.7	3.3	2.094	1.047±0.002
0.9	3.06	1.920	0.960±0.004

We now wish to investigate the stability of the V+AV configuration by stacking their minimal-energy fields $N = \{1, 2, 3, 4, 5\}$ times in the $z-$direction. Anticipating copious amounts of processing time in obtaining the minimum energy fields for large N, we have decided to use a larger value of the lattice spacing $h = 0.2$ for $N > 2$, while keeping $h = 0.1$ for

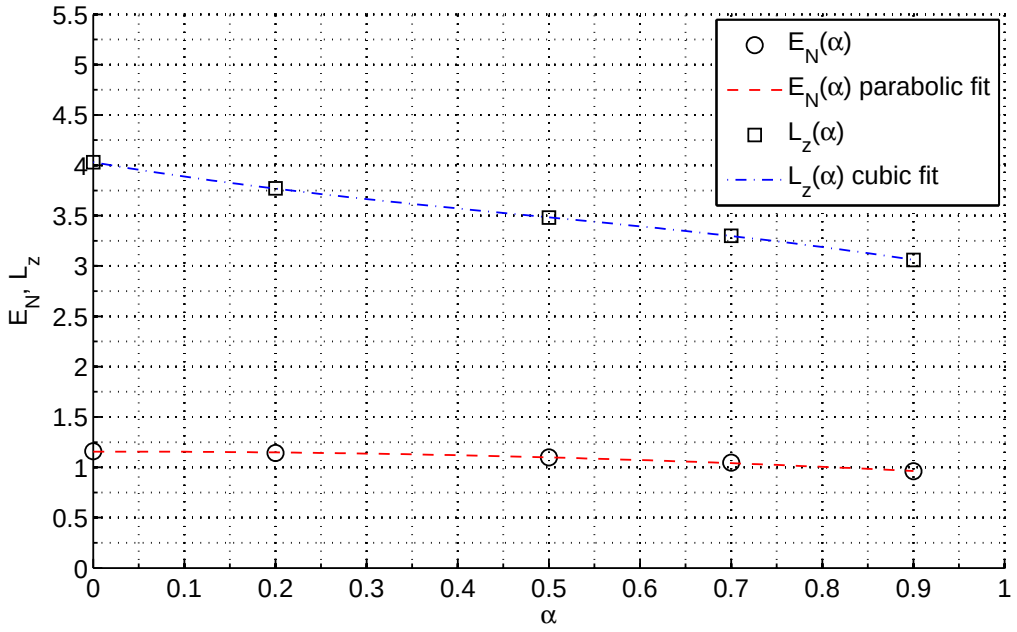

Figure 6.3: Plot of minimal normalized energies E_N and optimal periods L_z vs. α for V+AV configuration.

$N = (1, 2)$. The idea is to take a copy of the minimal-energy $N = 1$ fields, for $\alpha = \{0, 0.2, 0.5, 0.7, 0.9\}$, and place them on top of each other N times with a slight perturbation and then minimize their energies. For $N = 2$, the perturbation consists of shifting the top copy in the $x-$direction by 5 lattice sites (equivalent to a distance $D = h_x * n_x = 0.5$) and for $N > 2$, it consists of bringing the two vortices in the middle copies closer together by $D = 0.6$. For the $\alpha = \{0.5, 0.7\}$ cases, this is done by deleting vertical sheets of lattice sites (i.e. $z \in [0, L_z]$) along the middle of the configuration, with the middle sheet approximately corresponding to $x = L_x/2$, and adding the same number of sheets along the edges by taking a copy of the edge sheets, and thus, keeping $L_x = L_y$ constant. For the $\alpha = \{0, 0.2, 0.9\}$ cases, it is worth noting that the initial condition consists of vortices located along a diagonal in the $(x, y)-$plane and, therefore, lattice sites are removed along the middle of the configuration in both the $x-$ and $y-$directions (while adding the same number along the edges), in order to bring them diagonally closer together by a distance $D \approx \{0.6, 0.6, 0.9\}$, respectively. Since the optimal L_z

values differ slightly for the $h = 0.1$ and $h = 0.2$ fields, we use different initial conditions for the $N = (1, 2)$ and $N > 2$ cases, corresponding to minimized fields with L_z values closest to the optimal ones for which the corresponding number of lattice sites in the $z-$direction is even, since we shall be using a second-order finite difference method to determine the energy E and charge Q for each configuration. The $N = 1$ ($h = 0.1$) fields, used for the $N = \{1, 2\}$ stacks, have $L_z = \{4, 3.8, 3.4, 3.2, 3.0\}$ (for the aforementioned values of α), and the $N = 1$ ($h = 0.2$) fields, used for the $N = \{3, 4, 5\}$ stacks, have $L_z = \{3.8, 3.6, 3.2, 3.0, 3.0\}$.

The result of minimizing the energy of these initial conditions can be seen in Fig. 6.4, which shows their energy density isosurfaces. The rows correspond to different N values, with N increasing downwards (from $N = 1$ to $N = 5$), and the columns correspond to different α values, with α increasing to the right (from $\alpha = 0$ to $\alpha = 0.9$). Note that the periods L_z for the N-stacks are given by multiplying the aforementioned L_z values for the $N = 1$ fields (with the appropriate values of $h = 0.1$ and $h = 0.2$) N times. The only exceptions to this rule are the $N = (3, 5)$ stacks for: $\alpha = 0$ ($L_z = 11.2, 19.2$, respectively) and $\alpha = (0.7, 0.9)$ ($L_z = 9.2, 15.2$). Moreover, the surface values chosen in order to accentuate their features are given by $\mathcal{E} = 0.15 * \mathcal{E}_{\max}$ for the $\alpha = 0$ N-stacks, $\mathcal{E} = 0.25 * \mathcal{E}_{\max}$ for the $\alpha = 0.2$ N-stacks, and $\mathcal{E} = 0.5 * \mathcal{E}_{\max}$ for the rest. Table 6.2 lists the corresponding normalized energy values ($E_N = E/Q$), with errors calculated as before, except that we now use a value of $Q = 2N$. The E_N values were calculated by using a second-order finite difference method, with $h = 0.1$ for $N = (1, 2)$ and $h = 0.2$ for $N = (3, 4, 5)$.

The V+AV N-stack solutions exhibit some peculiar features as α is changed, as we now briefly describe. Starting with the $\alpha = 0$ case, we see that the $N = 1$ and $N = 2$ stacks correspond to regular Skyrme chains (see [8]), whereas the $N = 3$ and $N = 4$ solutions correspond to the standard $Q = 6$ skyrmion

and the fullerene-like[1] $Q = 8$ solution, respectively (see e.g. [10, 21]). This suggests that Skyrme chains are unstable to clumping, as pointed out in [8]. However, note that we have not varied L_z for $N \geq 2$, which leaves open the possibility that Skyrme chains might exist for these (and possibly even higher) N values. The $N = 5$ solution is a non-fullerene-like polyhedron, consisting of 16 pentagons and two squares at both ends. The $\alpha = 0.2$ case is similar to the $\alpha = 0$ case, except that it is even more unstable to clumping, as the $N = 2$ stack collapses into the standard $Q = 4$ skyrmion with cubic symmetry. The only other difference is the $N = 5$ solution, which is again a polyhedron that is not fullerene-like, consisting of 16 pentagons and this time two hexagons at both ends.

We start seeing qualitatively different solutions in the $\alpha = 0.5$ case. The $N = 2$ solution consists of a surface that has two holes facing in the $x-$direction and also in the $y-$direction. Recall that a similar-looking solution motivated Prof. Ward to look for its optimal periods and eventually led to the discovery of the multi-sheet solution (see sec. 5.3.3), but note that the value of α used by him was different ($\alpha = 0.8$). The $N = 3$ solution is the first example of a braided V+AV pair, where each of the vortices braids once around the other, winding by 2π in the $z-$direction. This is the case for the other braided structures seen at $\alpha = 0.7$, $N = 3, 4$, but not so for the $\alpha = 0.5$, $N = 5$ structure, where the vortices braid around each other twice, but apparently preferring to do so along the diagonal in the $(x, y)-$plane. The $\alpha = 0.5$, $N = 4$ and $\alpha = 0.7$, $N = 5$ solutions are the only examples of isolated, twisted loops. One can imagine obtaining configurations like these by holding a torus from one end and twisting the other end by 2π. For the $N = 1$ solutions, we can see that the merged vortices at $\alpha \leq 0.5$ are now separated at $\alpha = 0.7$ and $\alpha = 0.9$, which is still the case for $N = 2$, but where now the vortices wind by 2π in the $z-$direction. The vortices at

[1] We adopt the definition from [21], which states that fullerene-like skyrmions are those whose energy density isosurfaces resemble polyhedra consisting of 12 pentagons and $2Q$-14 hexagons, for $Q \geq 7$.

$\alpha = 0.9$ continue to be separated all the way up to $N = 5$, still winding by 2π, but one can notice that the solutions no longer wind smoothly and continuously in the $z-$direction for $N \geq 3$.

To sum up, we have seen that the V+AV configuration for $\alpha \in [0, 0.9]$ is unstable to stacking in the $z-$direction, in the sense that they do not preserve their shape. In the $\alpha = 0, 0.2$ cases, the shapes are still intact up to $N = 2$, but subsequently collapse into both fullerene and non-fullerene-like polyhedra, possibly due to the type of perturbation that we use and the fact that the vortices are closer together than for higher values of α. For $\alpha \geq 0.5$, the V+AV configurations collapse into winding, braided, and twisted structures. Perhaps it is not surprising to see such behaviour, as it is a well-known fact that in the $\alpha \to 1$ limit, it is energetically favourable for Hopf solitons to twist and link with each other as the value of the Hopf charge increases (see e.g. [31, 38]).

In order to analyze the properties (such as the charge) of these winding and braiding structures, we have made use of an ansatz which replicates their dependence in the three Cartesian coordinates. We now turn to a description of this ansatz as well as how we use it to analyze some of the fields featured in Fig. 6.4.

Table 6.2: Normalized energies ($E_N = E/Q$) of V+AV N-stack solutions with associated errors.

	$\alpha = 0$	$\alpha = 0.2$	$\alpha = 0.5$	$\alpha = 0.7$	$\alpha = 0.9$
$N = 1$	1.1581 ± 0.0004	1.1414 ± 0.0003	1.0975 ± 0.0003	1.0465 ± 0.0003	0.9592 ± 0.0004
$N = 2$	1.1581 ± 0.0004	1.1074 ± 0.0003	1.0658 ± 0.0002	1.0382 ± 0.0002	0.9408 ± 0.0002
$N = 3$	1.107 ± 0.005	1.100 ± 0.005	1.044 ± 0.004	0.972 ± 0.004	0.944 ± 0.004
$N = 4$	1.095 ± 0.005	1.091 ± 0.005	1.060 ± 0.005	0.971 ± 0.004	0.940 ± 0.003
$N = 5$	1.099 ± 0.005	1.083 ± 0.004	1.041 ± 0.004	0.991 ± 0.006	0.915 ± 0.002

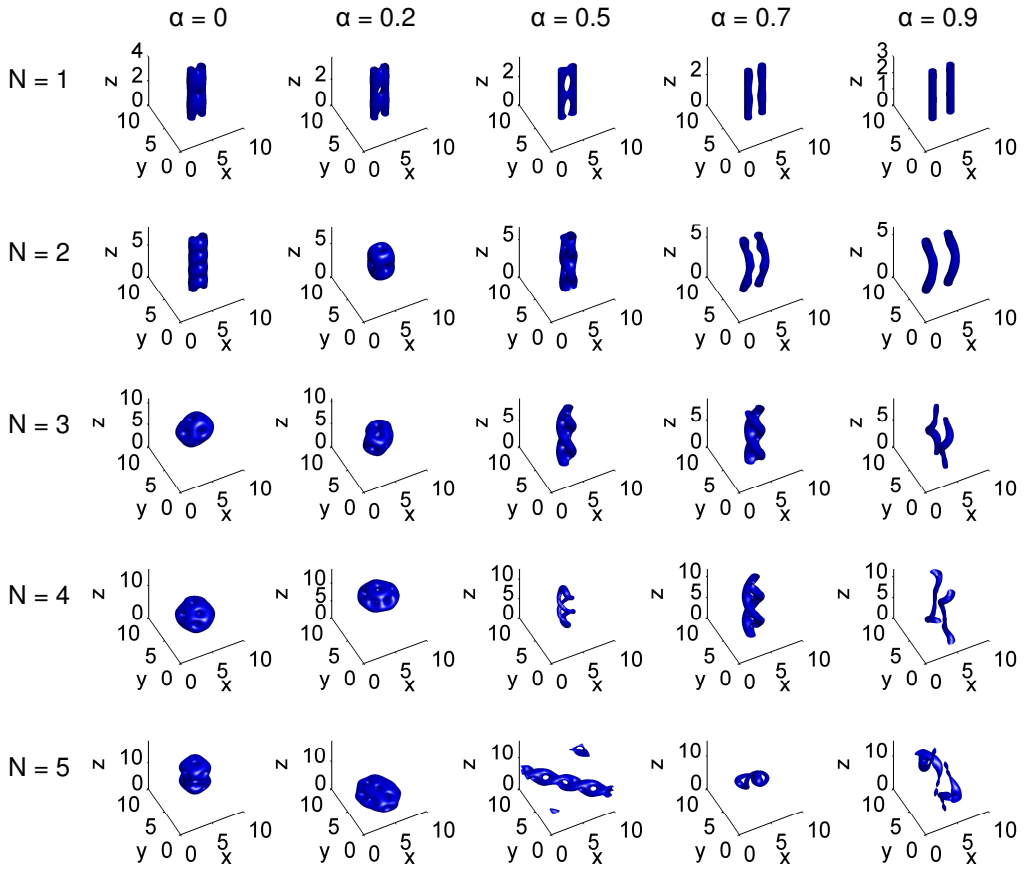

Figure 6.4: V+AV N-stack energy density isosurfaces for $N = (1, 2, 3, 4, 5)$ and $\alpha = (0, 0.2, 0.5, 0.7, 0.9)$; the surface values used are: $\mathcal{E} = (0.15, 0.25) * \mathcal{E}_{\max}$ for $\alpha = (0, 0.2)$, respectively, and $\mathcal{E} = 0.5 * \mathcal{E}_{\max}$ for the rest.

6.1.3 The braided V+AV ansatz

The ansatz for multi-vortices (5.14), from sec. 5.3.1, can be used to describe the braided solutions in Fig. 6.4 if we modify it in such a way that the locations of the vortex cores have a helical dependence, rather than being stationary in the $(x, y)-$plane, as functions of z. This can be done as follows:

$$\frac{U}{V} \equiv \frac{\Phi_3 + i\Phi_4}{\Phi_1 + i\Phi_2} = \frac{e^{\frac{2\pi i q_1 z}{L_z}}}{(w_1)^{p_1}} + \frac{e^{\frac{2\pi i q_2 z}{L_z}}}{(w_2)^{p_2}}\,, \tag{6.13}$$

where (p_j, q_j) refer to the $(p, q)-$charges of vortex j, as before, and the w_j are now given by:

$$w_1 = (x - aL_x) + i(y - bL_y) + (m + ik)e^{\frac{2\pi i b z}{L_z}}\,, \tag{6.14}$$

$$w_2 = (x - gL_x) + i(y - hL_y) + (d + if)e^{\frac{2\pi i b z}{L_z}}\,, \tag{6.15}$$

where (a, b, m, k) and (g, h, d, f) are parameters which specify the locations of the cores of vortices 1 and 2, respectively, and b is an integer we refer to as the "braiding number" or "linking number" which specifies the number of times the cores wind by 2π in the $z-$direction, over the period L_z, with its sign depending on whether the vortices wind clockwise or counterclockwise. By looking at the energy density isosurfaces of V+AV solutions, one can estimate the location of the vortex cores, choose the appropriate parameters, and (approximately) reproduce the path of the cores. Note that if we choose $(a, b) = (g, h)$ and $(m, k) = -(d, f)$ we get vortex cores which revolve about a common centre and are connected by a line passing through the centre (i.e. they link with each other $|b|$ times).

To get a feeling of how the charge Q of a V+AV system depends on the braiding number b and the charges q_j, we first numerically calculate the charge Q of braided V+AV fields produced analytically, by using the ansatz (6.13), for many different values of b and q_j. After analyzing such a list

of charges, we have come to the conclusion that they follow the following formula, with $|p_1| = |p_2| \equiv p$:

$$Q = p(|q_1| + |q_2|) - 2bp^2 \,. \tag{6.16}$$

Note that eq. (6.16) is only compatible for V+AV configurations that are linked. An alternate method for calculating the charge of configurations that are not linked will be discussed later on.

We now wish to verify eq. (6.16) by numerically calculating the (p, q_1, q_2) charges of some of the linked V+AV $N-$stack solutions from Fig. 6.4. We should stress that the linking number b is an artifact that we implemented to try to analytically reproduce the energy density isosurfaces of such solutions, so it is not information that is carried by the fields of those solutions and, therefore, cannot be "measured" by carrying out certain operations on the fields, such as those performed below to measure their $(p, q_1, q_2)-$charges. However, the linking number is something that can be determined quite easily for V+AV fields, whose charge we wish to calculate, by simply looking at how many times their energy density isosurfaces link with each other over the period L_z.

We start by describing a numerical method for calculating the $q-$charge of a vortex (or antivortex). Recall from the single vortex (or antivortex) ansatz (eq. (5.14), with $d = 1$) that q corresponds to a $z-$dependent winding number:

$$\frac{U}{V} \equiv \frac{\Phi_3 + i\Phi_4}{\Phi_1 + i\Phi_2} = \frac{e^{\frac{2\pi i q z}{L_z}}}{(w)^p} \,, \tag{6.17}$$

where $w = (x - c^1) + i(y - c^2)$ and $(x, y) = (c^1, c^2)$ specifies the location of the core of the vortex in the $(x, y)-$plane. We can make use of this ansatz to find an analytic expression that we can use to numerically determine the

charge q, as follows:

$$\left|\frac{\partial U}{\partial z}\right|^2 = \left(\frac{\partial \Phi_3}{\partial z}\right)^2 + \left(\frac{\partial \Phi_4}{\partial z}\right)^2 = \left(\frac{2\pi q}{L_z}\right)^2 . \tag{6.18}$$

Solving for $|q|$ yields an expression involving the z derivatives of the fields Φ_3, Φ_4. We are now ready to numerically determine the charge $|q|$. To do this, we first identify the location of the vortex cores by using expressions (6.14, 6.15), with parameters determined through trial and error – i.e. by comparing the resulting curves with the energy density isosurface we wish to study. Having done this, we measure the fields Φ_β at each grid point along the curve and take their approximate $z-$derivative by using a first-order finite difference method. Finally, we make use of eq. (6.18) to determine the value of $|q|$ at each point along the curve and we take its average value. Fig. 6.5 (a) shows the curves of the vortex-antivortex cores for the $\alpha = 0.5$ V+AV 3-stack solution; Fig. 6.5 (b) shows the value of $|q|$ as a function of z for the blue curve, with average value given by $\text{avg}(|q|) = 1.8$ (the red curve has a similar value); Fig. 6.5 (c) shows the associated energy density isosurface, with $\mathcal{E} = 0.5 * \mathcal{E}_{\text{max}}$. The other solutions whose $|q|-$charges we measured are: $\alpha = 0.7$ V+AV 3-stack, with $\text{avg}(|q|) = 2.0$, and $\alpha = 0.7$ V+AV 4-stack, with $\text{avg}(|q|) = 2.5$ (we shall discuss this value later on). One should note that the same average value of $|q|$ is obtained for both the vortex and the antivortex in each solution. We should stress that this method is not exact, since it involves approximating the derivative of the fields as well as the location of the vortex cores. The resulting average value of $|q|$ has to be rounded, as it is usually not an integer. Therefore, to double-check it, we make use of an alternative method for calculating $|q|$ and compare the results. However, to do this, we first need to measure the charge p for the braided V+AV configurations.

Recall from sec. 5.3.1 that the $p-$charge of a vortex corresponds to its winding number on the $(x, y)-$plane for $z = c$, where c is a constant. Re-

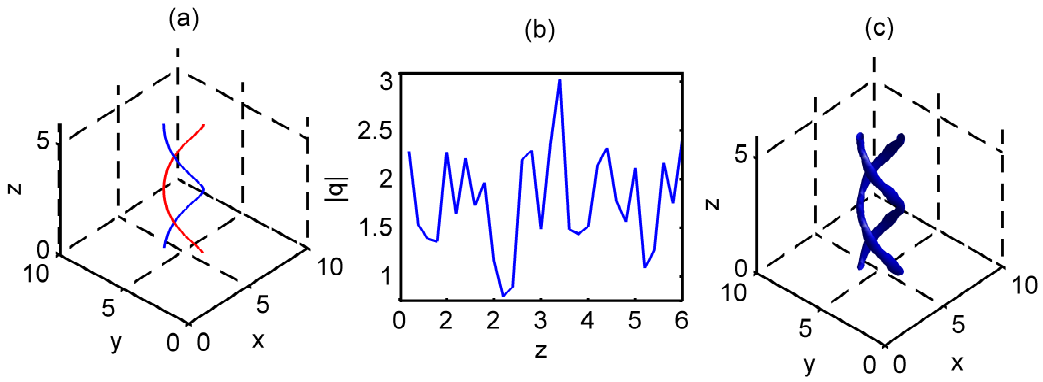

Figure 6.5: Numerical calculation of the $\alpha = 0.5$ V+AV 3-stack solution $q-$charge. Fig. (a) shows the approximate location of the vortex-antivortex cores; Fig. (b) plots the charge $|q|$ as a function of z of the blue vortex from Fig. (a); Fig. (c) shows the associated energy density isosurface, with $\mathcal{E} = 0.5 * \mathcal{E}_{\max}$.

stricting ourselves to such a plane, the $p-$charge can be calculated by performing a Hopf projection of the fields Φ_β, given by $\psi^a = Z^\dagger \sigma_a Z$, where $Z \equiv (Z_1, Z_2)^T \equiv (\Phi_4 + i\Phi_3, -\Phi_2 + i\Phi_1)^T$, and then calculating the "baby skyrme" charge[2] of the fields ψ^a over the half F of the plane occupied by one of the vortices (recall that, under a Hopf projection, the $p-$charges must add up to zero):

$$p = \frac{1}{4\pi} \int_F \vec{\psi} \cdot (\partial_1 \vec{\psi} \times \partial_2 \vec{\psi})\, d^2x\,. \tag{6.19}$$

In our numerical calculations, we interpret the integral in eq. (6.19) as an average of the values of the integrand over the region F, where the derivatives are approximated using a first-order finite difference method and the value of the lattice spacing depends on its value for the field being studied: $h = 0.1$ for the $N = (1, 2)$ solutions and $h = 0.2$ for the $N = (3, 4, 5)$ solutions. We choose the plane $z = c$ where the vortices are located in such a way that it makes it easy for us to calculate the charge p in each half (i.e. two square regions). The solutions whose $p-$charges we measured (p_1 for the vortex and p_2 for the antivortex) are: $\alpha = 0.5$ V+AV 3-stack ($|p_1| = |p_2| = 0.90$),

[2]The Baby Skyrme model is the two-dimensional analogue of the Skyrme model (see e.g. [10]).

$\alpha = 0.7$ V+AV 3-stack ($p_1 = 0.95$; $p_2 = -0.94$), $\alpha = 0.7$ V+AV 4-stack ($|p_1| = |p_2| = 0.96$), $\alpha = 0.7$ V+AV 2-stack ($p_1 = 0.97$; $p_2 = -0.98$), and $\alpha = 0.9$ V+AV 3-stack ($p_1 = 0.93$; $p_2 = -0.94$). These values, when rounded, confirm the fact that we are dealing with 1V+1AV pairs.

Using the rounded value of $|p| = 1$, we can manipulate eq. (6.16) to obtain $|q_1| + |q_2| = Q + 2b$. Since we have already noticed that $|q_1| = |q_2| \equiv |q|$, we can further simplify this expression to get $|q| = (Q + 2b)/2$. Assuming we know the value of Q (obtained numerically, for example), we can now double-check our $|q|-$charge measurements. For the $\alpha = 0.5$ and $\alpha = 0.7$ V+AV 3-stack solutions, $Q = 6$, and for the $\alpha = 0.7$ V+AV 4-stack, $Q = 8$. Suppose we do not know the sign of b; since we know that the vortices wind around each other once, we could try the values $b = \{-1, 1\}$, and simply pick the one that yields the value of b that comes closest to the value we measured earlier. Using these values of b for the $\alpha = 0.5$ and $\alpha = 0.7$ V+AV 3-stack solutions ($Q = 6$), we would get $|q| = \{2, 4\}$, and for the $\alpha = 0.7$ V+AV 4-stack solution ($Q = 8$), we get $|q| = \{3, 5\}$. Recall that, for these solutions, we measured $\text{avg}(|q|) = \{1.8, 2.0, 2.5\}$, respectively, and thus we conclude that their charges are: $|q| = \{2, 2, 3\}$. Note that we have also tested eq. (6.16) using (6.14, 6.15) to produce analytic fields for various values of (b, p, q_1, q_2) and, subsequently, numerically measured their charge Q (with a lattice spacing of $h = 0.1$); the resulting value of Q agrees with (6.16) in every case.

Recall that eq. (6.16) only works for linked vortices, so we end this section by discussing an alternate method used to obtain the charge Q for both linked and unlinked V+AV configurations. We adopt the techniques presented in [38], used to obtain the charge of Hopf solitons. Therefore, we need to perform a Hopf projection of the fields Φ_β to obtain the Hopf fields $\vec{\psi}$ – this time, no longer restricting ourselves to a plane $z = c$ as we did before to measure the $p-$charges. To calculate the charge Q of a V+AV configuration we first have

to determine the "winding number" of each vortex (or antivortex). This, in turn, is given by the number of times the linking curve, which we take to be the preimage of the point $\psi^1 = 1$ on the target 2-sphere, winds around the position curve of a vortex – defined as the preimage of the point $\psi^3 = -1$, which is antipodal to the vacuum value. Note that the point $\psi^1 = 1$ is an arbitrary choice. Any other point on S^2, aside from $\psi^3 = 1$, works equally well as long as one can easily determine the winding number from the curves.

To calculate the charge Q of an unlinked V+AV configuration, one simply adds the winding numbers of the vortex and the antivortex. On the other hand, for a linked configuration, one adds 1 to each of the winding numbers before adding them, due to the fact that the linking curve of the vortex also winds around the antivortex, and vice versa. Fig. 6.6 (a)-(e) shows the linking (blue) and position (green) curves for various different linked and unlinked V+AV $N-$stack solutions with the following (α, N) values: (a) (0.5,3); (b) (0.7,3); (c) (0.7,4); (d) (0.7,2); and (e) (0.9,3). For clarity, we have thickened these curves by choosing a circle of vectors with the constant values $\psi^1 = 0.9$ (blue curves) and $\psi^3 = -0.5$ (green curves), with the exception of Fig. 6.6 (d), where we use a value of $\psi^3 = -0.85$. Note that we have numerically calculated the $(p, q)-$charges for the fields corresponding to Figs. 6.6 (a)-(c) and Figs. 6.6 (d),(e) are examples of V+AV unlinked solutions. One can see, with a bit of effort, that the vortices in Fig. 6.6 have the following winding numbers: (a) 2; (b) 2; (c) 3; (d) 2; and (e) 3, which is consistent with the aforementioned method for calculating Q. Recall that we had measured a value of $\text{avg}(|q|) = 2.5$ for the $\alpha = 0.7$ V+AV 4-stack solution (Fig. 6.6 (c)). If one assumes the winding numbers represent the $|q|-$charges, then this is further confirmation of the fact that the $\alpha = 0.7$ V+AV 4-stack solution has a $|q|-$value of 3.

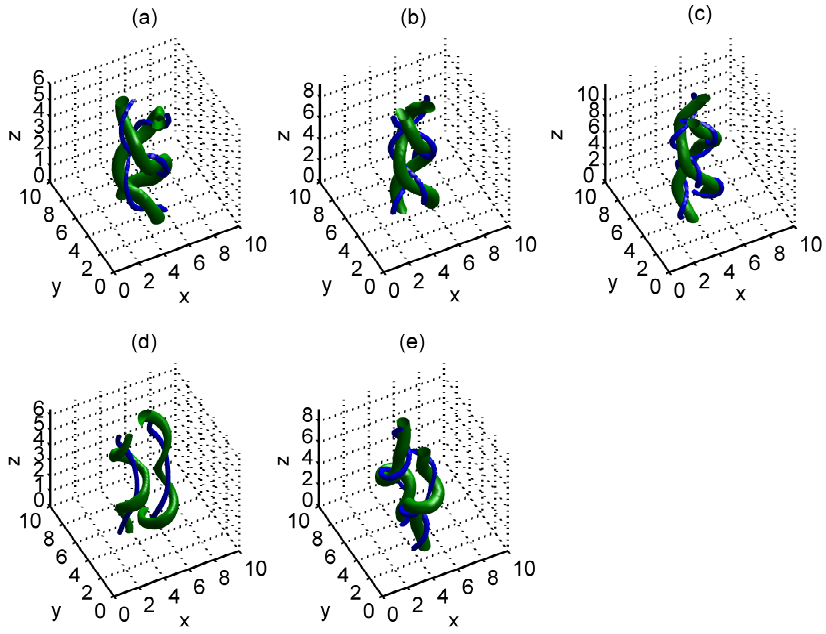

Figure 6.6: Hopf projection of various V+AV $N-$stack solutions with the following (α, N) values: (a) (0.5,3); (b) (0.7,3); (c) (0.7,4); (d) (0.7,2); (e) (0.9,3) and winding numbers: (a) 2; (b) 2; (c) 3; (d) 2; (e) 3. The green isosurfaces $\psi^3 = -0.5$ ($\psi^3 = -0.85$ for (d)) correspond to the position curves and the blue isosurfaces $\psi^1 = 0.9$ correspond to the linking curves.

6.2 V+AV+V+AV multi-stack solutions

In this (last) section we briefly discuss the V+AV+V+AV analogue of the V+AV $N-$stack solutions from the previous section. Again, we make use of the ansatz for multi-vortices (5.14), now applied to the case of two 1-vortices and two 1-antivortices:

$$\frac{U}{V} \equiv \frac{\Phi_1 + i\Phi_2}{\Phi_3 + i\Phi_4} = \sum_{j=1}^{4} \frac{e^{\frac{2\pi i q_j z}{L_z}}}{w_j}\,, \tag{6.20}$$

where $q_1 = -q_2 = q_3 = -q_4 = 1$ and the w_j are given by:

$$w_1 = Ae^{\Lambda|A|^2}\,, \text{ where } A = (x - L_x/2) + i(y - L_y/2) + c\,, \tag{6.21}$$

$$w_2 = Be^{\Lambda|B|^2}\,, B = (x - L_x/2) - i(y - L_y/2) - c^*\,, \tag{6.22}$$

$$w_3 = Ce^{\Lambda|C|^2}\,, C = (x - L_x/2) + i(y - L_y/2) + c^*\,, \tag{6.23}$$

$$w_4 = De^{\Lambda|D|^2}\,, D = (x - L_x/2) - i(y - L_y/2) - c\,, \tag{6.24}$$

where Λ is a parameter that determines how quickly the fields reach their asymptotic values away from the cores (we take $\Lambda = 0.8$) and $c = 2 + 2i$. This places the $j = \{1, 3\}$ vortex cores at $(x, y) = (L_x/2 - 2, L_y/2 \pm 2)$ and the $j = \{2, 4\}$ antivortex cores at $(x, y) = (L_x/2 + 2, L_y/2 \pm 2)$ (i.e. the distance D between diametrically opposite vortices is given by $D = 4\sqrt{2}$). The fields are subsequently normalized: $U' \equiv U/||U||$ and $V' \equiv V/||V||$, with $||U|| = ||V|| \equiv \sqrt{|U|^2 + |V|^2}$. Furthermore, we impose the following boundary conditions: $U(0, y, z) = U(L_x, y, z) = U(x, 0, z) = U(x, L_y, z) = 0$ and $V(0, y, z) = V(L_x, y, z) = V(x, 0, z) = V(x, L_y, z) = 1$. This set-up is used as the initial condition (i.c.) for minimization of the fields in the $\alpha = 0.3$ case; these minimized fields are then used as the i.c. for the $\alpha = 0, 0.6$ cases, while for the $\alpha = 0.9$ case, the minimized $\alpha = 0.6$ fields are used as the i.c. – explained in more detail below. Recall that we used similar boundary conditions in the V+AV case, sec. 6.1.1, with the effect of causing the vortices

to merge into a coaxial torus; otherwise, without these boundary conditions, one needs to perturb them by bringing them close together in order for them to merge.

Our goal here, as in the V+AV case of the previous section, is to analyze the stability of the V+AV+V+AV configuration for $\alpha = \{0, 0.3, 0.6, 0.9\}$, by stacking them $N = \{1, 2, 3, 4, 5\}$ times in the $z-$direction. We shall be using a lattice spacing of $h = 0.2$ and periods $L_{x,y} = 10$. The L_z optimal periods of the $N = 1$ V+AV+V+AV solution (for $h = 0.2$) are given by $L_z = \{4.55, 3.93, 3.49, 2.85\}$ for the aforementioned values of α; these were taken into account in the $h \to 0$ extrapolation of L_z (see Table 5.2, sec. 5.3.1). However, since we wish to use a second-order finite difference method in determining the energies E and charges Q for each configuration, we use L_z values that are associated with an even number of lattice sites in the $z-$direction and are also closest to the optimal ones, given by $L_z = \{4.4, 4, 3.6, 2.8\}$. For $N > 1$, we simply take these periods and multiply them by N; the only exception is for the $\alpha = 0.9$ case, where we use $L_z = \{2.8, 6, 9.2, 12, 15.2\}$, for N =1-5.

We introduce different kinds of perturbations for the $N = 2$ and $N > 2$ cases. In the former case, we translate the top copy in the $+x$-direction by 3 lattice sites (i.e. by a distance $D = 0.6$), and in the latter case, the four vortices (for the middle copies) are brought closer together by removing the lattice sites along the middle of the configuration in the $x-$ and $y-$directions, corresponding to $(x, y) \in [4.4, 5.6]$. The fields are subsequently minimized by flowing down the energy gradient. The local minima obtained can be seen in Fig. 6.7, where the energy density isosurfaces are plotted for various values of α and N. The surface values are given by: $\mathcal{E} = 0.15 * \mathcal{E}_{\max}$ for $\alpha = 0$; $0.25 * \mathcal{E}_{\max}$ for $\alpha = (0.3, 0.6)$; $0.5 * \mathcal{E}_{\max}$ for $\alpha = 0.9$, $N = \{1, 2, 4\}$, and $0.3 * \mathcal{E}_{\max}$ for $N = \{3, 5\}$. These are organized such that the aforementioned α values increase to the right and N increases downwards. The corresponding

normalized energies ($E_N = E/Q$) with associated errors $(Q - Q_{\text{num}})/Q$ are listed in Table 6.3, where Q_{num} is defined as the numerically calculated charge and Q is now given by $Q = 4N$.

The differences between the V+AV+V+AV and V+AV $N-$stack solutions are immediately apparent, as one can see from Fig. 6.7. First of all, examples of twisted and braided vortices now only occur at $\alpha = 0.9$, whereas for the V+AV case, they appeared at $\alpha = \{0.5, 0.7, 0.9\}$; the $N = 2$ case corresponding to twisting and unbraided vortices and the $N = \{3, 4, 5\}$ cases corresponding to two sets of braided vortices, all winding by 2π in the $z-$direction. Furthermore, for the $\alpha = \{0.3, 0.6\}$ (N =1-5) cases, the V+AV+V+AV configurations are now stable, under similar kinds of perturbations that were used for the V+AV case, where one can see that the local minima consist of simple concatenations in the $z-$direction of V+AV+V+AV configurations.

Finally, the $\alpha = 0$ case is similar for both V+AV and V+AV+V+AV $N-$stacks, in the sense that the configurations have collapsed under perturbations for $N = \{3, 4, 5\}$. This might be due to the fact that our perturbation, for $N > 2$, consists of removing part of the region between the vortices for the middle copies of the V+AV+V+AV configuration, which are again more closely merged in the $\alpha = 0$ case than for other α values, and therefore, the perturbation also has the effect of removing a significant chunk of the vortices themselves. This is clearly seen in the $N = 3$ case, where the chunk in the middle is triangular, rather than square-shaped; this configuration has a total of 22 holes: 16 from the square-shaped ends and 6 from the middle. The $N = 4$ and $N = 5$ configurations consist of (flattened) polyhedral structures; in the former case, it has a total of 24 holes (12 hexagons, 12 pentagons) and, in the latter case, it has a total of 28 holes (13 hexagons, 15 pentagons). Note that these numbers show that these configurations do not follow the "Geometric Energy Minimization" (GEM) rule, which states that the isosurfaces contain $2(Q - 1)$ holes, and are also not "fullerene-like", since

they are not composed of 12 pentagons and $2Q - 14$ hexagons (for $Q \geq 7$) [10]. Also note that the $N = 5$ configuration starts to merge with itself across the boundary, in the $x-$direction, which might be a sign that the periods $L_{x,y} = 10$ are now small for such large configurations, in the sense that they can no longer be considered isolated. The effect of our perturbations can also be clearly seen in the large errors for $N = \{3, 4, 5\}$, which increase with N.

Table 6.3: Normalized energy ($E_N = E/Q$) of V+AV+V+AV N-stack solutions with associated errors.

	$\alpha = 0$	$\alpha = 0.3$	$\alpha = 0.6$	$\alpha = 0.9$
$N = 1$	1.084 ± 0.004	1.068 ± 0.004	1.031 ± 0.004	0.946 ± 0.007
$N = 2$	1.084 ± 0.004	1.068 ± 0.004	1.031 ± 0.004	0.915 ± 0.003
$N = 3$	1.00 ± 0.09	1.068 ± 0.004	1.031 ± 0.004	0.812 ± 0.002
$N = 4$	0.9 ± 0.2	1.068 ± 0.004	1.031 ± 0.004	0.819 ± 0.002
$N = 5$	0.8 ± 0.3	1.068 ± 0.004	1.031 ± 0.004	0.757 ± 0.005

An analysis of the $(p, q)-$charges of the twisted and braided vortices for the $\alpha = 0.9$ case could also be carried out, using the methods outlined in the previous section, but we have decided to forgo this, as it is our belief that such a task would not add any new and interesting results to our discussion. On that note, we end our discussion of triply-periodic solutions of generalized Skyrme systems. We now turn to our concluding remarks, where we summarize our results and provide a short discussion of possible future avenues of research.

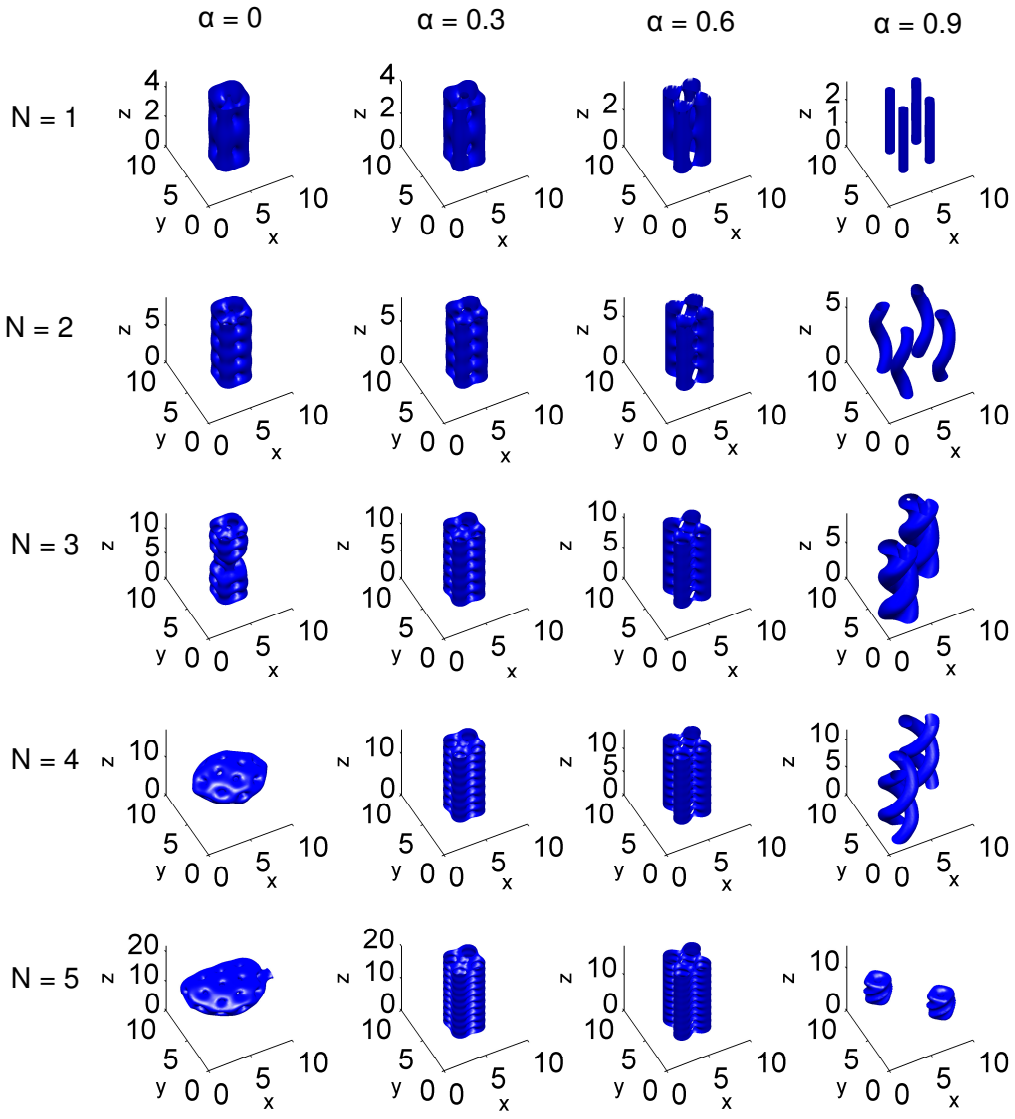

Figure 6.7: V+AV+V+AV N-stack energy density isosurfaces for $N = (1, 2, 3, 4, 5)$ and $\alpha = (0, 0.3, 0.6, 0.9)$. The surface values used are: $\mathcal{E} = 0.15 * \mathcal{E}_{\max}$ for $\alpha = 0$; $0.25 * \mathcal{E}_{\max}$ for $\alpha = 0.3, 0.6$; $0.5 * \mathcal{E}_{\max}$ for $\alpha = 0.9$, $N = \{1, 2, 4\}$ and $0.3 * \mathcal{E}_{\max}$ for $N = \{3, 5\}$.

Part IV

Concluding Remarks

Summary

We have dealt with a one-parameter family of generalized Skyrme systems, which interpolate between the Skyrme model and the Skyrme-Faddeev model. The parameter is given by $\alpha \in [0, 1]$, reproducing the Skyrme model when $\alpha = 0$ and the Skyrme-Faddeev model when $\alpha = 1$.

The Skyrme model, whose solitonic solutions are called skyrmions, was originally proposed as a theory of pions and was later shown that it is a low-energy approximation to QCD, in the limit where the number of colours goes to infinity. The Skyrme-Faddeev model features string-like solutions, which often take the form of knotted solitons.

The Skyrme crystal, which consists of a maximally-attractive (cubic) arrangement of skyrmions, was originally proposed as a model of dense nuclear matter and is still the lowest energy-per-charge configuration of skyrmions seen so far. To study the Skyrme crystal, which consists of an infinite number of half-skyrmions, we constrain ourselves to a triply-periodic lattice of eight half-skyrmions.

One of the themes we explored consists of the deformation of the Skyrme crystal, at $\alpha = 0$ [3]. This has involved varying the periods away from the optimal (energy-minimizing) values, in all three directions. It was found that, in the limit of large $L_{x,y}$ periods and small L_z periods, vortex-like structures appear. In the limit of small $L_{x,y}$ periods and large L_z periods, a pair of square "sheets" are seen to appear.

Subsequently, we made a detailed investigation of the energy of a pair ($N = 2$) of these square sheets, as well as a pair of hexagonal sheets, and found that the latter "prefer" to be misaligned in the $z-$direction, in the sense that their energy is smaller than when they are aligned. Moreover, we found that a pair of (aligned) square sheets have a smaller energy-per-charge value than a pair of misaligned hexagonal sheets. The hexagonal sheets were found to

be highly unstable for $N > 2$ – for both $L_y = \sqrt{3}L_x$ and $L_y \neq \sqrt{3}L_x$; in both cases, we claim that the sheets tend to lose their hexagonal symmetry. The $N > 2$ square sheet case has been explored further in [2], where it was found that the energy-per-charge has a $1/N$-dependence, with a value very close to that of the Skyrme crystal in the limit $N \to \infty$.

Another of the themes consists of a numerical study of the Skyrme crystal within the context of generalized Skyrme systems. The work has involved a full three-dimensional numerical minimization of its energy, as a function of α, and the subsequent analysis of its fields and energy density surface plots. At $\alpha = 0$, the resulting structure is the Skyrme crystal, but as $\alpha \to 1$, the local minimal-energy solutions include arrays of vortices produced from the pair-wise merging of the half-skyrmions (V+AV+V+AV solution) – akin to the ones mentioned earlier, in the context of deformed Skyrme crystals; a pair of vortices, each of which has charge $|p| = 2$ (2V+2AV solution); and multi-sheeted structures. The local minimum obtained depends on both the ansatz and the initial periods used: we have used the Skyrme crystal ansatz [45] for the V+AV+V+AV solution and an ansatz featured in [1] for the 2V+2AV and multi-sheet solutions. The latter two are obtained by using different initial periods.

Since vortices crop up in the deformations of the $\alpha = 0$ Skyrme crystal as well as in its $\alpha \to 1$ limit, we decided to investigate the stability of V+AV and V+AV+V+AV configurations in generalized skyrme systems, by using a multi-vortex ansatz. First, we made a generalization of the analytic results in [8], which show that there is an attractive force between a vortex-antivortex pair at large separation, and we found that the term that describes this force vanishes in the $\alpha \to 1$ limit. This result, as well as an analysis of the optimal periods of the V+AV+V+AV and 2V+2AV configurations, suggest that vortices repel each other in this limit. Next, we studied the stability of V+AV and V+AV+V+AV configurations for several different

values of α by stacking N copies of such configurations in the $z-$direction and introducing certain perturbations. We have shown that, under these perturbations, the configurations tend to become unstable for $N > 2$, at $\alpha = 0$, collapsing into polyhedric structures. Furthermore, twisting structures, including both separated and braided ones, appear at $\alpha \geq 0.5$, with $N \geq 2$ (for the V+AV case), and at $\alpha = 0.9$, $N \geq 2$ (for the V+AV+V+AV case). Finally, we have described a numerical method for calculating the $(p, q)-$charges of the braided V+AV configurations and have shown that these are consistent with an analytic expression for their charge Q, given in terms of their $(p, q)-$charges.

Possible future directions

Note that the model of generalized Skyrme systems we have considered assumes massless pions. However, there has been much recent work [53–56], based on early studies [57, 58], where a pion mass term m_π has been added to the Skyrme Model.

This has been done in order to make stronger connections between the Skyrme Model and Nuclear Physics. Such a model has produced results which are remarkably close to experimental observations. As stated in [55], the shell-like fullerene structures present in the massless limit (at high charge values) tend to collapse and form clusters of lower-charge components, mostly of charge 3 and 4, when a pion mass is added, which is good news since it is known that many nuclei can be described as configurations of alpha particles. In [56], besides adding a pion mass, the skyrmions were quantized as rigid bodies in space and isospace. The quantum states predicted by the model reproduce experimental data of light nuclei (such as spin splittings, isobar splittings, and moments of inertia) quite well, with correct spins and parities.

Since, for high m_π values, the shells are unstable and a Skyrme crystal-type

configuration is preferred [53], it would be interesting to numerically study the Skyrme crystal as a function of both α and m_π to see what kind of structures emerge and identify any possible connections with physical systems.

Such a connection has been established between the $\alpha = 1$ limit and condensed-matter systems [59], where it has been shown that the Ginzburg-Landau-Gross-Pitaevskii (GLGP) model with two charged condensates has both a hidden symmetry and allows for the formation of knotted solitons, like the ones present in the Skyrme-Faddeev Model.

It was later shown (on a compact domain) that such condensed-matter systems also contain a field, which tends to destroy the topological stability of the knotted solitons present in the theory [60]. However, this does not mean that one cannot find a similar, stable, system since it might be possible to add terms to the theory to stabilize it and/or to consider different physical domains. We have also encountered certain instabilities in the $\alpha \to 1$ limit, in the context of Skyrme crystals [1], which are not present for other values of α. Therefore, there exists the possibility of finding stable solutions (with $m_\pi \geq 0$) for $\alpha \in (0, 1)$, which might have a connection with physical systems; the massive $\alpha = 1$ case has been presented in [61]. With this in mind, it would be interesting to carry out numerical and analytical studies of the system considered in [59], but with α included.

Through discussions with Prof. Nick Manton, an idea has also emerged of deforming the Skyrme crystal, as in Chapter 3 and [3], but this time by performing a diagonal stretch. This diagonal stretch can be done by changing the spatial metric tensor from the standard euclidean form in the expression for the energy density (and its gradient), derived from the Lagrangian in eq. (2.17), and implement it in the existing energy-minimizing code. The motivation comes from looking at a Skyrme crystal along one of the diagonals. Given enough half-skyrmions, one can see hexagonal, rather than cubic, symmetry. Therefore, the expectation is that a diagonal stretch might pro-

duce parallel, hexagonal sheets, such as those studied in Chapter 4 and [7], which are analogous to graphene sheets, or it can produce other structures. This can be investigated with $m_\pi \geq 0$.

Finally, as mentioned previously, there has been a substantial effort in quantizing the Skyrme Model ($\alpha = 0$), as well as the Skyrme-Faddeev Model ($\alpha = 1$) [37], so it would be interesting to look at quantum corrections for $\alpha \in (0, 1)$. Such a task might be worth doing, as it might uncover previously unseen phenomena, with possible interesting connections with nuclear and condensed-matter physics.

Part V

Appendix

Appendix A

Numerical Methods

The main ingredients in our numerical calculations have consisted in using the forward-difference approximation for the derivatives appearing in the expression for the energy density of generalized skyrme systems, eq. (2.26), and the trapezoid rule in evaluating its integral over a triply-periodic lattice, both of which we now describe.

The forward-difference approximation for the derivative of a function $f(x)$, defined on a lattice with lattice spacing h, is given by:

$$\frac{df}{dx} \approx \frac{f(x+h) - f(x)}{h}. \tag{A.1}$$

The error in the approximation (A.1) can be gracefully described through a Taylor series approximation of $f(x+h)$:

$$f(x+h) = f(x) + \left(\frac{df}{dx}\right) h + \frac{1}{2!}\left(\frac{d^2f}{dx^2}\right) h^2 + \frac{1}{3!}\left(\frac{d^3f}{dx^3}\right) h^3 + \frac{1}{4!}\left(\frac{d^4f}{dx^4}\right) h^4 + \cdots, \tag{A.2}$$

which leads to

$$\frac{f(x+h) - f(x)}{h} - \frac{df}{dx} = \frac{1}{2!}\left(\frac{d^2f}{dx^2}\right) h + \frac{1}{3!}\left(\frac{d^3f}{dx^3}\right) h^2 + \frac{1}{4!}\left(\frac{d^4f}{dx^4}\right) h^3 + \cdots. \tag{A.3}$$

Looking at eq. (A.3) one can see that the error in the forward-difference approximation, to leading order, is $\mathcal{O}(h)$ – called the "truncation error".

The trapezoid rule is given by:

$$\int_a^b f(x)\,dx \approx \frac{1}{2}\sum_{i=0}^{n-1}(x_{i+1}-x_i)[f(x_i)+f(x_{i+1})]\,, \tag{A.4}$$

which calculates the integral by splitting the region under the curve $f(x)$ into n trapezoids, with upper corners touching the function $f(x)$, and adding the individual areas: width $\times$ height$= (x_{i+1}-x_i)\times(f(x_i)+f(x_{i+1}))/2$. The error in the approximation (A.4), to leading order, is $\mathcal{O}(h^2)$, where $h = x_{i+1} - x_i$ (see e.g. [62]).

Predicting the exact behaviour of the numerical error, given in terms of the lattice spacing, is not a trivial task, especially for multi-dimensional models, whose derivatives and integrals are approximated as above. In our 3-dimensional case, we have found it quite useful to simply evaluate the energy of a certain configuration, for different values of the lattice spacing h. That is, by applying the 3-dimensional extensions of the approximations (A.1) and (A.4) to the integral of eq. (2.26) over a triply-periodic lattice, for a certain field configuration $\Phi_\beta(\mathbf{x}) = (\Phi_1(\mathbf{x}), \Phi_2(\mathbf{x}), \Phi_3(\mathbf{x}), \Phi_4(\mathbf{x}))$, and for different values of h. One can then readily see the behaviour of the numerical errors involved by plotting the energy as a function of h. We have found that using the approximations detailed above, for generalized skyrme systems, the errors are $\mathcal{O}(h^2)$ as one can see from the linear behaviour in our plots of E vs h^2; see e.g. Figs. $4.1, 4.2, 5.1$, where one can see a similar behaviour for the charge Q and the periods L_x, L_y, and L_z. An important thing to note from these figures is that one can extrapolate the charge Q to $h = 0$, where its value gets very close to the actual topological charge, which is always an integer. Therefore, we expect the extrapolated values of the energy and the periods (which are derived from energy minima) to be similarly close to their "actual" values. Since the same 3-dimensional extensions to (A.1) and (A.4)

are applied to the expression for the charge, eq. (2.5), we expect a similar numerical error; therefore, the errors quoted in the text for the energies are given in terms of the difference between the numerical and actual charges, for specified values of h.

Finally, we should clarify what we mean in the text by "second order finite-difference" schemes. The energy (or charge), having an h^2 dependence, can be expressed as follows:

$$E_h = E_0 + ch^2 \,, \tag{A.5}$$

where E_0 is the value of the energy extrapolated to $h = 0$ and c is a constant. If one also determines the energy by measuring it only at even-numbered lattice sites, i.e. with a lattice spacing of $2h$, then one would have the following expression:

$$E_{2h} = E_0 + 4ch^2 \,. \tag{A.6}$$

Solving eq. (A.5) for c and substituting into (A.6), we get the following expression for the extrapolated energy:

$$E_0 = \frac{4}{3}E_h - \frac{1}{3}E_{2h} \,. \tag{A.7}$$

A similar calculation can be done for the charge Q.

Therefore, the second order finite-difference scheme involves calculating the energy with two different values of lattice spacing: h and $2h$, as opposed to a first order finite-difference scheme, where only the value of h is used – this is always specified in the text. Obviously, the smaller the value of lattice spacing used, the closer the value of E_0 will be to the "actual" value, but the energy minimization procedure would take longer (if one is dealing with minimized fields $\Phi_\beta(\mathbf{x})$, as is usually the case here).

Bibliography

[1] J. Silva Lobo and R.S. Ward, *Generalized Skyrme Crystals*, Phys.Lett. **B696**, 283–287 (2011), arXiv:1012.4090 [hep-th].

[2] J. Silva Lobo and R.S. Ward, *Skyrmion Multi-Walls*, J.Phys.A **A42**, 482001 (2009), arXiv:0910.5457 [hep-th].

[3] J. Silva Lobo, *Deformed Skyrme Crystals*, JHEP **1010**, 029 (2010), arXiv:1010.0619 [hep-th].

[4] R.S. Ward, *Skyrmions and Faddeev-Hopf solitons*, Phys.Rev. **D70**, 061701 (2004), arXiv:hep-th/0407245 [hep-th].

[5] John Scott Russell, *Report on waves* (1845), Proceedings of the British Association for the Advancement of Science, 14th Meeting, 311-390.

[6] Zachariah Sinkala, *Soliton/exciton transport in proteins*, J. Theor. Biol. **241**, 919 – 927 (2006), ISSN 0022-5193.

[7] Richard A. Battye and Paul M. Sutcliffe, *A Skyrme lattice with hexagonal symmetry*, Phys.Lett. **B416**, 385–391 (1998), arXiv:hep-th/9709221 [hep-th].

[8] Derek Harland and R.S. Ward, *Chains of Skyrmions*, JHEP **0812**, 093 (2008), arXiv:0807.3870 [hep-th].

[9] T.H.R. Skyrme, *A Nonlinear field theory*, Proc.Roy.Soc.Lond. **A260**, 127–138 (1961).

[10] N. Manton and P. Sutcliffe, *Topological Solitons* (Cambridge University Press, 2004) ISBN 0-521-83836-3.

[11] G.H. Derrick, *Comments on nonlinear wave equations as models for elementary particles*, J.Math.Phys. **5**, 1252–1254 (1964).

[12] Edward Witten, *Current Algebra, Baryons, and Quark Confinement*, Nucl.Phys. **B223**, 433–444 (1983).

[13] Edward Witten, *Baryons in the 1/N Expansion*, Nucl.Phys. **B160**, 57 (1979).

[14] L.D. Faddeev, *Some Comments on the Many Dimensional Solitons*, Lett.Math.Phys. **1**, 289 (1976).

[15] V.B. Kopeliovich and B.E. Stern, *Exotic Skyrmions*, JETP Lett. **45**, 203–207 (1987).

[16] N.S. Manton, *Is the B=2 skyrmion axially symmetric?*, Phys.Lett. **B192**, 177 (1987).

[17] J.J.M. Verbaarschot, *Axial symmetry of bound baryon number two solution of the Skyrme Model*, Phys.Lett. **B195**, 235 (1987).

[18] Eric Braaten, Steve Townsend, and Larry Carson, *Novel Structure of Static Multi - Soliton Solutions in the Skyrme Model*, Phys.Lett. **B235**, 147 (1990).

[19] Richard A. Battye and Paul M. Sutcliffe, *Symmetric skyrmions*, Phys.Rev.Lett. **79**, 363–366 (1997), arXiv:hep-th/9702089 [hep-th].

[20] Richard M. Battye and Paul M. Sutcliffe, *Solitonic fullerenes*, Phys.Rev.Lett. **86**, 3989–3992 (2001), arXiv:hep-th/0012215 [hep-th].

[21] Richard A. Battye and Paul M. Sutcliffe, *Skyrmions, fullerenes and rational maps*, Rev.Math.Phys. **14**, 29–86 (2002), arXiv:hep-th/0103026 [hep-th].

[22] Richard A. Battye, Conor J. Houghton, and Paul M. Sutcliffe, *Icosahedral skyrmions*, J.Math.Phys. **44**, 3543–3554 (2003), arXiv:hep-th/0210147 [hep-th].

[23] Jan Cami, Jeronimo Bernard-Salas, Els Peeters, and Sarah Elizabeth Malek, *Detection of C60 and C70 in a Young Planetary Nebula*, Science **329**, 1180–1182 (2010), http://www.sciencemag.org/content/329/5996/1180.full.pdf.

[24] N.S. Manton, *Geometry of skyrmions*, Commun.Math.Phys. **111**, 469 (1987).

[25] L.D. Faddeev, *Quantisation of solitons* (1975), princeton preprint IAS-75-QS70.

[26] L.D. Faddeev and Antti J. Niemi, *Stable knot-like structures in classical field theory*, Nature **387**, 58 (1997), arXiv:hep-th/9610193 [hep-th].

[27] R.S. Ward, *Hopf solitons on S(3) and R(3)*, Nonlinearity **12**, 241–246 (1999), arXiv:hep-th/9811176 [hep-th].

[28] R.S. Ward, *The Interaction of two Hopf solitons*, Phys.Lett. **B473**, 291–296 (2000), arXiv:hep-th/0001017 [hep-th].

[29] Roger Penrose, *The Road to Reality* (Vintage Books, 2006) ISBN 0-099-44068-7.

[30] Jens Gladikowski and Meik Hellmund, *Static solitons with nonzero Hopf number*, Phys.Rev. **D56**, 5194–5199 (1997), arXiv:hep-th/9609035 [hep-th].

[31] Richard A. Battye and Paul Sutcliffe, *Solitons, links and knots*, Proc.Roy.Soc.Lond. **A455**, 4305–4331 (1999), arXiv:hep-th/9811077 [hep-th].

[32] Jarmo Hietarinta and Petri Salo, *Faddeev-Hopf knots: Dynamics of linked unknots*, Phys.Lett. **B451**, 60–67 (1999), arXiv:hep-th/9811053 [hep-th].

[33] Mauri Miettinen, Antti J. Niemi, and Yuri Stroganov, *Aspects of duality and confining strings*, Phys.Lett. **B474**, 303–308 (2000), arXiv:hep-th/9908178 [hep-th].

[34] Pierre van Baal and Andreas Wipf, *Classical gauge vacua as knots*, Phys.Lett. **B515**, 181–184 (2001), arXiv:hep-th/0105141 [hep-th].

[35] L. Pontrjagin, *A classification of mappings of the three-dimensional complex into the two-dimensional sphere*, Rec. Math. [Mat. Sbornik] N.S. **9(51)**, 331–363 (1941), `http://mi.mathnet.ru/msb6073`.

[36] Jarmo Hietarinta, Juha Jaykka, and Petri Salo, *Relaxation of twisted vortices in the Faddeev-Skyrme model*, Phys.Lett. **A321**, 324–329 (2004), arXiv:cond-mat/0309499 [cond-mat].

[37] Steffen Krusch and J.Martin Speight, *Fermionic quantization of Hopf solitons*, Commun.Math.Phys. **264**, 391–410 (2006), arXiv:hep-th/0503067 [hep-th].

[38] Paul Sutcliffe, *Knots in the Skyrme-Faddeev model*, Proc.Roy.Soc.Lond. **A463**, 3001–3020 (2007), arXiv:0705.1468 [hep-th].

[39] Juha Jaykka and Jarmo Hietarinta, *Unwinding in Hopfion vortex bunches*, Phys.Rev. **D79**, 125027 (2009), arXiv:0904.1305 [hep-th].

[40] A.F. Vakulenko and L.V. Kapitansky, *Stability of solitons in S(2) in the nonlinear sigma model*, Sov.Phys.Dokl. **24**, 433–434 (1979).

[41] A. Kundu and Yu.P. Rybakov, *Closed vortex type solitons with Hopf index*, J.Phys.A **A15**, 269–275 (1982).

[42] Igor R. Klebanov, *Nuclear matter in the Skyrme Model*, Nucl.Phys. **B262**, 133 (1985).

[43] Alfred S. Goldhaber and N.S. Manton, *Maximal symmetry of the Skyrme crystal*, Phys.Lett. **B198**, 231 (1987).

[44] A.D. Jackson and J.J.M. Verbaarschot, *Phase structure of the Skyrme Model*, Nucl.Phys. **A484**, 419 (1988).

[45] L. Castillejo, P.S.J. Jones, A.D. Jackson, J.J.M. Verbaarschot, and A. Jackson, *Dense skyrmion systems*, Nucl.Phys. **A501**, 801 (1989).

[46] M. Kugler and S. Shtrikman, *A new skyrmion crystal*, Phys.Lett. **B208**, 491 (1988).

[47] M. Kugler and S. Shtrikman, *Skyrmion crystals and their symmetries*, Phys.Rev. **D40**, 3421 (1989).

[48] W.H. Press, B.P. Flannery, S.A. Teukolsky, and W.T. Vetterling, *Numerical Recipes in FORTRAN 77* (Cambridge University Press, 1992) ISBN 052143064X.

[49] A. Visintin, *Differential Models of Hysteresis* (Springer-Verlag Berlin Heidelberg, 1994) ISBN 3-540-54793-2.

[50] Milton Abramowitz and Irene A. Stegun, *Handbook of Mathematical Functions: with Formulas, Graphs, and Mathematical Tables* (Dover Publications, 1965) ISBN 9780486612720.

[51] E. T. Whittaker and G. N. Watson, *A Course of Modern Analysis* (Cambridge University Press, 1927) ISBN 0521588073.

[52] Frank W. J. Olver, Daniel W. Lozier, Ronald F. Boisvert, and Charles W. Clark, *NIST Handbook of Mathematical Functions* (Cambridge University Press, 2010) ISBN 0521192250.

[53] Richard Battye and Paul Sutcliffe, *Skyrmions and the pion mass*, Nucl.Phys. **B705**, 384–400 (2005), arXiv:hep-ph/0410157 [hep-ph].

[54] Richard A. Battye, Steffen Krusch, and Paul M. Sutcliffe, *Spinning skyrmions and the skyrme parameters*, Phys.Lett. **B626**, 120–126 (2005), arXiv:hep-th/0507279 [hep-th].

[55] Richard Battye and Paul Sutcliffe, *Skyrmions with massive pions*, Phys.Rev. **C73**, 055205 (2006), arXiv:hep-th/0602220 [hep-th].

[56] Richard A. Battye, Nicholas S. Manton, Paul M. Sutcliffe, and Stephen W. Wood, *Light Nuclei of Even Mass Number in the Skyrme Model*, Phys.Rev. **C80**, 034323 (2009), arXiv:0905.0099 [nucl-th].

[57] Gregory S. Adkins, Chiara R. Nappi, and Edward Witten, *Static Properties of Nucleons in the Skyrme Model*, Nucl.Phys. **B228**, 552 (1983).

[58] Gregory S. Adkins and Chiara R. Nappi, *The Skyrme Model with Pion Masses*, Nucl.Phys. **B233**, 109 (1984).

[59] Egor Babaev, L.D. Faddeev, and Antti J. Niemi, *Hidden symmetry and knot solitons in a charged two-condensate Bose system*, Phys.Rev. **B65**, 100512 (2002), arXiv:cond-mat/0106152 [cond-mat.supr-con].

[60] J.M. Speight, *Supercurrent coupling in the Faddeev-Skyrme model*, J.Geom.Phys. **60**, 599–610 (2010), arXiv:0812.1493 [hep-th].

[61] David Foster, *Massive hopfions*, Phys. Rev. D **83**, 085026 (2011), arXiv:1012.2595 [hep-th].

[62] E. Cheney and D. Kincaid, *Numerical Mathematics and Computing* (Thomson Brooks/Cole, 2007) ISBN 978-0495384724.